THE UNIVERSITY OF MICHIGAN

College of Engineering

Department of Mechanical Engineering

Cavitation and Multiphase Flow Laboratory

PRE-STRESS CONDITIONING AND ITS EFFECTS ON MATERIAL ATTRITION IN A CAVITATING ENVIRONMENT

by: Dale J. Kemppainen

Approved: Frederick G. Hammitt

A Dissertation Submitted

in Partial Fulfillment of the Requirements

for the Degree of Nuclear Engineer

at the University of Michigan

1969

ABSTRACT

An investigation of the effects of stresses applied during cavitation attack upon damage to metals of varying mechanical properties and crystalline structures and upon subsequent strength characteristics of the damaged metals was undertaken.

Initial tests were made with cylindrical stainless steel specimens placed across the diffuser of a venturi in both mercury and water systems. In the mercury system the tension specimen exhibited slightly more damage than the no load specimen, although damage patterns were very similar. A compressive stress tended to reduce the number of small pits, which may be interpreted as extension of the incubation period. Neither stress had much effect on large pits.

Later tests were made with specimens placed in a cavitation field created by an ultrasonic vibratory facility. In tests with specimens (copper and aluminum) under radially symmetric compression due to a shrink-fitted external rim, damage was greater than in identical tests with unstressed specimens.

The most extensive study was made with specimens of seven different metals stressed axially in both tension and compression. In general for HCP and FCC crystalline structured metals, with stresses applied parallel to the rolling direction, a compressive stress decreased and a tensile stress increased both cavitation damage in the incubation period and the later cavitation damage rate. The effects were markedly larger in the HCP metal (magnesium). Damage rate increased in both stress modes for the BCC metal (1020 steel). The effect of a stress applied perpendicular to the rolling direction was shown to be mixed and dependent upon the material.

Tensile and yield strengths were determined for copper and aluminum tension-compression specimens after testing. The fact that tensile strengths (corrected for change in area) were lowered in all cases was attributed to the effect of microcracks, the existence of which were verified by metallurgical examination. Yield strengths were also affected; however, additional factors such as strain hardening and residual compressive stresses made the effect on yield strengths highly dependent upon the material and its directional properties.

Acknowledgments: The author would like to acknowledge the financial support provided by the Atomic Energy Commission through their fellowship program.

The assistance and guidance provided by Professor F.G. Hammitt during the duration of this investigation is gratefully appreciated.

The author would also like to acknowledge the assistance of Mr. Edward Timm and Mr. Darrell Rogers for their help in various phases of this study.

My most sincere and grateful thanks are due my wife, Jeanne, who through her unselfish attitude and love provided stability and encouragement for me during the years this dissertation was being conducted.

TABLE OF CONTENTS

LIST OF TABLES

LIST OF FIGURES

I. INTRODUCTION

Cavitation is a phenomenon of great importance not because of its inception but because of its termination. In all flowing systems the possibility of cavitation is a real problem since its effects can be detrimental to the flow system as a whole. The present study is an effort to investigate the problem of material attrition, under different surface conditions, due to cavitation bubble collapse. Here, the problem of what can be done to the system components to lessen the amount of material attrition, thereby increasing the useful life of the system as a whole, was undertaken considering an à priori existence of cavitation which cannot be alleviated by flow parameter control.

A considerable amount of data on material attrition has already been reported from this laboratory and of course elsewhere also; however, very little information has been obtained on materials under stress and the effect of this stress. This is unfortunate, in that the components of any flowing system are usually, at some point, under either compressive or tensile loading. The same is true of fuel element clodding, bundle supports and numerous other components which are in the coolant flow channels of nuclear reactors.

It is to fill this gap in our knowledge that the present investigation was initiated. Previous data from this laboratory (1, 2) indicated that a tensile pre-stress on the material surface, subjected to cavitation attack, exhibited a greater tendency toward material attrition than did a surface which was in the unstressed state. The data on 304SS included in these reports show applied tensile loads of up to 1.3 times the yield strength of the material (52,500 psi). With these loads, increases in damage, of up to 8% were noted. Admittedly this factor of damage increase with the applied load is not substantial

nor is it sufficient to indicate the certainty of an important effect. However, it does indicate the possible presence of a trend.

A second study of the effect of pre-stress, possibly in response to our work as he was a contributor to the Royal Society meeting where this was discussed and did submit a discussion on our paper; was conducted in 1967 by Shal'nev et al. (3) in the U.S. S. R. In contrast to the flowing system used here (1, 2) they used a magnetostriction apparatus with a fixed specimen. Such a system was also used here (4) at about the same time though not for stress associated tests. In Shal'nev's tests on a material similar to our 3003-0 aluminum, an increase in damage rate up to 140% was reported as the level of tensile stress increased from zero to 50% yield stress. As the magnitude of the stress was increased the erosion rate stabilized, and became less dependent on the stress level. They found that the primary effect of the stress was most noticeable during the incubation period at which time the added tensile stresses caused increased erosion rates.

Barnard and Cooper (5) at Cambridge University conducted an experiment to study the effects of spark-induced bubbles on a ribbon of material under a tensile load. They used a vacuum-cast oxygen-free high-conductivity (OFHC) copper. The bubble size and distance as well as the stress levels were varied. They observed that the strain was dependent upon the difference between the applied stress and the yield stress, and not upon the absolute magnitudes. They also found that a bubble which collapsed within its maximum radius of the specimen caused the maximum amount of damage. The experiment showed that if a series of bubbles all of the same size were allowed to collapse near the specimen, the elongation strain caused by successive bubbles decreased at a greater rate than would be expected from work hardening effects.

In the above investigations no work has been mentioned concerning the effects of compressive stresses on the erosion rate. To the author's knowledge our present investigation is the only one which takes the compressive mode into consideration.

The expected benefits from this study were two-fold:

i) Additional information and insight into the mechanism of cavitation damage.

ii) Information regarding questions as the following:

1. What is the effect of compressive and tensile stresses on the development of cavitation damage?
2. How do these stresses affect the damage rate in materials of different hardness and strength, but of the same basic crystalline structure?
3. What are the effects of compressive and tensile stresses on damage to materials of different structure?
4. Is there a change in the mechanical strength properties of the materials due to cavitation attack, and is this enhanced or reduced by the applied stress?

In order to pursue these questions several materials were chosen: 304 Stainless Steel, 65/35 Brass, OFHC copper, 3003-0 Aluminum, Bearing Bronze-Azarcon 773(SAE660), magnesium, and mild steel (1020 steel). Of these materials the first five are basically of FCC (face centered cubic)structure, whereas the magnesium is HCP (hexagonal close packed) and the mild steel is a BCC (body centered cubic) structure.

Damage tests were run at 3 stress levels for each material: 1) tension of approximately 75% yield stress, 2) compression of approximately 75% yield stress, and 3) no external force. The latter condition served as a control for each material, thereby allowing comparison of the effects of stress with a common "normal" condition.

It is the object of this report to present the results of this investigation as well as a clear outline of how the data were obtained in order that further work along these same lines may be completed, thereby adding more insight into the principles and peculiarities of cavitation erosion and its prevention.

II. EXPERIMENTAL FACILITIES

During the course of the investigation three different experimental facilities were used to obtain information pertinent to the effects of a cavitation field on a stressed surface. These were A) Water Loop, B) Mercury Loop, and C) Vibratory Facility. Each of these facilities have been described elsewhere (6, 7, 8). However, for the purposes of completeness and further reference they will be covered briefly here.

A. Water Loop

The water loop facility is a closed loop multiple venturi system. It consists of four closed loops which are capable of parallel, simultaneous operation. The facility is also equipped with deaereation and purification equipment which allows preconditioning and control of the water used for testing. The maximum throat velocity is in excess of 200 ft. per second. For the tests performed in this study, however, fairly low velocities were used (less than 100 ft/sec).

Figure 1 is a schematic diagram of the facility and Figure 2 is a photograph of the facility with all loops in position. For these specific tests only one loop was used, with the remaining three parallel loops closed off. A more detailed explanation of the particular experimental apparatus used in this facility for the present tests will be given in a later section.

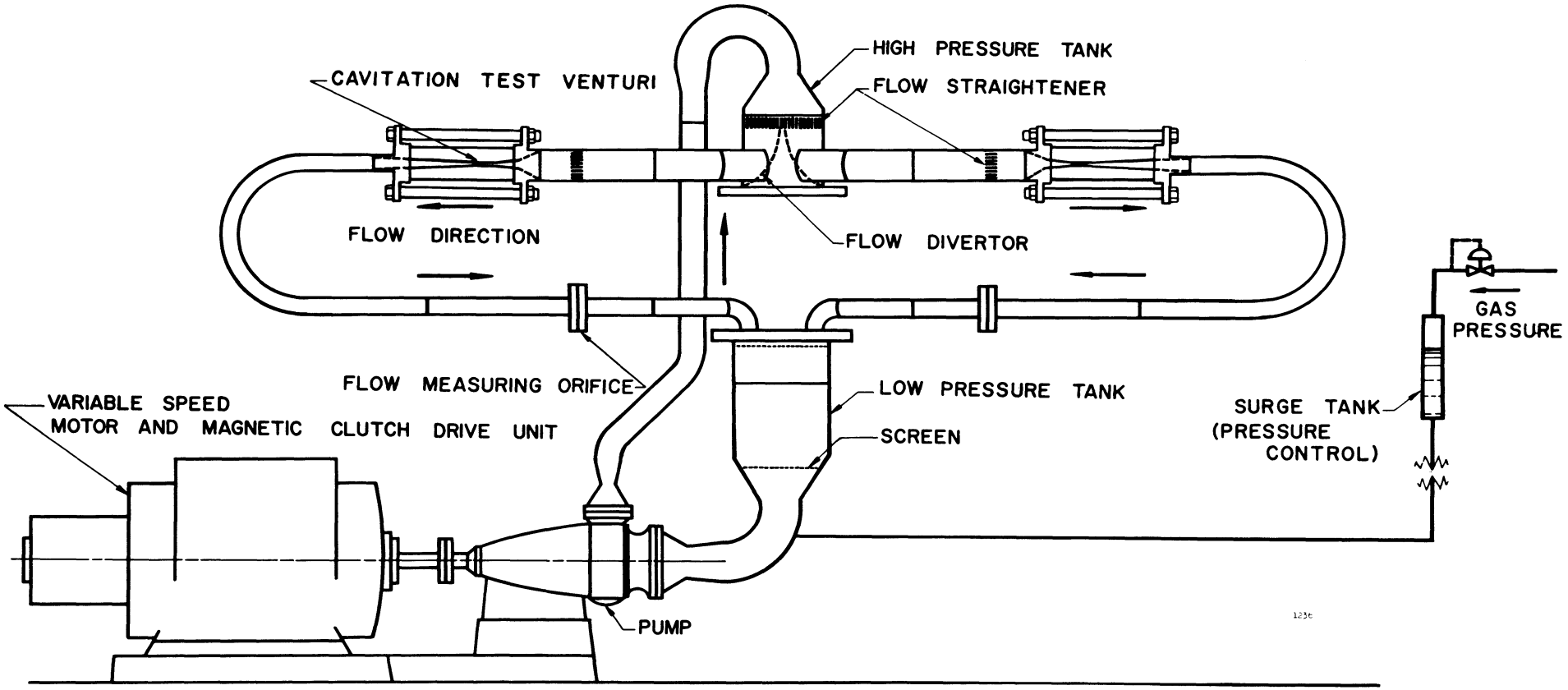

Fig. 1. Schematic of Water Cavitation Damage Facility
(only two of the four loops shown)

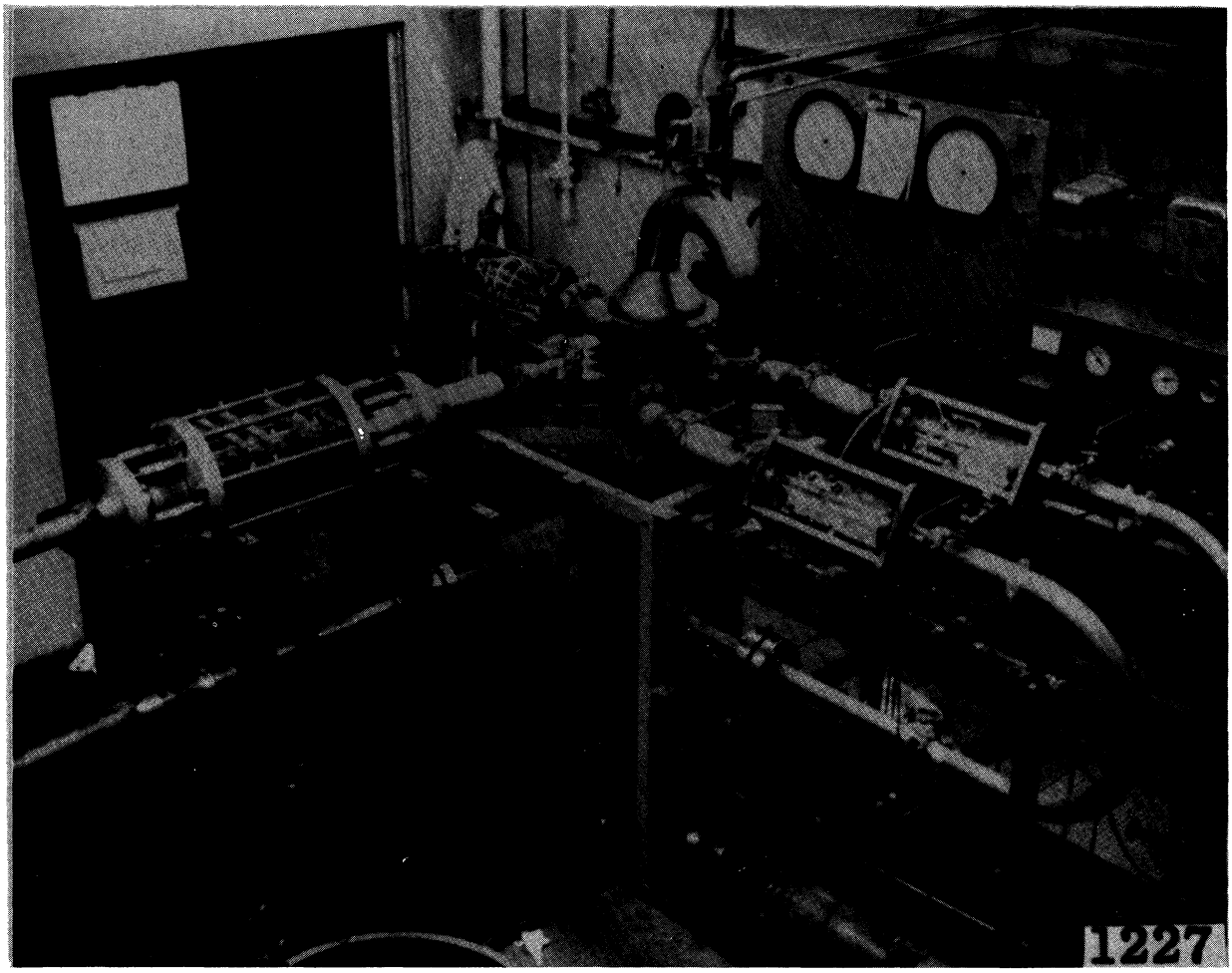

Fig. 2. Photograph of Water Cavitation, Closed Loop Venturi Facility

B. Mercury Loop

Since previous studies had shown that damage could be rapidly obtained in the mercury loop, this facility was used in our earlier investigation of the effect of stresses. A schematic of this system is shown in Figure 3.

The mercury facility is a closed loop consisting of a venturi test section, a flow measuring venturi, two throttle valves, and approximately 20 feet of 1 1/2-inch, schedule 40 stainless steel pipe. It is powered by an overhung sump-type centrifugal pump capable of producing a head rise in mercury of about 40 ft. at a flow rate of 40 gpm (7).

Figure 4 is a photograph of the mercury facility showing the heater units used for high temperature tests. This capability was not required in the present investigation. Further details which concern the particular experimental apparatus needed and required modifications to this facility will be discussed later.

C. Vibratory Facility

The vibratory system used was that designed by Garcia (8) and used in many of the material evaluations reported previously. It has been explained in detail in Garcia's work (8). However, a brief summary of the important features will be outlined here.

This facility at the University of Michigan utilized the piezoelectric effect for the production of a cavitation field. The system uses two lead zirconate-titanate crystals. To produce dilation of the crystals, an alternating electric field is applied to their parallel faces. The voltage applied causes them to alternately expand and contract in length by $\sim$ 0.1 to 0.2 mils (10). To take full advantage of the movement of the crystals it is necessary to mechanically amplify these movements.

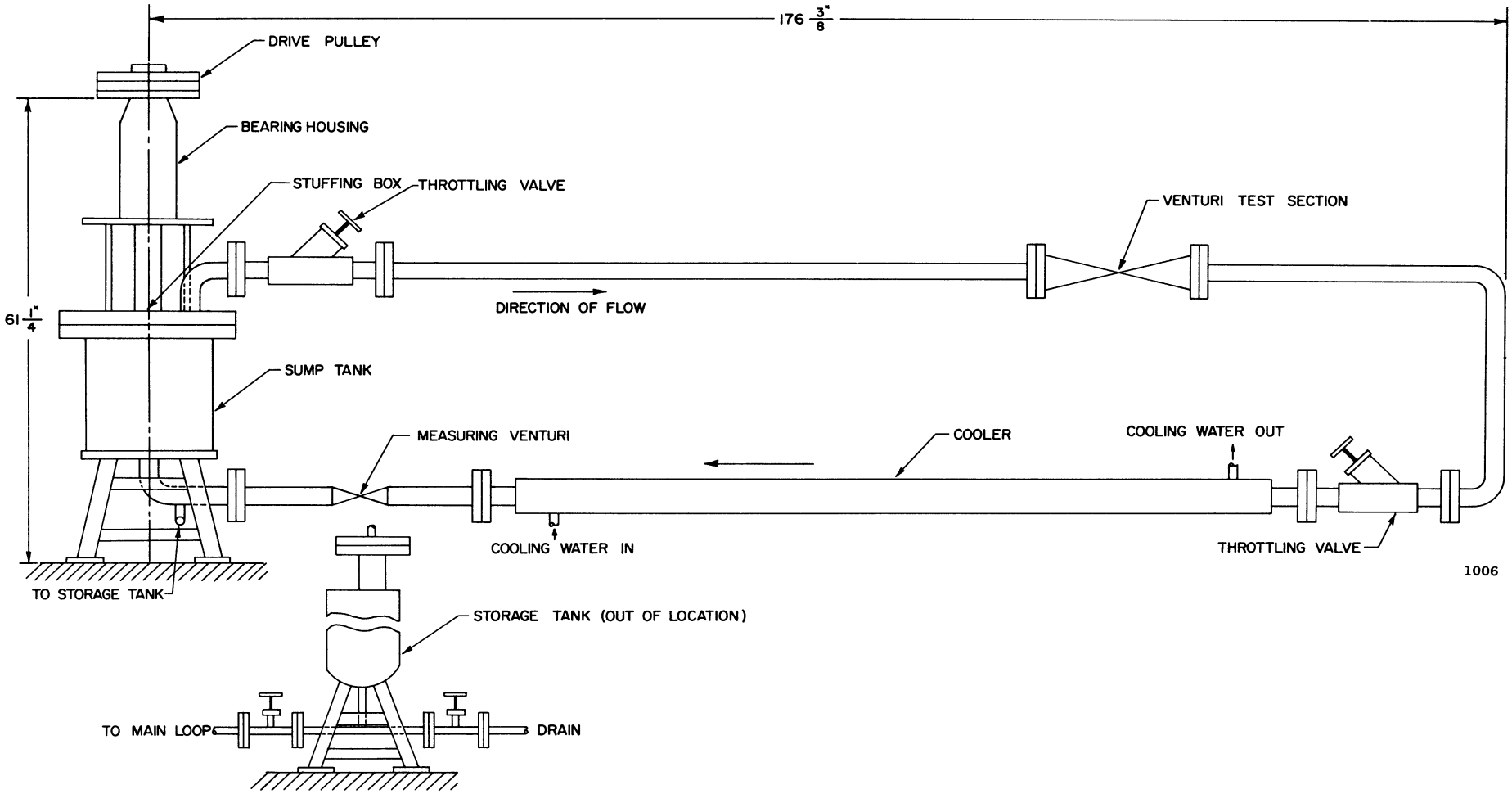

Fig. 3. Schematic Drawing of Overall Mercury Facility Layout

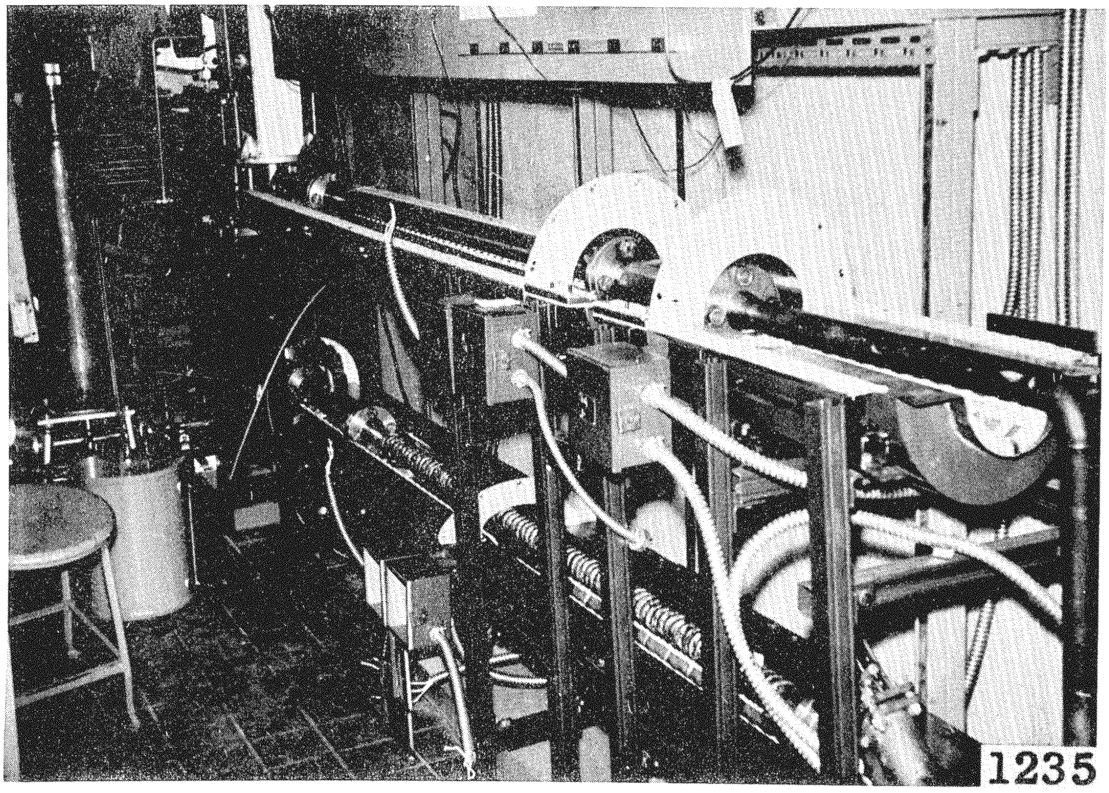

Fig. 4. Photograph of Mercury Facility with Top half of Heater Sections Removed

This is accomplished by the use of an exponential horn which is mechanically attached to the crystal transducer section. The horn acts as a velocity transformer, increasing the velocity of the standing waves propagated by the crystal.

The amplification which is obtained is a function of the ratio of the end areas of the exponential horn section (10). By increasing the input voltage to the maximum allowable, the amplitude of the lower surface can be increased to more than 2.5 mils double amplitude. The typical length of the overall "ultrasonic horn", i.e. the upper driver section with corresponding exponential horn, equals one wavelength of the acoustic oscillation propagated in it. Figure 5 is a schematic representation of a typical wave form showing the position of the nodes and anti-nodes along the length of the transducer assembly (8). It is obvious that if full capability of the assembly is to be used, the maximum amplitude must occur at the very end of the assembly. The horn tip must thus correspond to an anti-nodal point of the standing wave propagated along the assembly.

It may also be noted that the assembly attachment to the stationary holder must be made as close as possible to a nodal point (a point of zero amplitude) of the standing wave.

The generator or power source which supplied the required voltage to the crystal assembly is a commercial unit sold under the trade name of "Branson Sonifier".

The Branson unit supplies the required voltage at a nominal frequency of 20 kHz. This unit can be tuned by $\pm$ 3 kHz around the nominal 20 kHz to accommodate a replacement exponential horn of a different resonant frequency if such is required for other experiments. The exponential horn used in this study is of titanium cut and tuned to operate at 20 kHz with the Sonifier power supply.

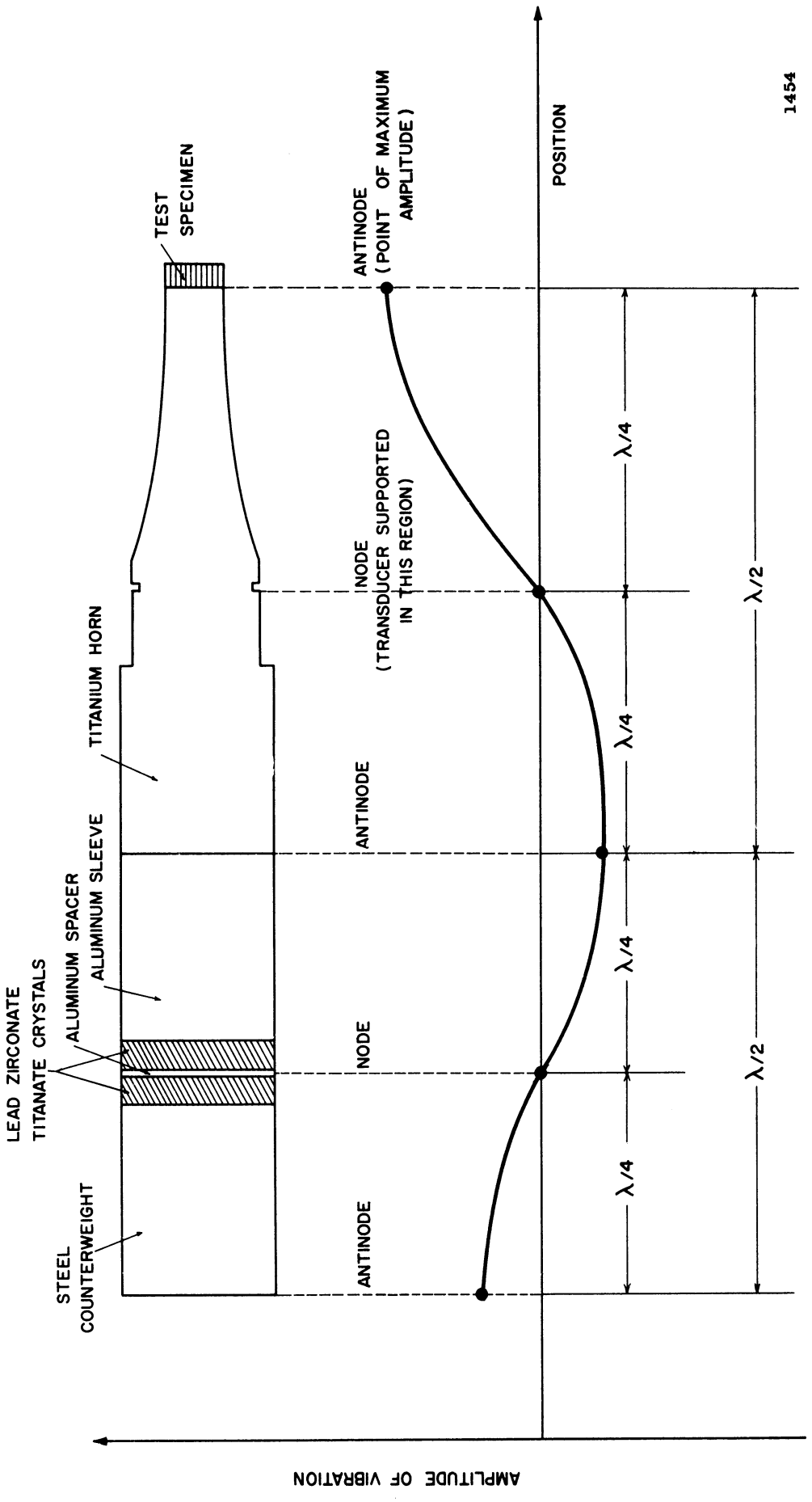

Fig. 5. Typical Wave Form Showing Position of Nodes and Antinodes on Transducer Assembly

Other pertinent information concerning the type of horn tip and adaptation of this piece of equipment will be related presently.

III. EXPERIMENTAL STUDY

A. Mercury Loop - Feasibility Study

1. Flow Patterns and Damage Studies

The flow pattern for the typical plate-type specimens used by Robinson (7, 21) when inserted into the cavitating region of the venturi, is somewhat analagous to cavitating flow over the leading edge of a pump blade, i.e., substantially translatory cavitating flow with a significant axial pressure gradient. It became evident in our past tests that this is not a particularly damaging type of flow. This was also evident in the tests of Barinka et al. (2) performed with a thin rectangular specimen with its face parallel to the flow.

If, however, a strong vorticity is superimposed upon a translatory flow of the type just mentioned, so that the vortex impinges in a suitable fashion upon a structural member or test specimen, the damage intensity can be increased by orders of magnitude. Also, while the specimen of Barinka et al. (2) (Figs. 6 and 7) was well adapted to a tensile stress, a different design was required if a compression test was to be undertaken since the test specimen would buckle under the compressive load.

A pin type specimen as shown in Figure 8 was selected to obtain rapid damage with a vortex flow and good compressive capability.

Early data on the pin specimens indicated that the rate of damage on such a specimen was orders of magnitude greater than that for the plate specimens. It was also noted that the damage rate was sensitive to the degree of cavitation as well as the trace water content of the mercury (6) (400 micro-inches per hour versus 1-5 per hour for conventional specimens was observed).

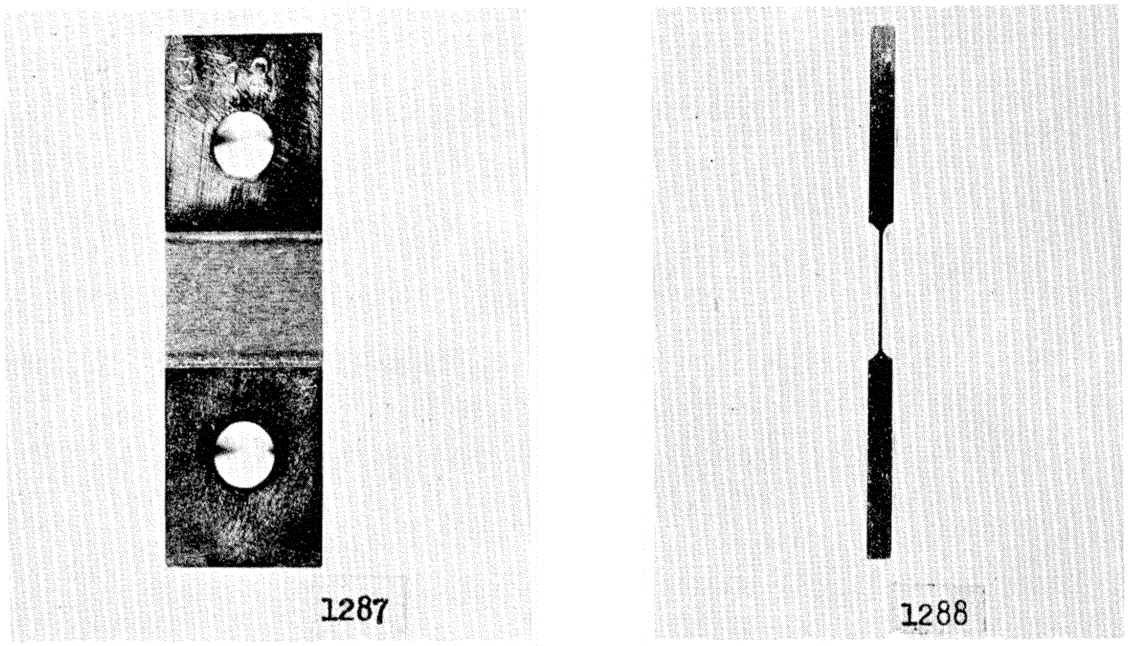

Fig. 6. Photograph of Previously Used Tensile Test Specimen

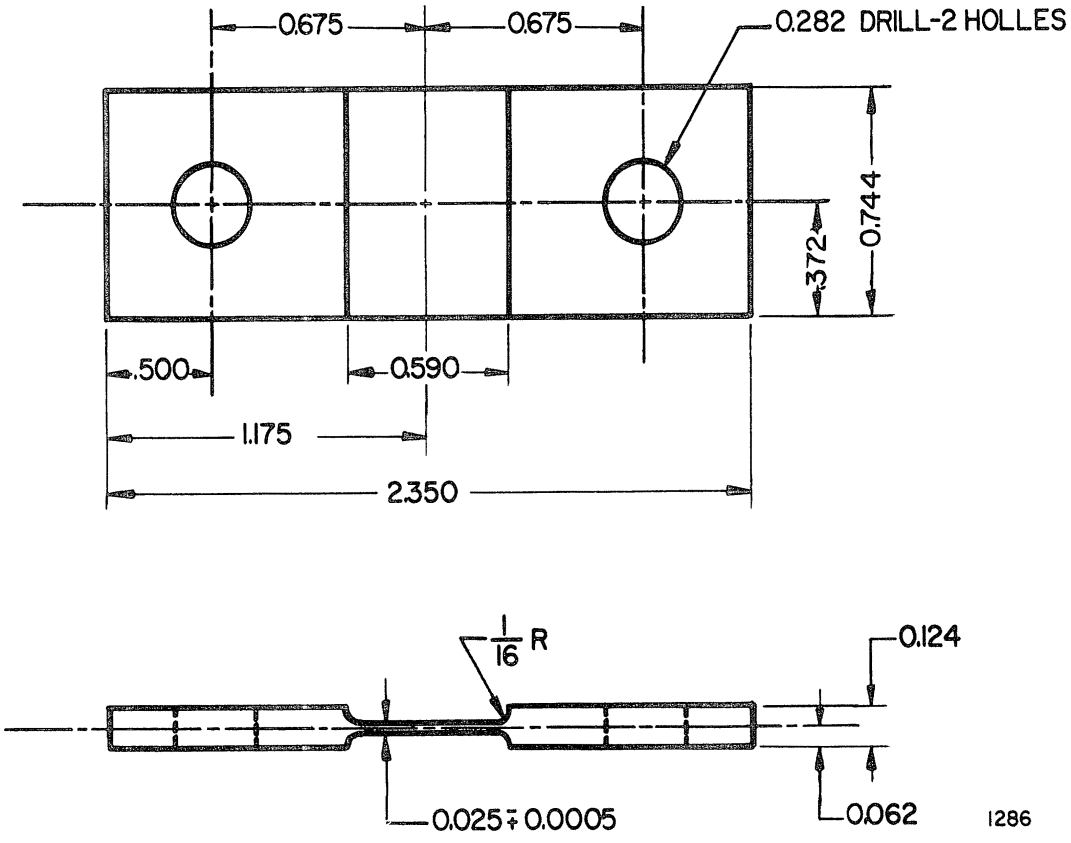

Fig. 7. Dimensional Drawing of Tensile Test Specimen

This dependence of the cavitation intensity upon specimen geometry can be justified if it is assumed that there exists an unsteady vaporous wake region behind the pin in the region of trailing vortices, consisting of more or less discreet vapor bubbles. By a suitable adjustment of velocity and downstream pressure, these bubbles can be caused to collapse on the downstream portion of the cylinder. Thus for a given velocity, the damage rate is very dependent upon the pressure differential across the pin, as this controls the location of bubble collapse, and the driving pressures for collapse, i.e. at low back pressure the trailing vortices collapse well into the fluid downstream of the pin, causing little damage.

In anticipation of the effect of cavitation cloud geometry and position on the rate of material attrition, the first study undertaken was to determine the effect of pressure drop across the venturi on damage rate.

a. The Tubular Pin Specimen

The pin specimens were fabricated from tubular stainless stell stock (0.049 inch wall) into the design shown in Figures 8 and 9. The specimens of Figure 8 were cut to a length of 4 1/4 inches, threaded 3/4 inch on each end with 1/4-32-NEF- 2A thread. A section 0.594 inches long with 1/32 inch radius on either end was machined in the center of the specimen. This length corresponds to the portion of the specimen in the flow field, which was machined to a wall thickness of 0.020 inches. The inner portion was accurately reamed to a diameter or 0.164 inches to obtain close control of the overall wall thickness.

The specimen shown in Figure 9 is an alternate form used in the latter half of the test program. The dimensions in the test section remained unchanged, although the specimen was of three piece construction. The center portion which contained the test

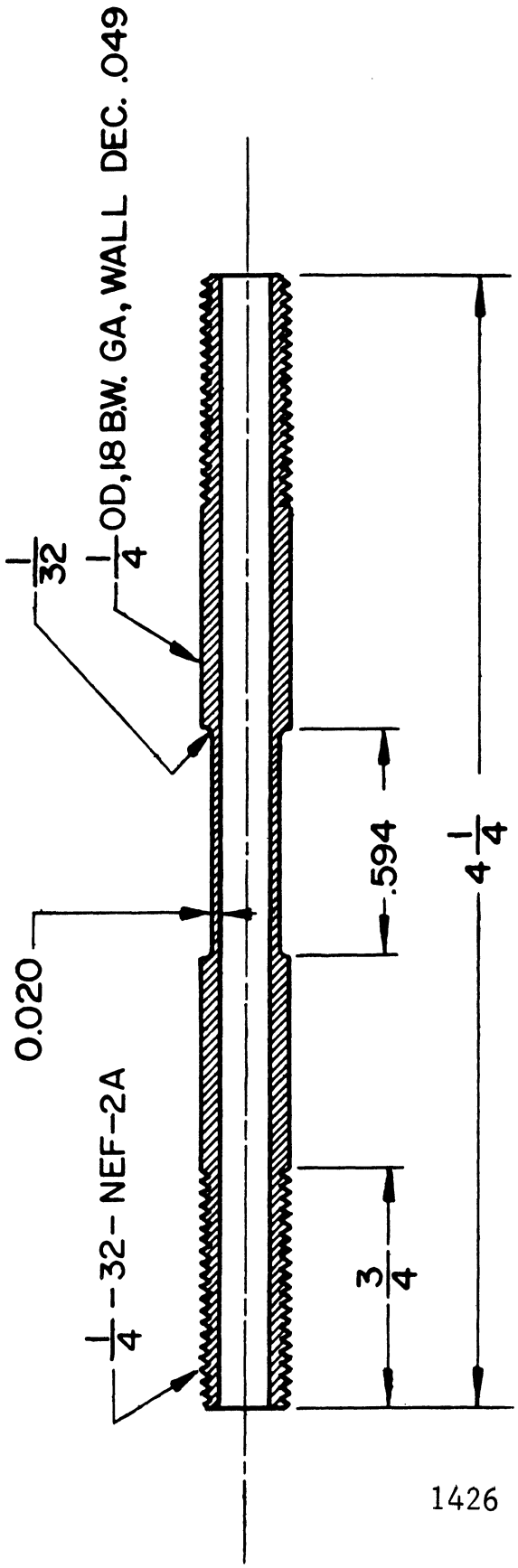

Fig. 8. Drawing of Tubular Test Specimen(pin)

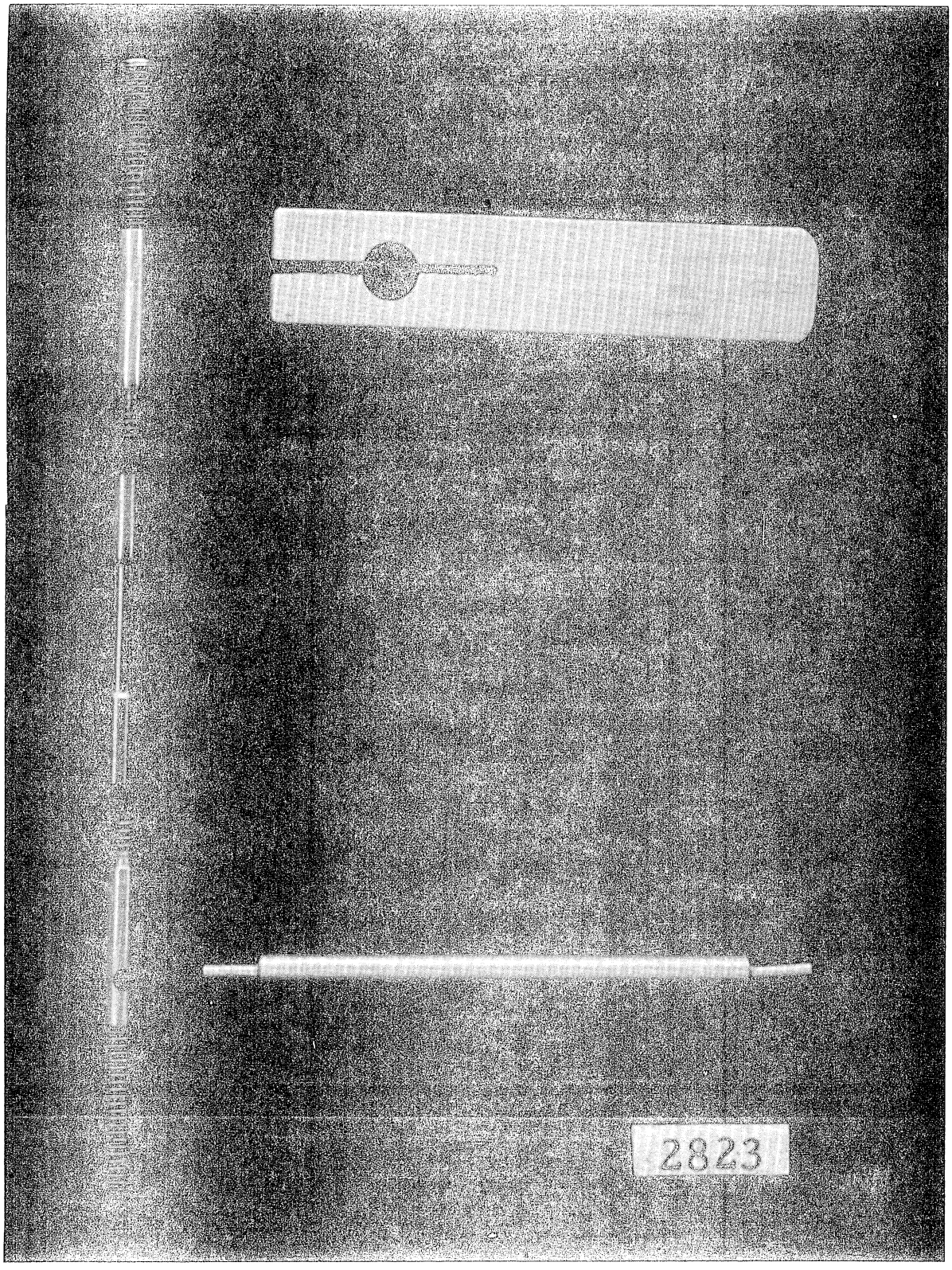

Fig. 9. Three Piece Tubular Test Specimen with Assembly Tools

section was 1.5" long and threaded internally with 1/8-20 threads. A special holding -tool was designed for tightening of the center section onto the two removable ends. Figure 9 is a photograph showing the test section and the assembly tools along with the removable ends.

b. The Venturi and Associated Test Facility

The stainless steel test venturi used in this investigation was of the same design and dimensions as that used previously by Robinson (7). A cut away drawing of this venturi is shown in Figure 10. The venturi incorporates a nozzle and a diffuser, both of which have an included angle of 6^{o}, separated by a cylindrical throat section 2.35 inches long and 0.5 inches in diameter. For the present study, the venturi was modified to allow vertical positioning of the tubular pin specimen.

The specimen, held in place by a larger cylindrical holder depicted in Figure 11, was constructed so that when screwed into the holder it could be positioned accurately by a holding shear pin inserted across its diameter. This provided stability for accurate positioning of the specimen both radially and vertically. The holder was marked in rings with 0.005 in. spacing to facilitate accurate vertical positioning of the specimen in the venturi as it was inserted for test.

A single specimen was gripped at both ends, extending across the entire fluid stream in the diffuser region of the venturi. The venturi was constructed to allow the center line of the specimen to be positioned 0.786 inches from the venturi throat exit. This position corresponded to the centerline position used by Robinson (7) in his investigation.

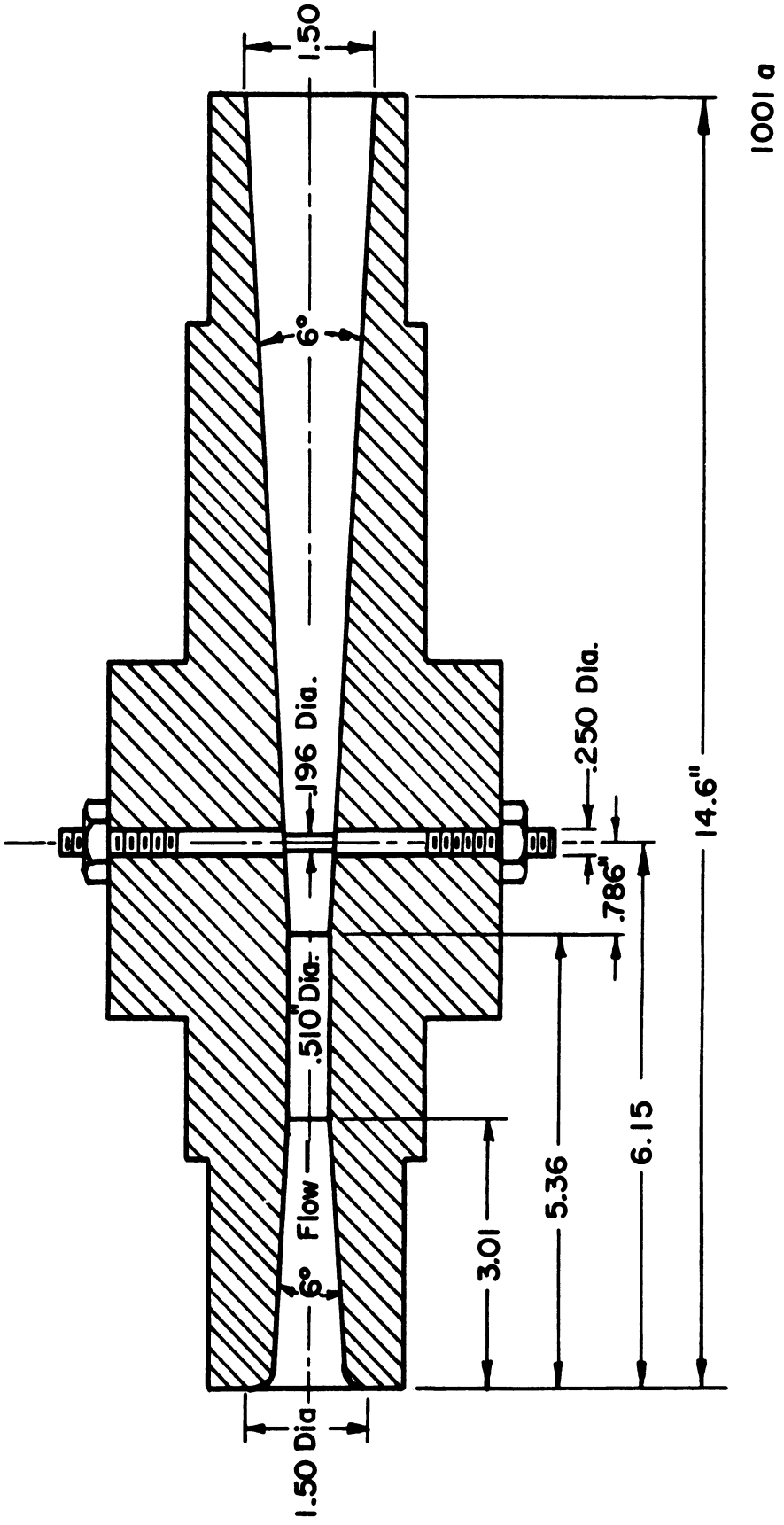

Fig. 10. Assembly Drawing of Tension Test Venturi

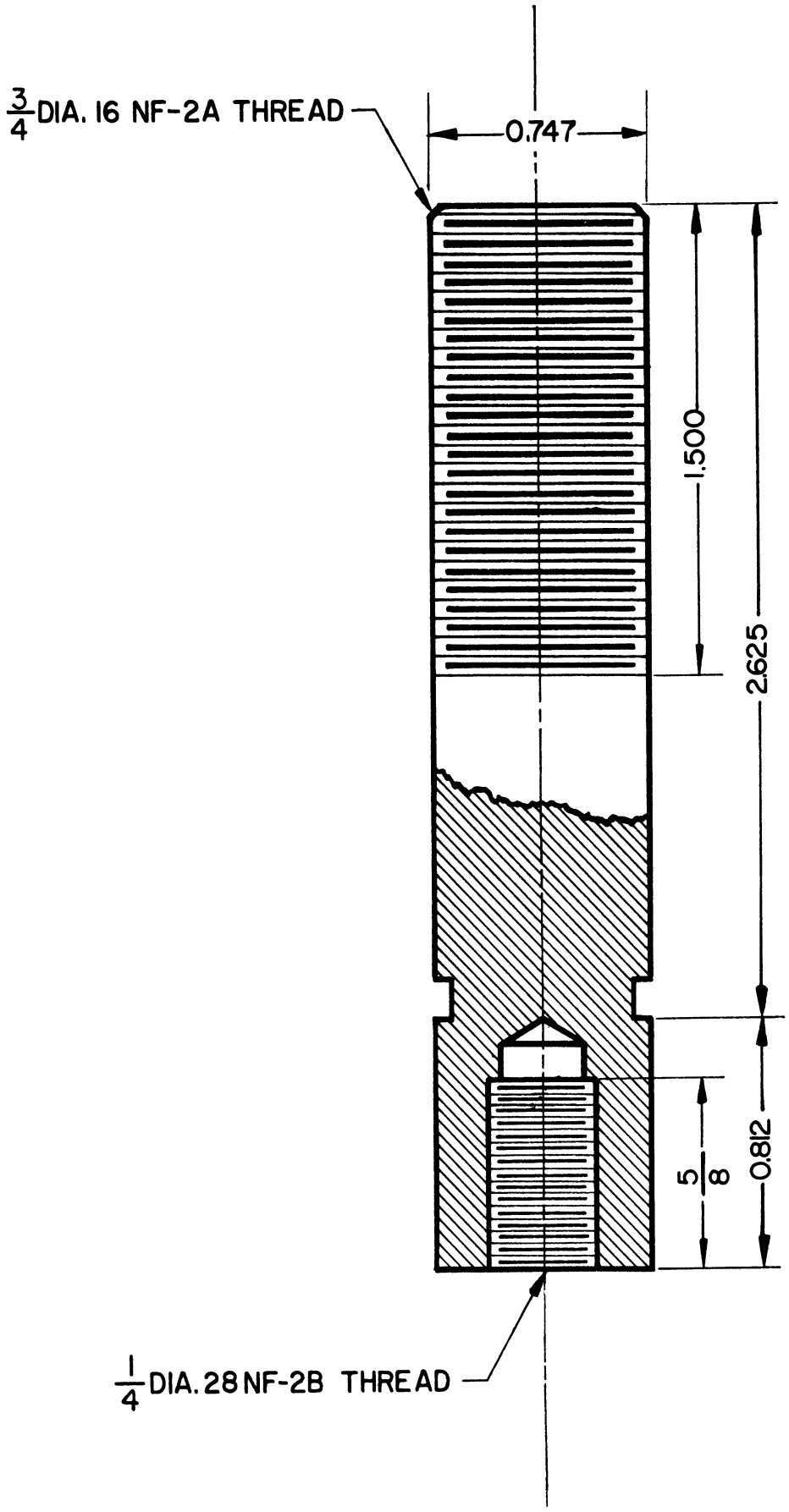

Fig. 11. Dimensional Drawing of Pin Specimen Holder

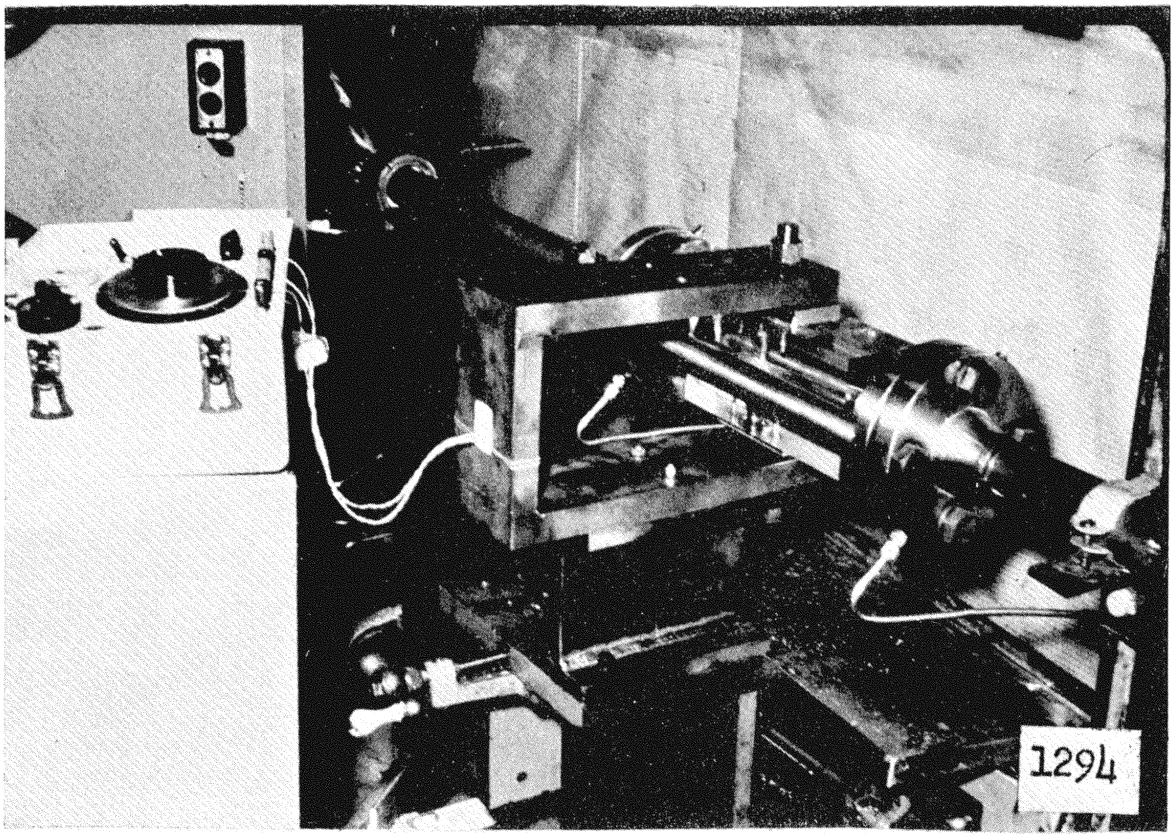

Fig. 12. Photograph of Tension Clamp and Venturi

The desired loads on the specimen were applied by using a heavy U-shaped steel block as shown in Figure 12. This "U-clamp" was instrumented with strain gages in a full bridge array in order to provide a method of determining the applied load. The specimen holders were placed through holes in the ends of the U-clamp. The external tensile or compressive load was applied to the specimen by tightening large nuts, on the threaded portion of the circular holder, against the face of the clamp.

c. Test Specimen Preparation

In the fabrication of the tubular pin specimens for initial tests, special precautions were taken in locating, cutting, and finishing of the center test section. It was felt that surface irregularities might influence the cavitating flow pattern. After the final machining step was completed the center section was sanded using progressively finer grit paper up to #600 to eliminate as many of the tooling marks from the surface as possible. The final polishing of the surface was done using a very fine abrasive and a small cloth wheel. The surface condition was monitored with a metallurgical microscope to obtain the desired finish.

Data acquired subsequently showed that such elaborated precuations were not really necessary as the damage was not substantially affected by the presence of surface scratches. (Fig. 19) For later tests, consequently, the surface finishes of test specimens were not so cirtically controlled.

The specimen was cleaned with an organic solvent to rid it of all machine oil and metal chips which would be detrimental to the exact weight measurements. The samples were then put into a vacuum distillation unit which was held at a temperature of 500°F under a vacuum for two hours. This process removed all deposits of volatile material from the external and internal surfaces of the specimen.

The samples are then weighed to $\pm$ 0.02 mg. on a Mettler Electronic Balance.

To minimize effects of residual mercury on the sample, each sample, when it was removed from the loop, was first cleaned with a soft brush to remove all visible mercury droplets from the surface. The specimen was then placed in a vacuum furnace for a period of 2 hours at a temperature of 600° F. This procedure seemed to remove the mercury particles or droplets visible with a metallurgical microscope (40 x) from the damaged surface. After cooling, the samples were again weighed and the weight loss was calculated.

d. Cavitation Conditions

With the specimen in position in the venturi, the loop was evacuated by use of a Cenco vacuum pump. After complete filling of the loop was assured, i.e. all excess air and air pockets removed, the loop was closed and readied for operation.

Since the testing was being done in a stainless steel venturi some method other than visual for determination of the state of cavitation had to be used. The nomenclature "sonic initiation, 1st mark, 2nd mark, etc . . . " had been used previously to describe degree of cavitation. These refer to particular cavitation conditions found visually or audibly in the venturi. It was anticipated that the

condition most acceptable for the program from the view of maximizing the damage rate would be close to sonic initiation, as this had been indicated by earlier experiments. "Sonic initiation" here refers to the condition which can be identified by the first slight audible crackle detected using a stethoscope pressed against the venturi adjacent to the test specimen.

An experiment was undertaken to determine the point of sonic initiation as a function of venturi inlet and outlet pressure as the flow velocity was increased (Fig. 13). The fluid velocity is first set by adjusting the speed of the pump. The venturi inlet pressure was recorded with the mercury flow just greater than that for the start of the cavitation condition required. The downstream valve of the mercury loop was then adjusted until the sound emanating from the venturi was just audible. This point was rechecked by closing off the downstream valve until all audible cavitation stopped and then reopening to the "sonic initiation" point. In Figure 13, the curve to the right depicts the venturi inlet pressure. To the left of this curve is a curve of venturi outlet pressure for conditions of sonic initiation. Points along these curves were reproducible to $\pm$ 4 psi. The shaded region between these two curves is an area for the venturi discharge pressure where no cavitation would exist. The area to the right of the inlet pressure curve cannot be reached due to equipment limitations. These curves were used to select the operating conditions for the desired velocity.

2. Cavitation Damage Studies

a. Effect of Pressure Drop

In order to provide a datum plane with which to compare future tests and also to find the cavitation condition which would provide the maximum damage rate, a study of pressure drop versus damage was done at flow velocities of 30 and 25 f/s. The cumulative results are shown in Figures 14 and 15. These plots both consist of families of curves at different venturi pressure drops, for two different flow

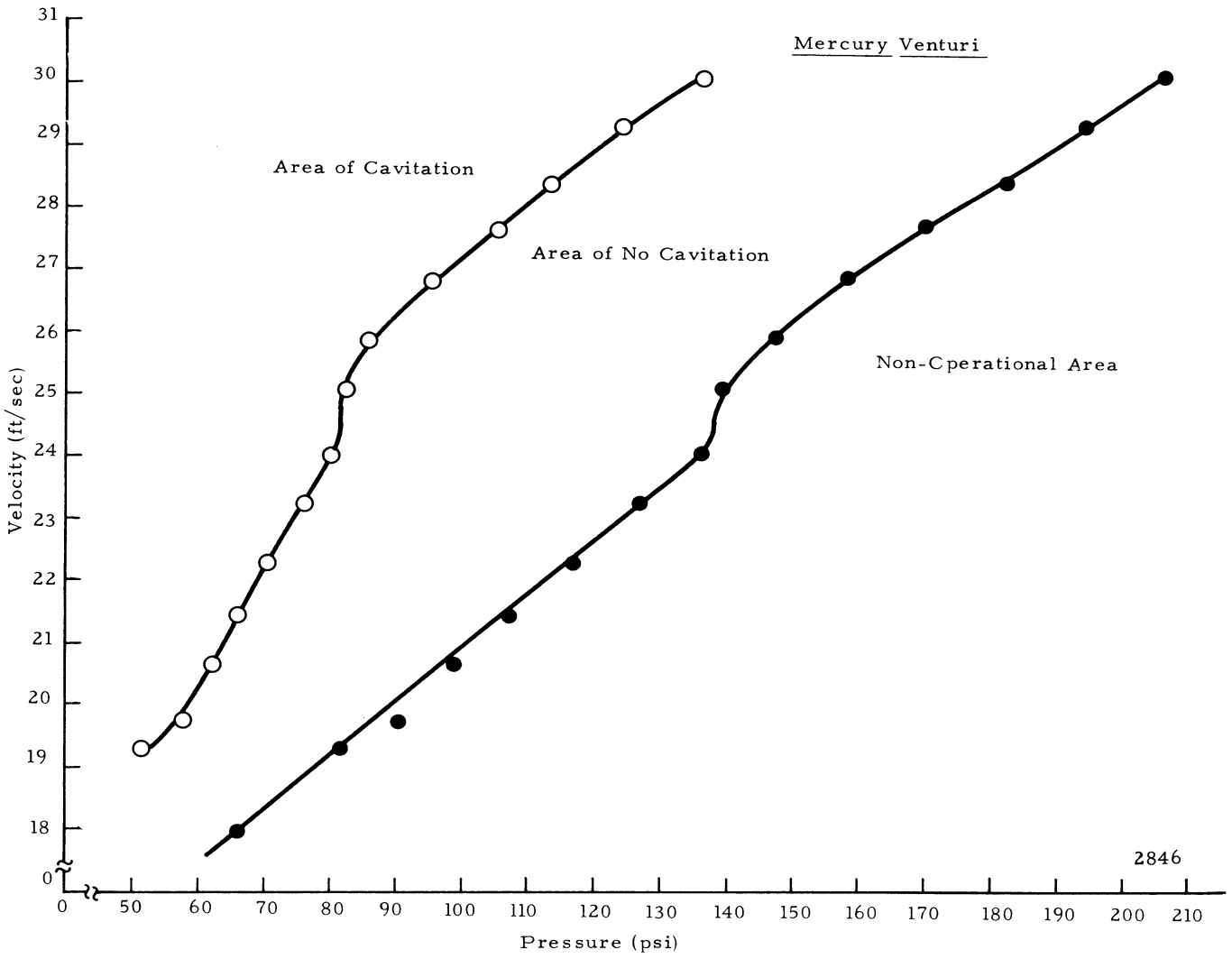

Fig. 13. Sonic Initiation Discharge and Inlet Pressure as a Function of Velocity

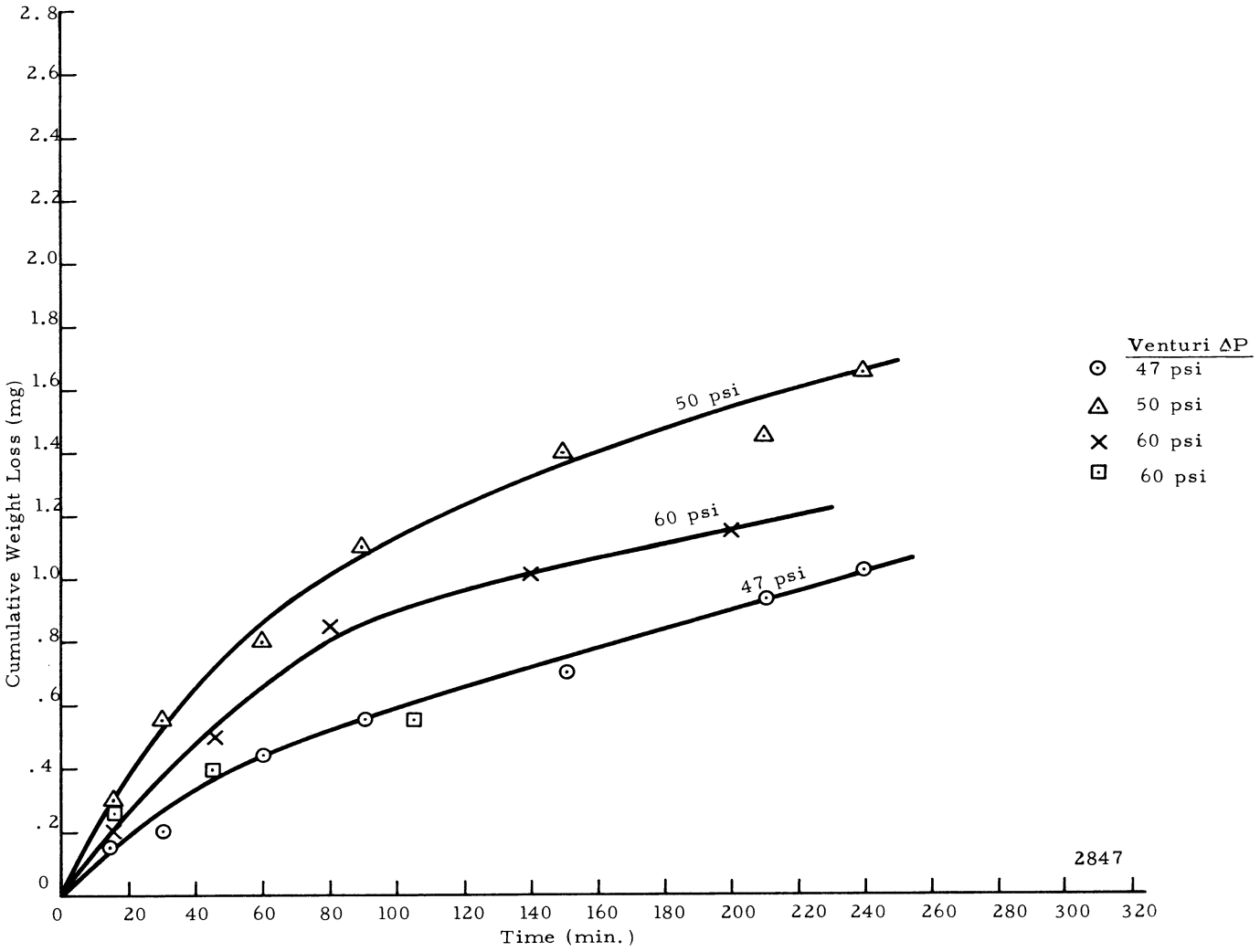

Fig. 14. Cumulative Weight Loss as a Function of Time (304 SS in Mercury, 25 fps)

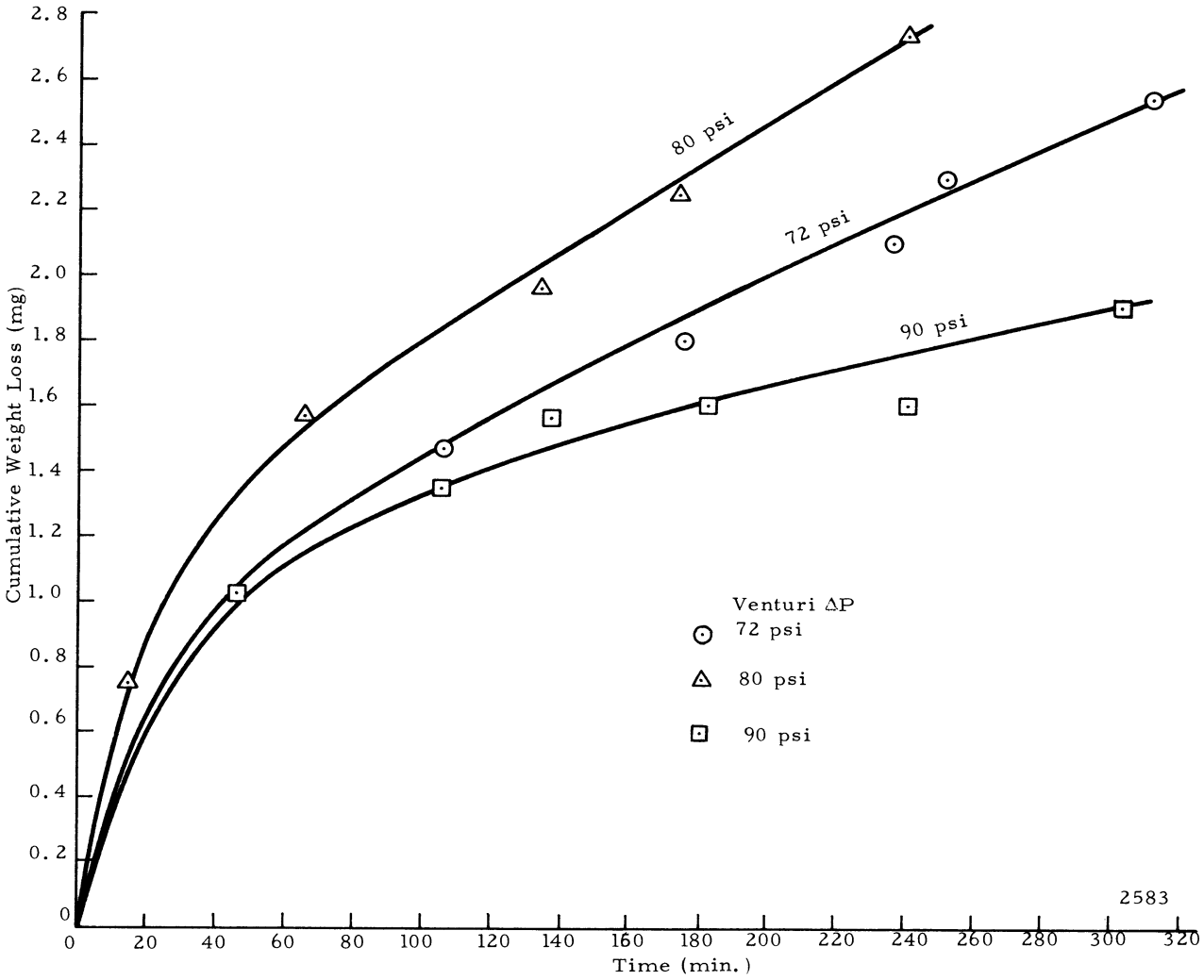

Fig. 15. Cumulative Weight Loss as a Function of Time (304 SS in Mercury, 30 fps)

velocities. Comparison of the two velocities shows that as the velocity increased the damage rate increased. The rate curves, Figure 16, have been plotted by calculating the slope of the latter portion of each damage versus time curve. The damage curves obtained in this manner show a sharply peaked damage rate at 50 psi pressure drop for the flow rate of 25 ft. per sec, and at 80 psi pressure drop for 30 ft. per sec.

The shapes of these curves are explicable in terms of the particular pressure fields. In the lower pressure drop region, i. e. higher back pressure, the pressure is high enough to suppress all but a few bubbles. Their collapse is very close to their initiation point, and damage is quite light, since the bubble size and number are small. As the downstream pressure is decreased a larger number of bubbles are nucleated and collapse upon the surface of the specimen until a maximum damage rate is reached. This flow condition comprises a situation in which the cavitation field is substantial enough to accommodate a large number of damaging collapses as well as having the cavitation bubble field collapse in close enough proximity to the specimen surface to cause damage. As the downstream pressure is decreased still further the cavitation field collapse progresses further downstream, and fewer of the damaging bubbles collapse in an area adjacent to the surface. This in turn decreases the amount of damage to the specimens even in a situation where the number of bubbles initiated in the venturi is large.

b. Observable Damage

1.) Damage Area: The samples which were run showed a pattern of damage at each side of the sample as shown in Figure 17. The photograph shows a darkened area of damage which indicated that the damage region is not strictly vertical but has a region of damage tapering at both ends in the downstream direction. The center section reflects a higher velocity region in which the cavitation cloud is swept just slightly downstream before collapse occurs. However, due

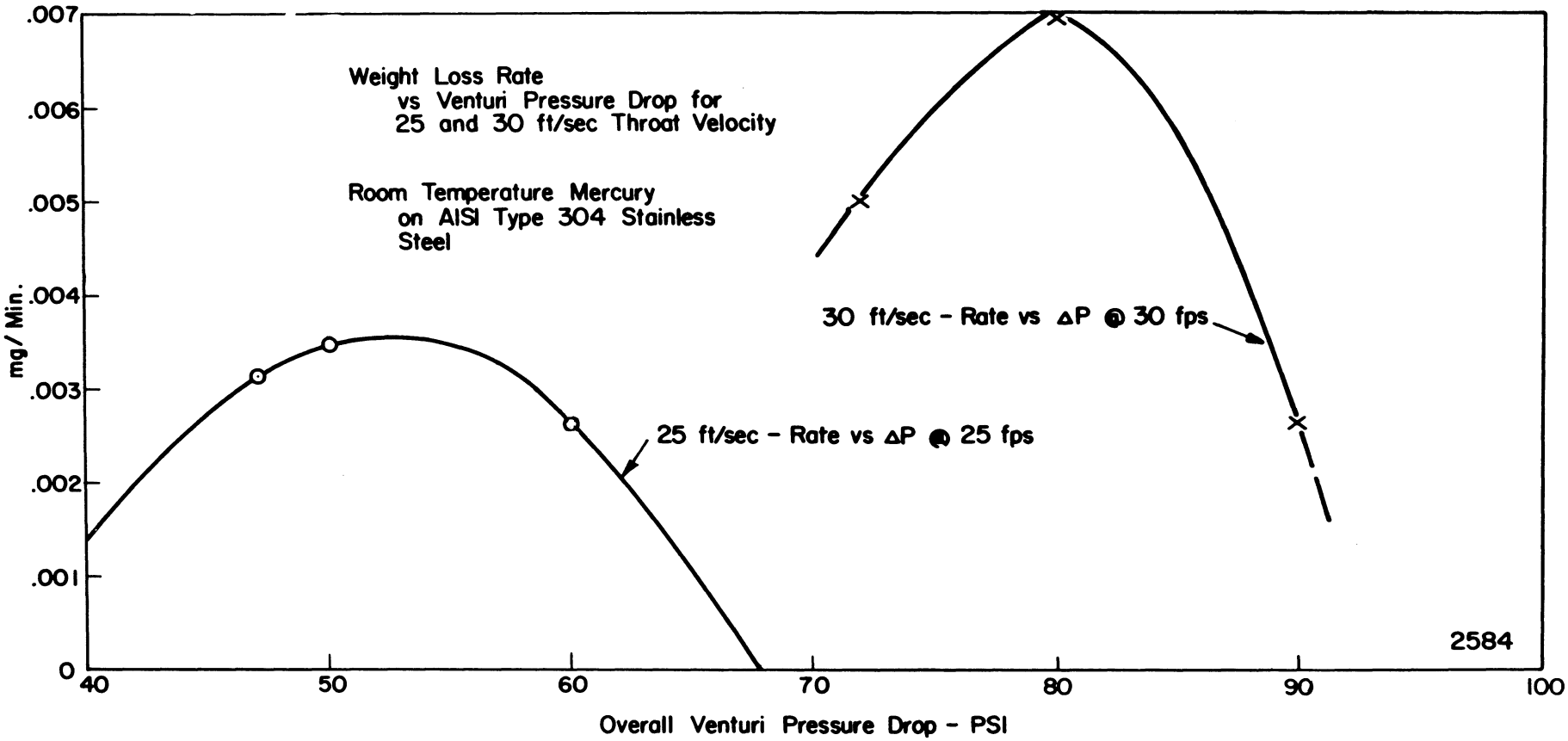

Fig. 16. Damage Rate as a Function of Pressure Drop and Flow Rate in the Mercury Venturi

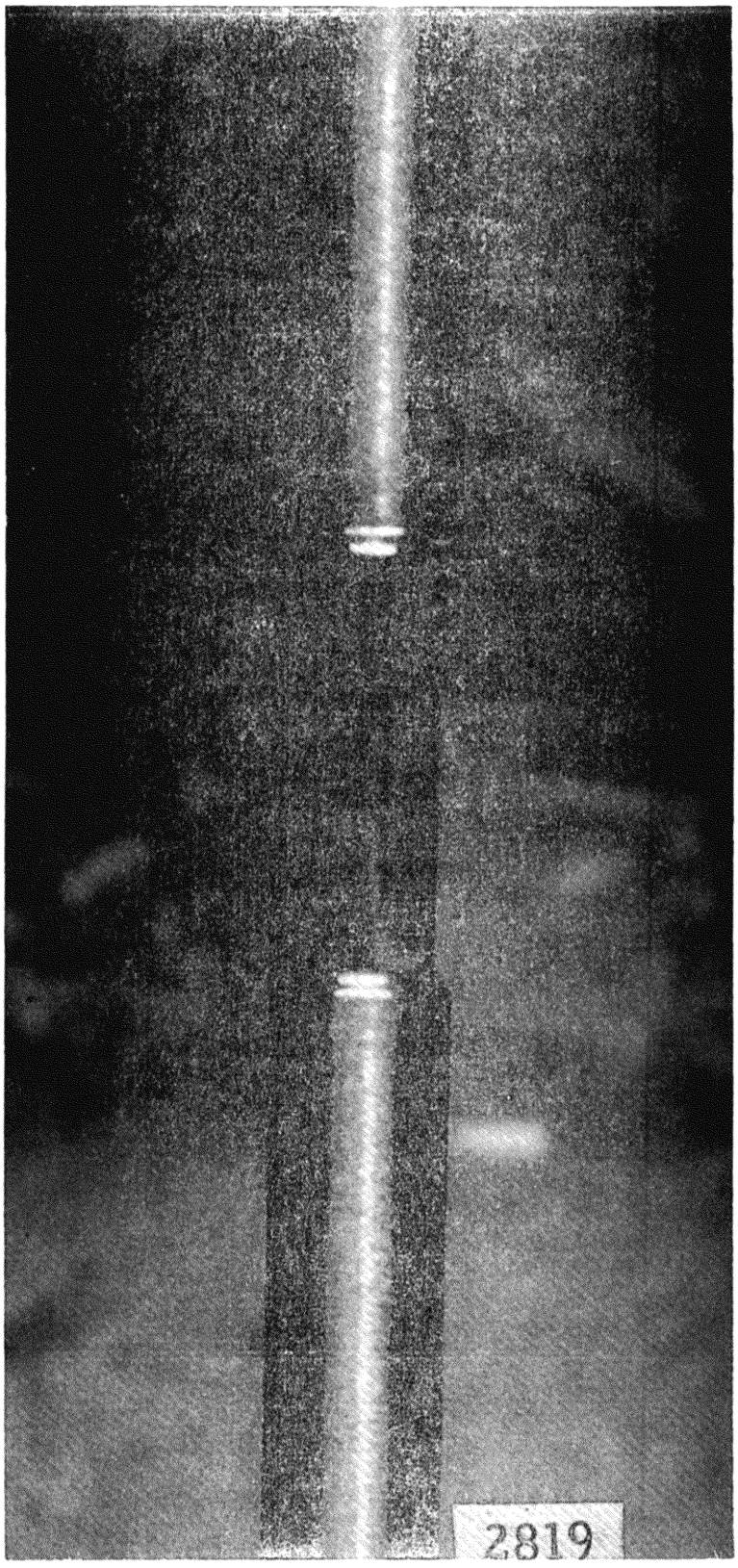

Fig. 17. Typical Pin Damage in Mercury Venturi

to the higher velocity the separation point moves upstream. The photograph in Figure 18 is a close-up taken with a rolliflex microscope camera. The magnification is approximately 40x. The enlarged picture shows that the damage has a clean line of demarcation except in certain individual spots where there appears to have been a protrusion to initiate cavitation. Close examination did not reveal the cause of these areas. However, they seemed to be present on all samples.

The location of the start of the damage area was checked on a number of the pin specimens. This was found to be close to 78^{o}-80^{o} around from the upstream axial centerline of the sample. This radial position did not change as the pressure drop was varied.

2.) Surface Effects: In order to determine the effect of surface scratches and blemishes on the damage, a previously scratched specimen was photographed after being run for two minutes at a velocity of 30 fps. and a pressure drop of 70 psi. The sequence of pictures in Figure 19 was taken with the center of each frame at 10 degree intervals from 60^{o} to 180^{o}. As can be seen, the scratches which were on the surface had no effect on either the amount of damage or the area of damage. One interesting observation which can be made of the damage photograph is that the damage starts in a region approximately 80^{o} around from the upstream center as mentioned previously. The greatest number of pits, however, occurs at a position of approximately 100 degrees. The damage in adjacent areas decreases; however, a number of larger pits are apparent around the specimen to approximately 165^{o}. From this point to the back of the specimen (180^{o} area) no further damage occurs. Another interesting observation which can be made here is the apparent increase in pit population again at 135^{o}.

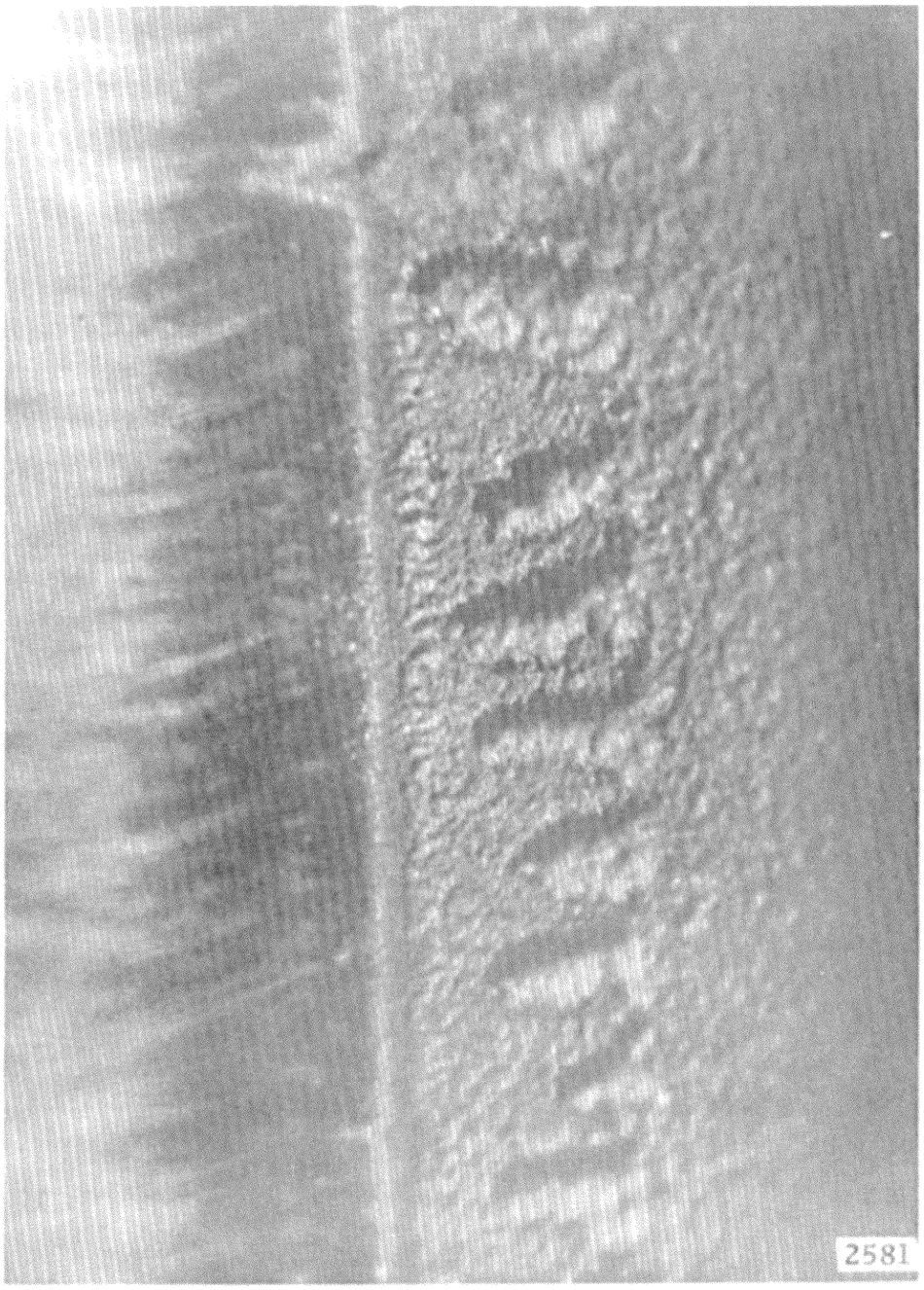

Fig. 18. Close up (40x) of Damage Demarcation Line on Tubular Damage Specimen

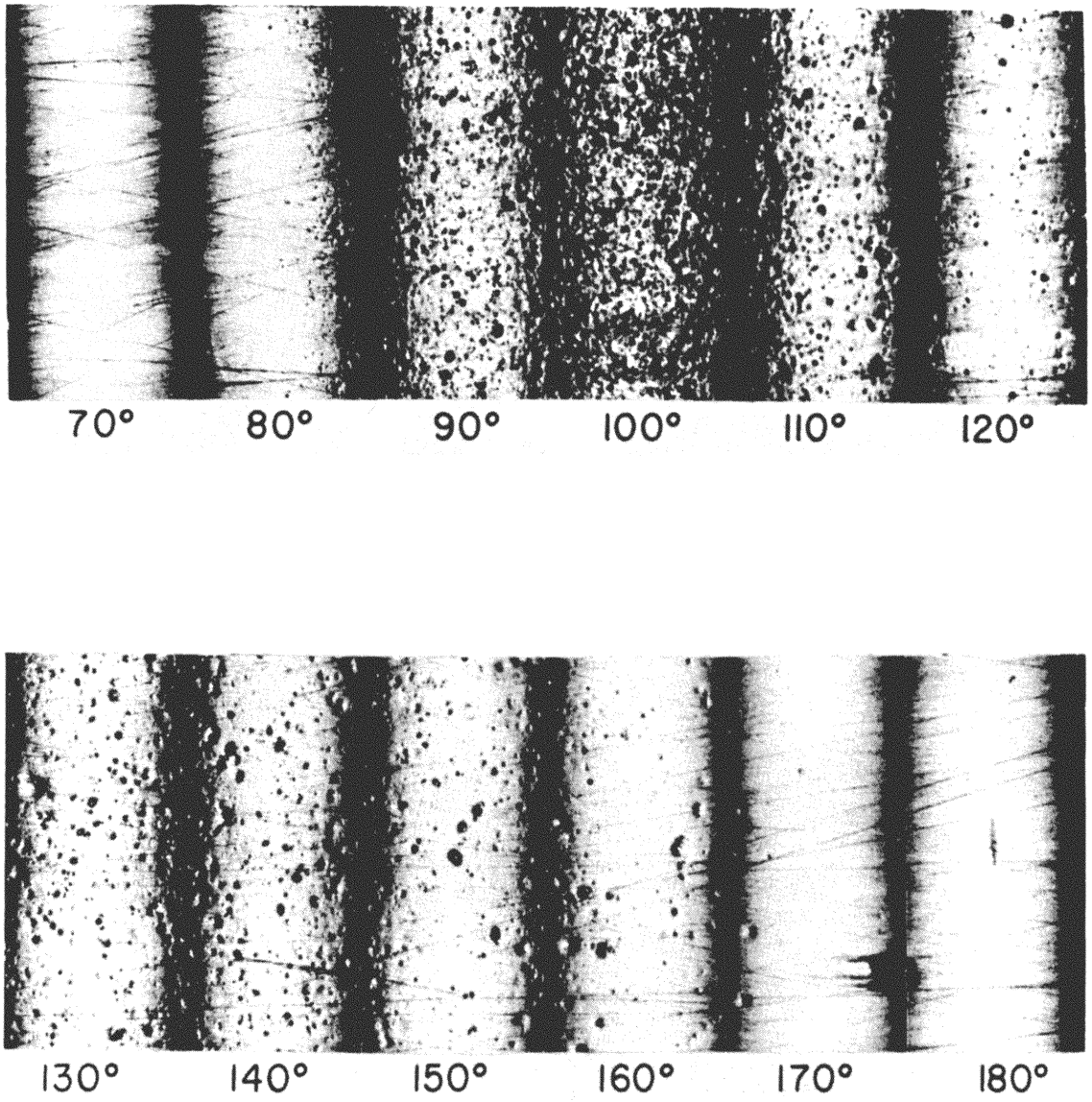

Fig. 19. Effect of Surface Scratches on Cavitation Damage of Tubular Pin Specimens

3. Effect of Surface Stress:

A very short experiment was undertaken to try to photographically differentiate between damage to specimens under tension, compression, or zero stress. Three highly polished specimens were run for a period of 1.5 minutes at a velocity of 30 fps. and a pressure drop of 71 psi. The three sequences of pictures shown in Figure 20 are again in 10 degree intervals strating from a center on 70 degree position. Sequence A is the specimen with no force applied, B is the specimen in compression and C is the specimen in tension. The total stress on the specimens was approximately 31,000 psi (88% yield strength). It is interesting to note that the specimens in tension and with zero force applied have approximately the same amount of visible damage. The specimen which was in compression shows very little damage in the same period of time. The specimens with the greater amount of damage also show a greater pit population at approximately 135^{o} as was noted on the previous sample. It is also interesting to note that on all three samples the pits which appear further around the sample i.e. 120^{o} to 165^{o} seem deeper and larger than those which appear in the region around 90^{o} to the upstream side. The interesting information which is apparent from these sequences of photographs is the following:

1.) The effect of compressive stress on the cylindrical specimen is to drastically decrease the number of small damage pits in the initial stage of cavitation attack. Assuming that these are primarily responsible for eventual fatigue failures, it may be that applied compressive stress would substantially increase the incubation period.

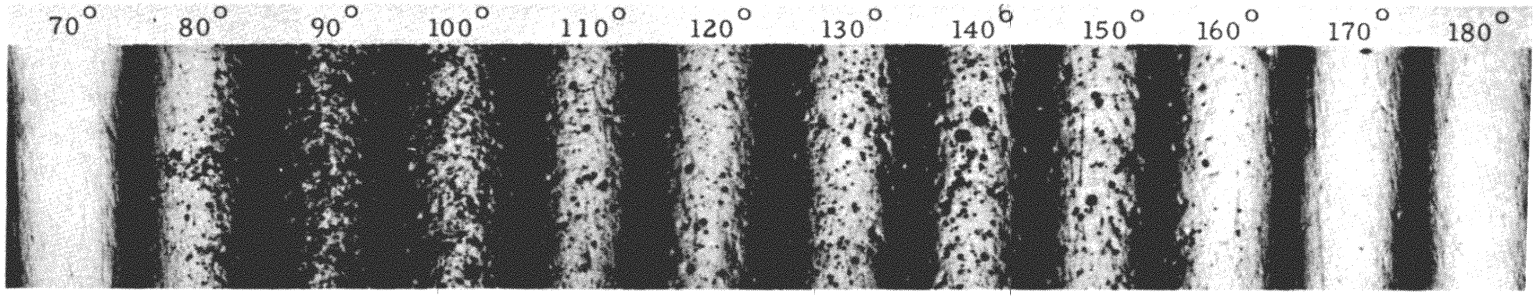

Sequence A- No Applied Force

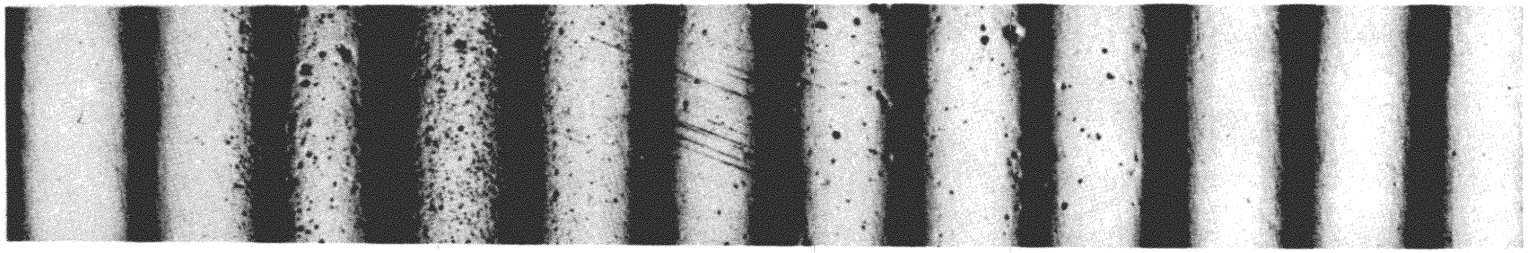

Sequence B-Compressive Force

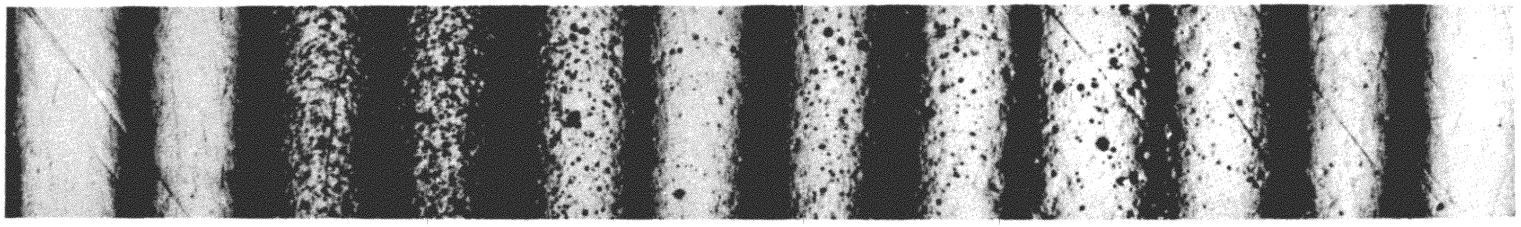

Sequence C-Tensile Force 2820

Fig. 20. Effect of Surface Stress on Damage for Short Duration Tests

2.) The compressive stress on the sample does not seem to decrease the number of large pits present in the damage area indicating that certain of the bubble collapses will initially cause large pits in relatively the same number regardless of the stress present on the sample.

3.) The pit spectra with zero force and tension are quite similar. There are five principle areas of damage as progression is made around the specimen: 1) the start of the cavitation damage region at 78^{o}-80^{o}, 2) high pit concentration area from approximately 90^{o}-110^{o}, 3) relatively sparsely pitted region from 115^{o} to 130^{o}, 4) another high density region from 130^{o}-145^{o}, and 5) no damage area from approximately 165^{o}-180^{o}. Each of these areas correspond to different positions of the cavitation cloud contact with the specimen surface.

B. The Water Loop - Flow Visualization

To obtain a visual indication of the flow pattern, considering the opacity of the mercury, it was necessary to make initial studies of the cavitation field around the cylindrical specimen in the water loop facility. Three separate investigations were made, 1) high speed motion pictures of the flow, 2) bubble damage capabilities in this configuration, and 3) pressure profiles around the specimen.

1.) High Speed Cinematography

A motion picture study of the cavitation field which surrounds the cylindrical specimen was undertaken using a Fastex camera ($\sim$ 15,000 frames/sec. max.). To enable the study of the cloud and its behavior near the cylindrical specimen, a plexiglas venturi was used (Figure 21), which corresponded

dimensionally to the stainless steel venturi used in the mercury loop. The plexiglas venturi was cut to accomodate a "light-pipe"(Figure 22) in the exact dimension of the cylindrical tension-compression specimen. The entire assembly was then installed into one of the loops of the water facility. It was positioned so that the lens of the camera could be directed toward the end of the specimen. This allowed the viewing of the cavitation field in a direction perpendicular to the specimen and lens. Fig. 23 is a resultant sequence of pictures showing the wake which was generated at the edge of the cylinder. As can be seen, the cavitation cloud starts just aft of the center plane of the cylinder. The two cavitation clouds from each side oscillate alternately back and forth toward and away from the center of the downstream portion of the cylinder.

The free stream velocity (U) was 50 feet per second. Film marker stripes, exposed by a 60 cycle source to produce 120 light pulses per second were used to determine the average shedding frequency of the cavitation cloud from the cylinder. The average number of frames between light pulses was 61. Since the pulse interpause was 1/120 second the time per frame was 1.36×10^{4} seconds (framing rate of 7.38×10^{3} frames/second). Sequences of individual frames as in Fig. 24 were investigated and the shedding frequency was calculated from the data. The shedding from one side required on the average 3.8 frames. The shedding period thus claculated was 5.168×10^{-4} seconds with a resulting shedding frequency (f_v) of 1.935×10^{3} kHz. Lienhard (11) has compiled a large quantity of data on vortex frequency and Reynolds number correlations. He arranges his data in a single plot in

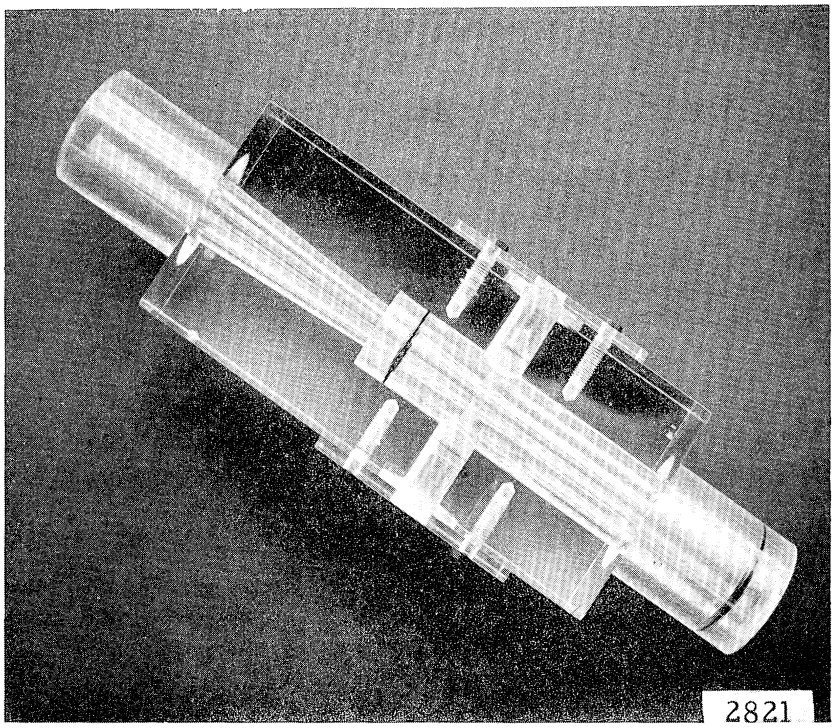

Fig. 21. Plexiglas Venturi Used for Photographic Study in Water Loop

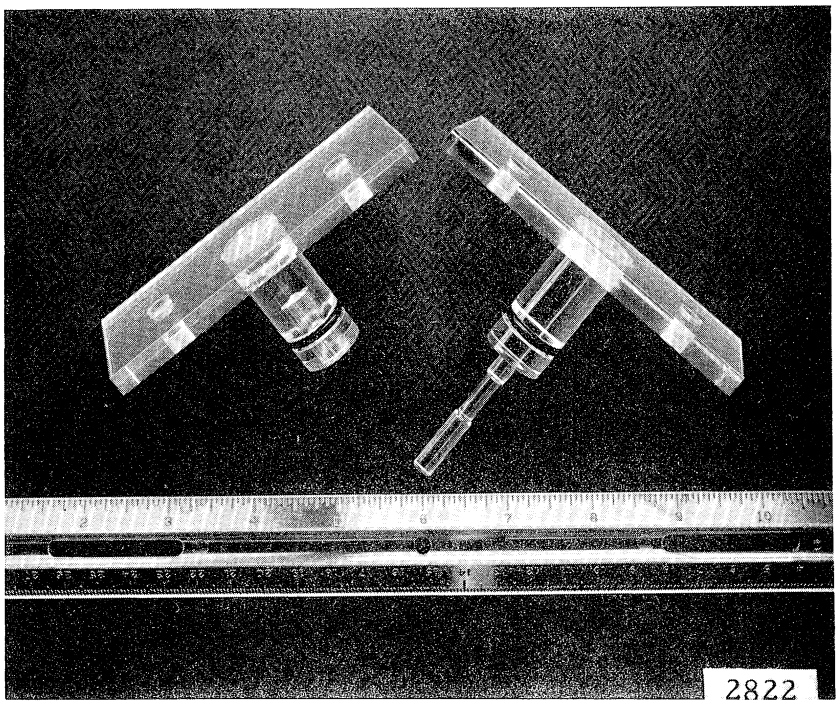

Fig. 22. Plexiglas Lite Pipe for Study of Flow Around Tubular Pin Specimen

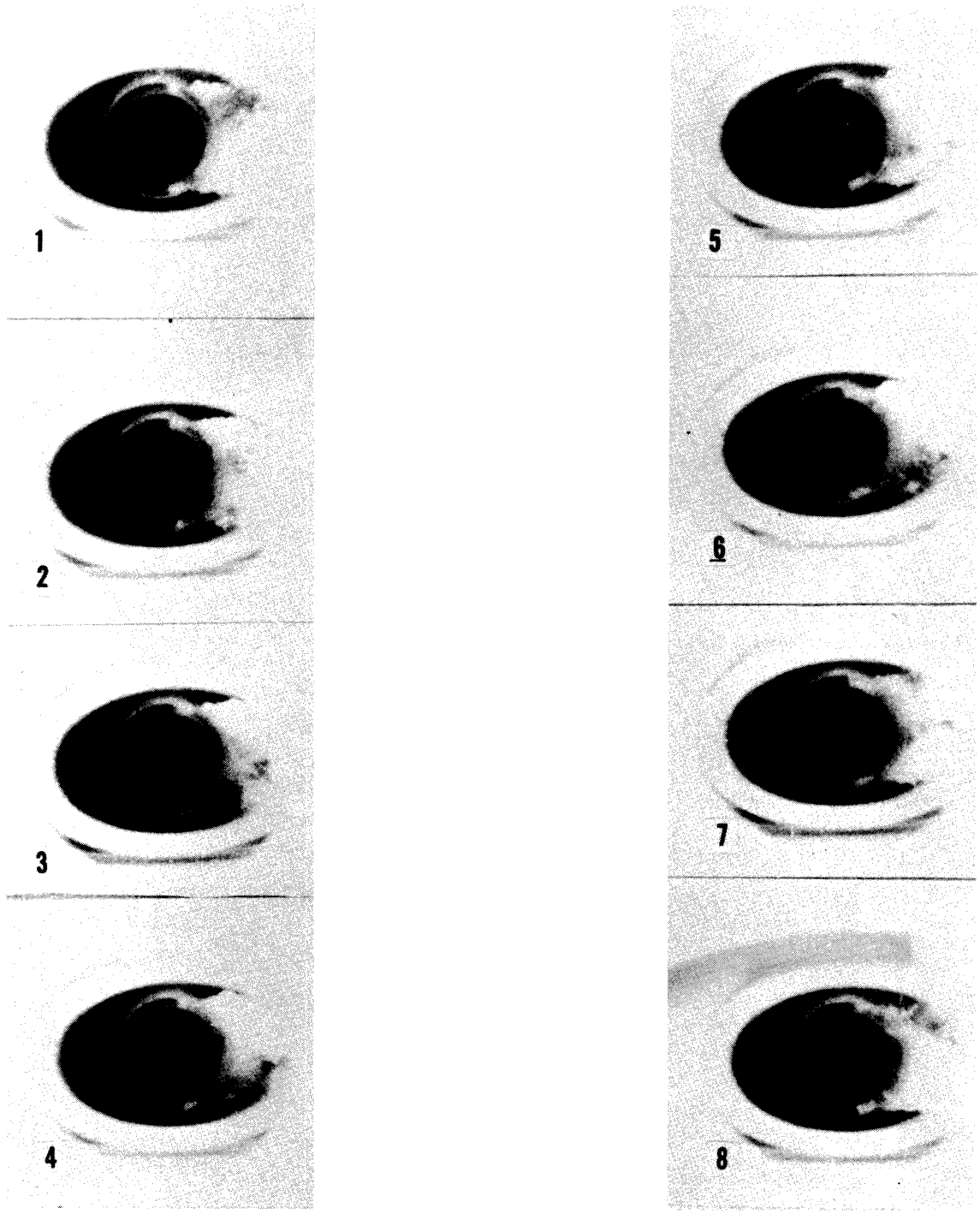

Fig. 23. Photographs of Oscillatory Flow Around Tubular Pin Specimen

which he considers:

$$St_v = fn(Re)$$

where $St_v = \frac{f_v L}{U}$ Vortex Strouhal number

f_v = Shedding frequency

L = Characteristic length (pin diameter)

U = Free stream velocity

The Strouhal number calculated from the photographs taken here at our laboratory was 0.632 at a pin Reynolds number of 5×10^5. In the region ($10^5 < Re < 3 \times 10^6$), which Lienhard (11) calls the "Laminar to turbulent transition in the boundary layer on the cylinder," he predicts, from all existing data to the time of his publications (1966), a Strouhal number between 0.2 and 0.47. He also comments that this data region holds a large uncertainty and needs further refinement and data. The presently observed Strouhal number then is at least of the expected order of magnitude.

One important difference between our experiment and Lienhard's data is the presence of a diffuser wall in close proximity to the test cylinder. Its effect on the Strouhal number can only be postulated. Since the oscillating cavitation cloud encounters an adverse pressure gradient in the area aft of the pin, the bubble wall collapse velocity would tend to be increased. This increase might be associated with an increase in shedding frequency, thereby increasing the magnitude of the Strouhal number. It is therefore to be expected that the Strouhal number as found in this work would be larger than that found in a straight duct.

Fig. 24 and 25 are taken with a graphic still camera. Fig. 24 shows the cloud formation around the pin, with the heavy cloud visible between 90 and 100 degress from the leading axial centerline of the cylinder. Fig. 25 shows a side view of the cloud as it appears perpendicular to the flow.

2.) Bubble Damage

Previous work by Noell (12) and Wood, et al. (13) had indicated that the damage effects of a cavitation field could be quickly pinpointed by using a coating applied to the surface on which the cloud impinged. In their study they applied a Krylon paint which damaged sufficiently slowly to allow visual determination of areas where later extensive damage might be expected.

This technique was tried in our water loop; however, the adhesion of the Krylon film to the 304 stainless steel cylinders was not adequate. At a throat velocity of 50 ft/sec the film was very quickly torn away. Although several different coatings were tried, the same problem remained. There was no way of determining the effect of the cavitation bubble collapse on the film since the entire film was removed. It was found that the film, to be of any used, must be more firmly attached to the cylinder. One such film which was used with a good degree of success was an electroplated cadmium film.

The specimens were plated with different thicknesses of cadmium by adjusting the time of exposure in the electrolytic tank. The cadmium plating was applied at a voltage of 2 volts and for times of 5, 10, and 20 minutes. The thickness of the film varied correspondingly with the exposure time. After plating, the specimens were placed in the water loop facility and run for 15 minutes at a

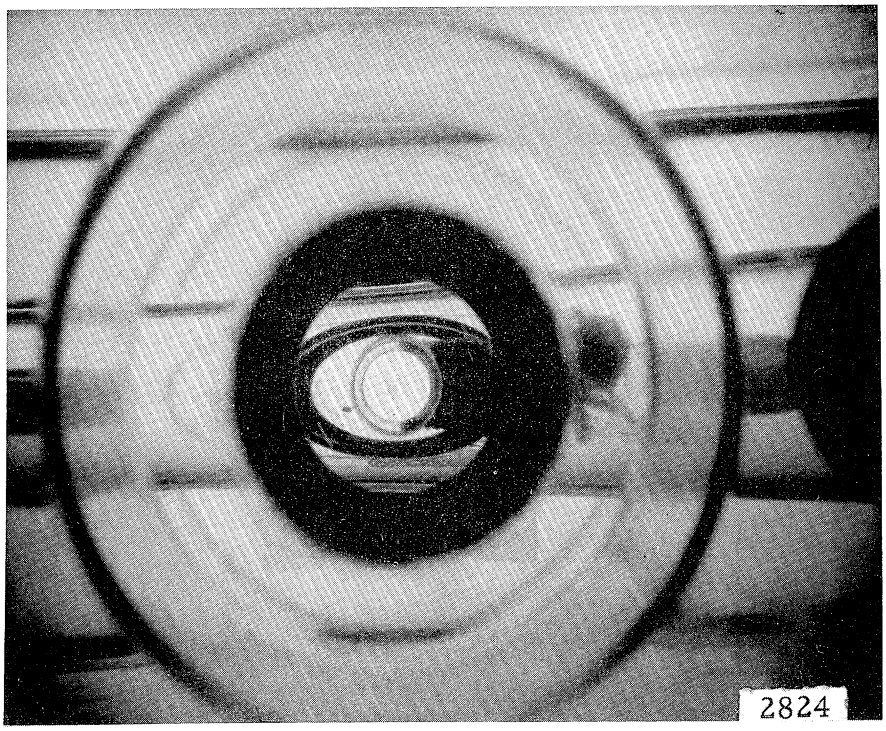

Fig. 24. Cavitation Cloud Surrounding Tubular Pin Specimen

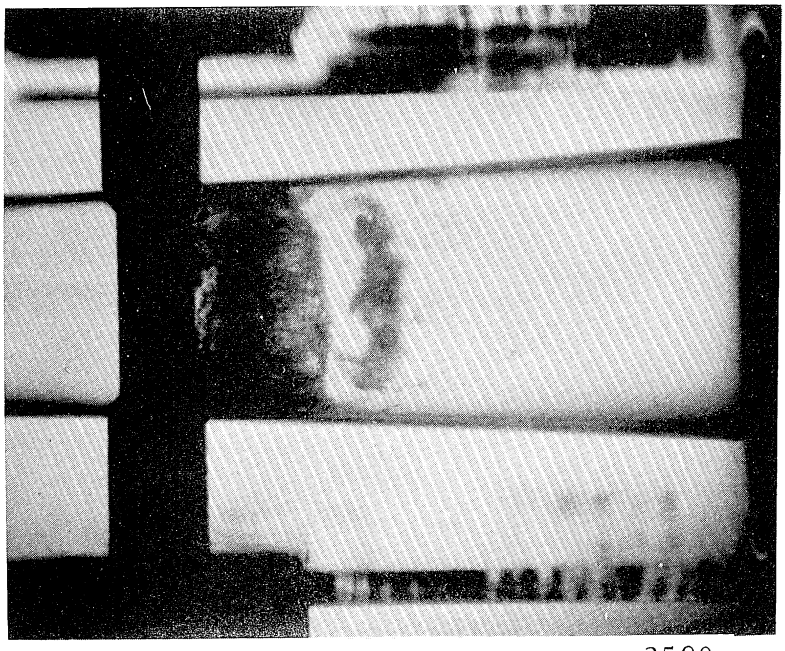

Fig. 25. Cavitation Cloud Shedding from Tubular Pin Specimen

velocity of 50 ft. per sec. After being subjected to cavitation attack for 15 minutes the specimens were removed and examined with a Bausch and Lombe metallographic camera. Distinct areas of damage were found along the sides and downstream portion of the cylindrical test specimens. This was limited, however, to a number of distinct circular pits or holes. Fig. 26 shows the effect of the increasing thickness of the cadmium film. The thinner plating (Fig. 26, A and B) allows complete removal of material from the surface at the center of attack. As the plating thickness is increased, (Fig. 26, C) the damage does not appear to extend through the coating, but rather only scars the surface.

Fig. 26-B shows a raised rim around a circular damage area. Picture C on the other hand shows areas where material has been dislodged. Close examination of the pits in C show a small circular area (indicated by arrow) near the center of the larger area which suggests that the material was removed by a sharp centralized blow much as would be present if the surface was impacted by a jet of fluid.

Fig. 27 contains three pictures showing again pits in the thinner films. The central area of each pit is void of all plating material. This is surrounded by an outer area where only a minor portion of the film is removed.

Fig. 27-A is an enlargement of the most central pit in 26-A The pit has a diameter of 0.6 μm. The picture shows the complete symmetry of the hole which has been created in the cadmium plating. This symmetry seems to indicate that the material removal has been accomplished by a single (rather than multiple) impact.

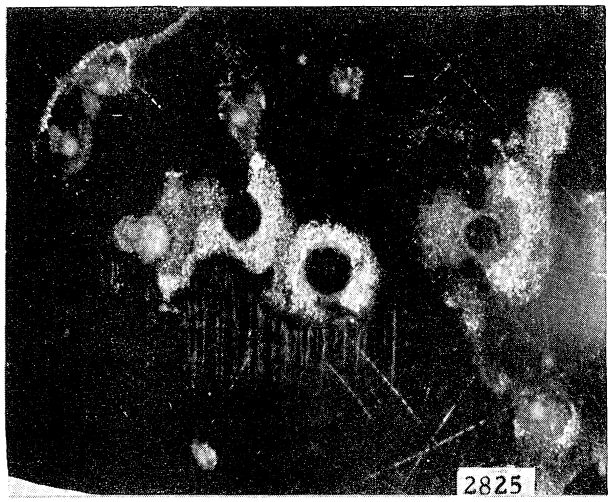

A

Coating Thickness: 2.5×10^{-5} in.

(120x)

B

Coating Thickness: 5×10^{-5} in.

Note raised rim.

(120x)

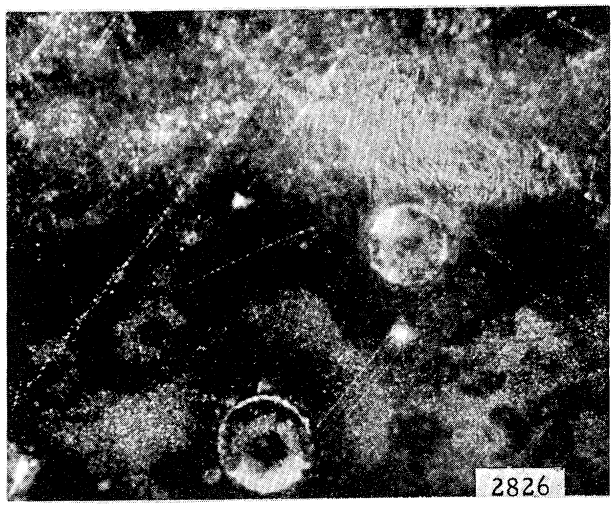

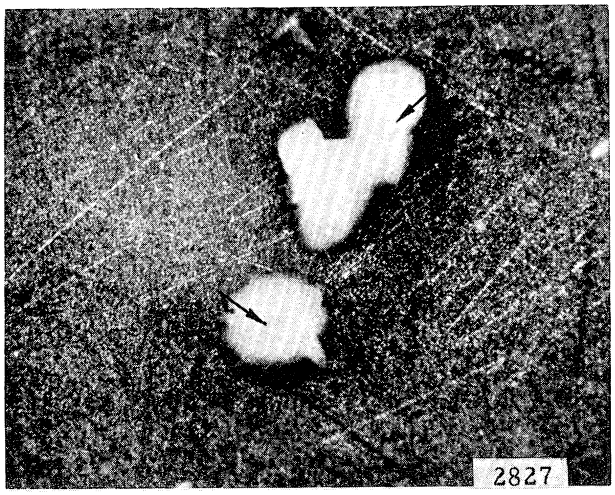

C

Coating Thickness: 5.5×10^{-4} in.

Small circles marked by arrows indicate a point of impact of a central jet.

(120x)

Fig. 26. Effect of Increasing Cadmium Coating Thickness of Stainless Steel Tubular Pin Specimens on Water Loop Cavitation Pits

A

Coating Thickness: 2.5×10^{-5} in.

Enlargement of the most central pit in Fig. 26-A.

(500x)

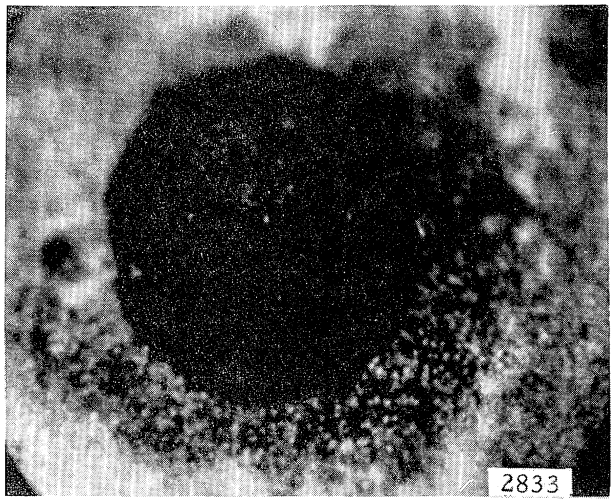

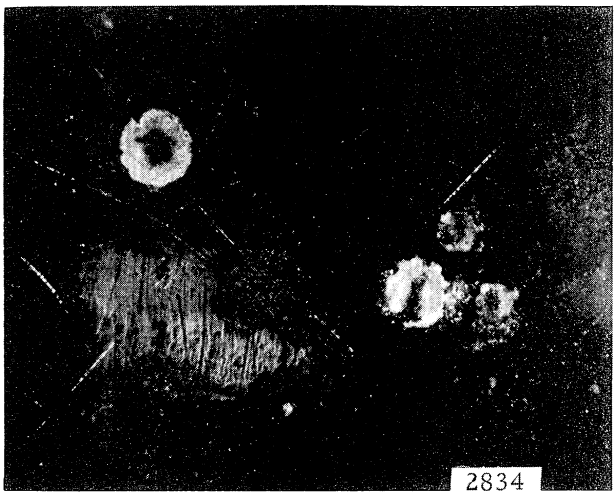

B

Coating Thickness: 5×10^{-5} in.

(120x)

C

Coating Thickness: 5×10^{-5} in.

Note difference in area around pits.

(120x)

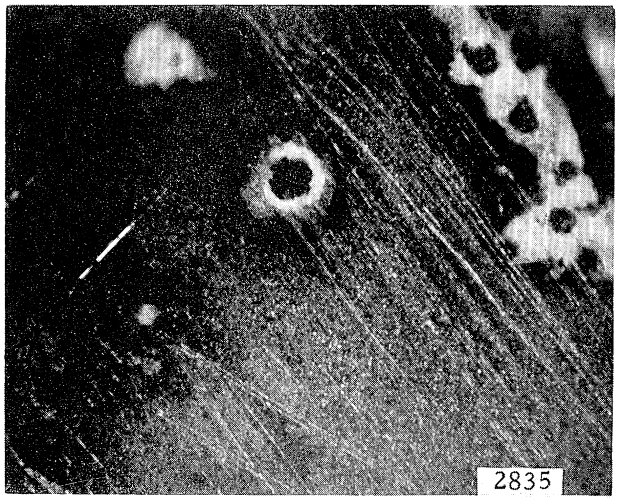

Fig. 27. Cavitation Pits in Coated Specimens Showing Material Removal

These pictures lend further evidence to the theory that cavitation damage is a result of microjets generated during bubble collapse rather than spherical shock waves as originally postulated by Rayleigh. The type of damage shown here cannot easily be attributed to a shock wave which would merely press the cadmium plate into the surface*, but is much more easily understood as the result of the stress produced by the radial flow of a high velocity liquid jet. Selected pictures of the sequence shown here in Fig. 26 and 27 have been published previously from this laboratory (14) in support of this theory.

3.) Pin Pressure Profiles

To correlate the area of damage with the pressure distribution, a pressure-measuring adapter was made for the plexiglas venturi (Fig. 28). This consists of two end pieces drilled to accomodate a 0.200-inch O.D. tube, silver-soldered to close off one end. The opposite end was connected to a Heise gauge. The rod was fitted with an 0.020-inch dia. hole, positioned 2 inches from its sealed end. This small hole served as a pressure tap. The end adapters were contoured so that the entire system closely duplicated the shape of the cylindrical specimens used in the tension-compression test. The tube was connected to a dial micrometer and a fitting which could be moved radially to sample pressures across the test area of the venturi. The top plate of the adapter was scaled off in degrees in order to mark the rotation angle of the impact hole to any point around a 360°

* This was verified by impacting small steel balls against a similar surface from an air gun.

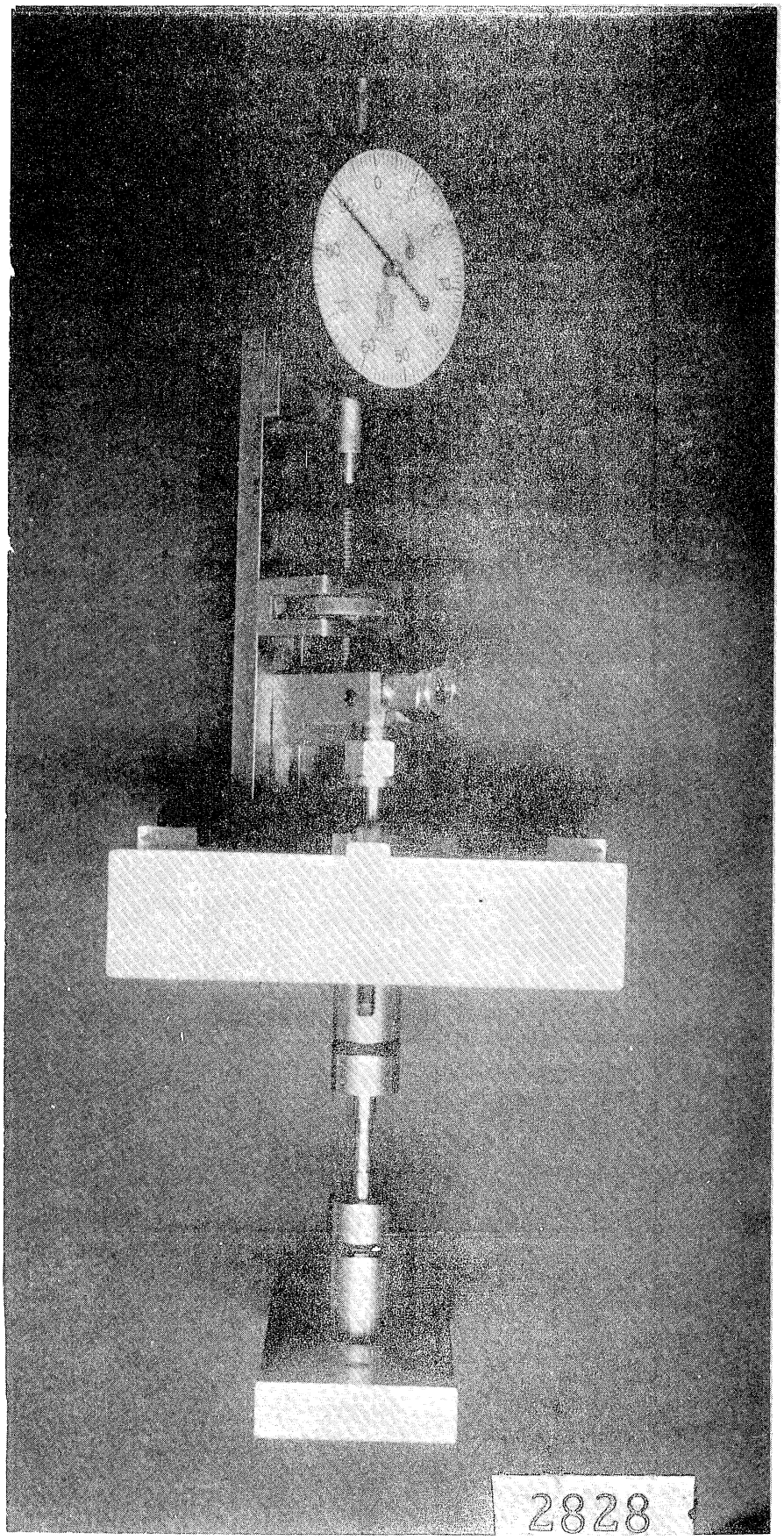

Fig. 28. Pressure Profile Adaptor for Plexiglass Venturi

arc. Numerous pressure profiles were taken at various pressure drops across the test section. Figure 29 shows a series of pressure profiles around a 180^{o} arc of the pin. The region of lowest pressure is at an angle of approximately 80^{o}. This result is a consequence of the design of the venturi and the chosen test position, and corresponds to the position of minimum flow area. Fig. 29 shows data for a venturi throat velocity of 50 fps. As the downstream pressure is reduced the visible cavitation field increases. At an absolute downstream pressure of one atmosphere the intermittant cloud became continuously visible. As the downstream pressure was further decreased the cloud extended further and further in the direction of flow.

Fig. 30 indicated the relative pressure profiles around the pin as the extent of the cavitation cloud is varied by a decrease in the downstream pressure at a throat velocity of 60 fps. These profiles are also plotted in Fig. 31 along with the same cloud lengths at 50 fps. throat velocity. These profiles indicate that the lowest pressures remain approximately the same for each field length, regardless of the flow velocity.

A sequence of profiles was taken across the test area to determine the effect of vertical displacement from the center of venturi. No systematic variation was found. Data points taken 0.1, 0.2, and 0.25 inches from the wall are shown in Fig. 32.

An attempt was made to measure pressure pulses which emanated from the test area using a Kistler quartz pressure transducer. The transducer was connected in a tee arrangement to the venturi inlet pipe. The transducer face was placed upstream of the venturi inlet and at 90^{o} to the standard pressure tap. No signals were apparent in the charge amplifier, indicating thereby that the highly transient cavitation pulses were attenuated substantially by the long pressure tube. These particular evaluations were not

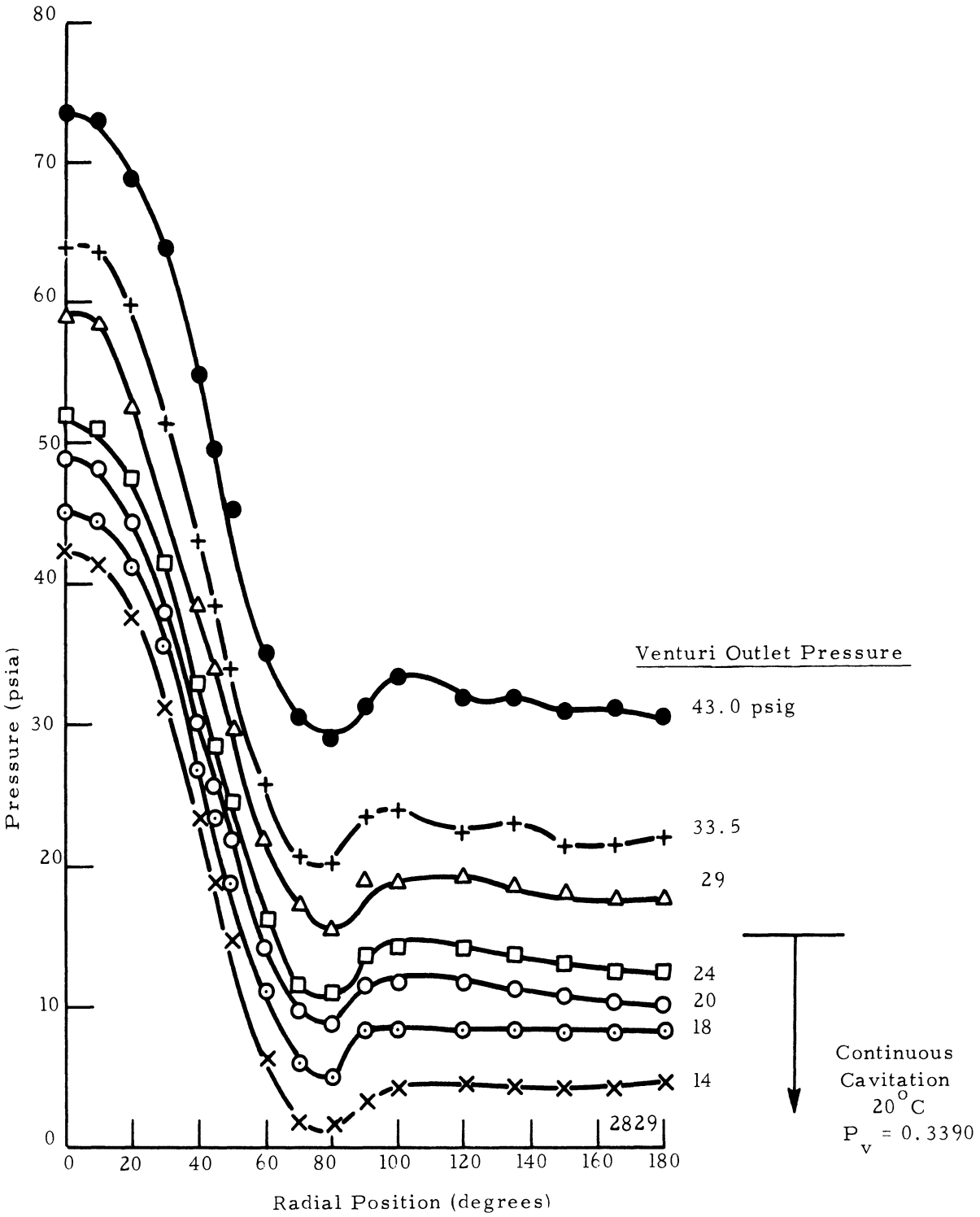

Fig. 29. Pressure Profiles Around Pin as a Function of Venturi Outlet Pressure in Water at 50 fps

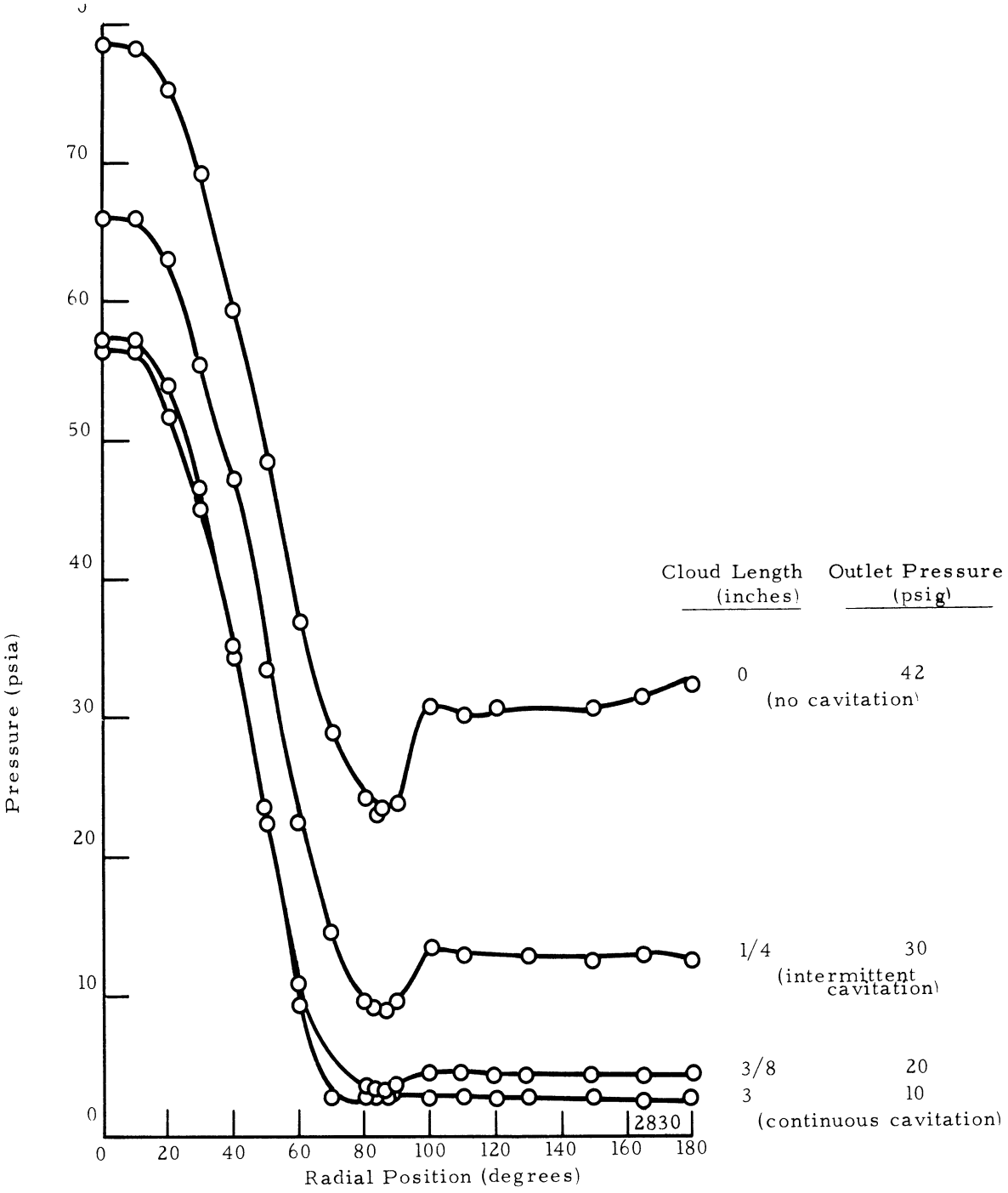

Fig. 30. Pressure Profiles Around Pin as a Function of Cavitation Cloud Length in Water at 60 fps

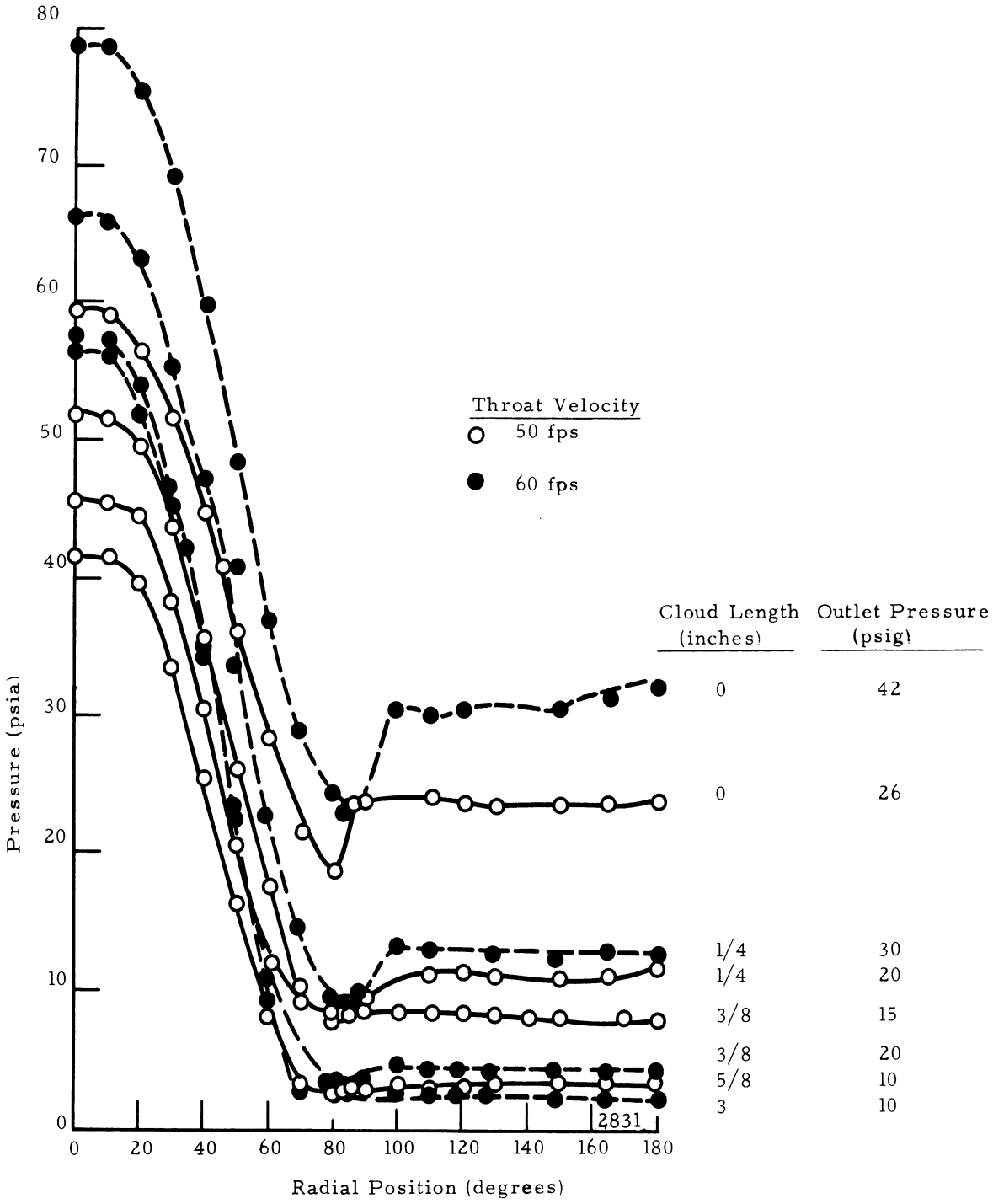

Fig. 31. Pressure Profiles Around Pin as a Function of Cavitation Cloud Length in Water at 50 fps.

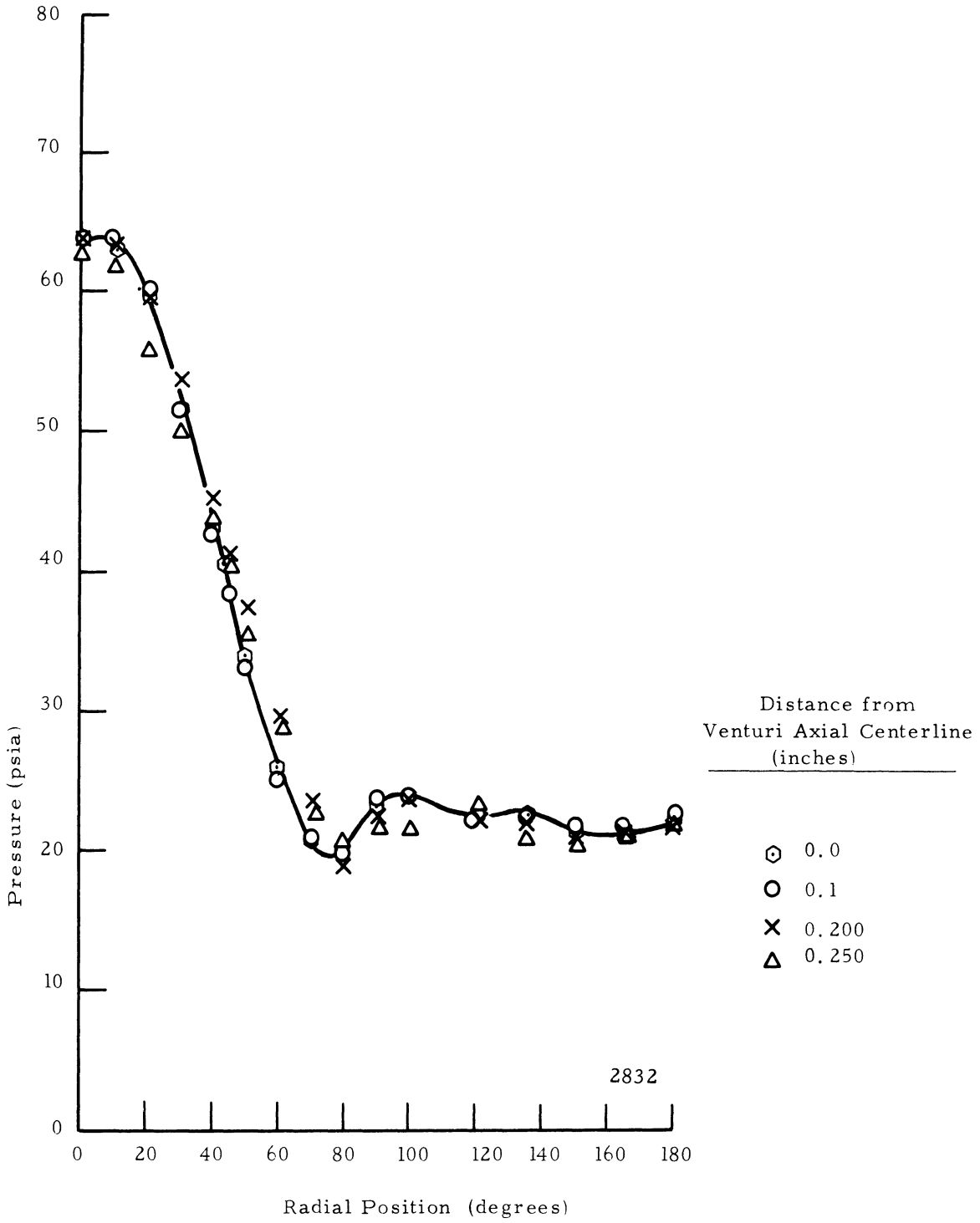

Fig. 32. Pressure Profiles Around Pin as a Function of Axial Displacement Along Pin in Water at 50 fps.

carried further since this type of work was also being pursued elsewhere in the laboratory.

C. Reproducibility

As was already mentioned the first investigation of venturi pressure drop versus damage in the mercury loop showed a peak in the damage rate at a pressure drop slightly larger than that corresponding to "sonic initiation", and damage decreased markedly as venturi pressure drop was further increased for the same throat velocity. The next samples run under identical conditions of velocity and pressure drop always had a weight loss markedly less than that which had occurred previously. Since the damage area of the specimen covered only 5-10% of its total area, weight changes were relatively very small. It was felt that perhaps foreign matter was being deposited in the damage area, causing only small weight losses and at times weight gains. Close investigation of the damage area did reveal some foreign matter present. The foreign substance was brownish-red in color, inorganic, and resembled closely ordinary rust. It was also observed that as the samples were tested during the day the weight loss rate for a given cavitation condition decreased. This observation would indicate that whatever was causing the problem was being entrained in the mercury as the loop was operated. The loop was subsequently thoroughly cleaned, reassembled, and filled with filtered mercury. A small amount of less pure mercury was also added as previously to compensate for losses. Whether or not the small additions of this secondary mercury source were important is not known.

Tests were again initiated with similar results, i.e., the damage rate decreased substantially for apparently identical runs as the loop was operated, again suggesting some important change in mercury condition during loop operation. To eliminate the possibility of residual mercury being held in some of the larger pits, the temperature at which the specimens were "distilled" under vacuum was increased from 500°F to 675°F and the distillation time increased from 2 to 3.75 hours. There was no apparent improvement in the results.

To evaluate damage reproducibility a series of ten tests were run at as closely as possible the same conditions of velocity, upstream and downstream pressure and temperature and time. The results showed damage rate variation up to 10 times the lowest weight loss rate found. It was then apparent that the reproducibility of damage was very questionable in this facility with the desired test arrangement so that some alternate methods for achieving the desired results were necessary.

D. Discussion of Experimental Alternatives

The primary desire was to increase the amount of damage to allow more precise measurement as well as its reproducibility. Two alternate methods were considered.

1. Double Pin

One method considered was that of placing a second pin specimen in a position such that the upstream pin could trigger a cavitation cloud which could in turn be adjusted to collapse on the forward portion of a second pin which would represent the actual damage specimen. In this manner the area of damage could be increased substantially. This method, however, presents serious problems. For one, damage to the trigger pin would

cause variation in flow patterns and in the cavitation cloud, which might then vary as the test progressed adding another unknown to the test. The opacity of the mercury would prevent the visual setting of the cavitation condition thus adversely affecting the reproducibility of the results.

Another problem would be the optimum positioning of the second pin. To maximize the damage, a number of positions would have to be tried. This would require a time-consuming cut and try procedure. Important variations in the flow pattern corresponding to pin position might be encountered. These two objections appeared over-riding so that this alternative was dropped.

2. Vibratory Facility

Despite the emphasis on the use of a flowing system in this work, the possible use of the vibratory facility was next considered, since it would provide a rapid test of stressed specimens if a suitable method of applying the stress could be achieved.

One advantage of using this facility is that the choice of test materials and test fluids are not so limited as in the mercury loop. (i.e. copper, brass and other materials of this type are not compatible with mercury). Also, previous tests with the vibratory facility indicated that the data obtained can be made highly reproducible (8).

This alternative could be easily followed since, in conjunction with the work in the mercury and water loops, an experimental damage study concerning non-machineable materials was being conducted in this laboratory, wherein the specimen is maintained stationary in the cavitation cloud. For this study,

an external modification of the existing vibratory facility was made. Early experimental results of this study were reported by Brager et al. (4). The existing equipment was modified by the addition of a plexiglas specimen holder suspended by three stainless steel rods. This early modification of the apparatus (Fig. 33 and 34) allowed an evaluation of the method and procedure. The test equipment dubbed the "Close Proximity Test" apparatus was refined by addition of stainless steel holders, micrometer posts for spacing adjustment, and a locking lower screw holder to position the specimen material to be tested. The entire set-up is shown in Fig. 35.

E. Experimental Study Using Shrink-Fit Specimens

1. Design and Fabrication

a. Specimen Concept and Description

One method of producing the required compressive stresses in the sample material for use in the vibratory facility is to hold the specimen by a shrink fit in an external rim, much like the assembly of hard steel rims on railroad wheels. This method has the advantage of producing a radially symmetric compressive stress field in the specimen matching the radial symmetry produced by the circular horn tip. Calculations indicated that this method of testing would be feasible. The test specimen consisted of a solid cylindrical center section made up of the test material, surrounded by a steel outer ring. The steel outer ring was made such that, δ, the radial difference in mating diameters would cause circumferentially uniform compressive loading of the test specimen when the steel outer ring was shrunk onto the center section.

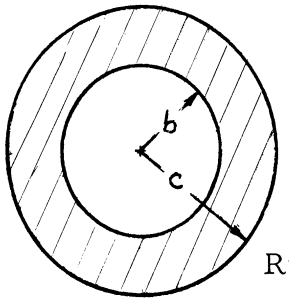

Ring

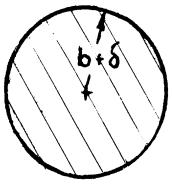

Test Specimen

The relationship between the compressive force p_{sf} and fit, δ. (15)

$$\frac{\delta}{b} = P_{sf}\left\{\frac{1}{E_o}\left[\frac{1+(b/c)^2}{1-(b/c)^2}+\nu_o\right]+\left[\frac{1-\nu_i}{E_i}\right]\right\}$$

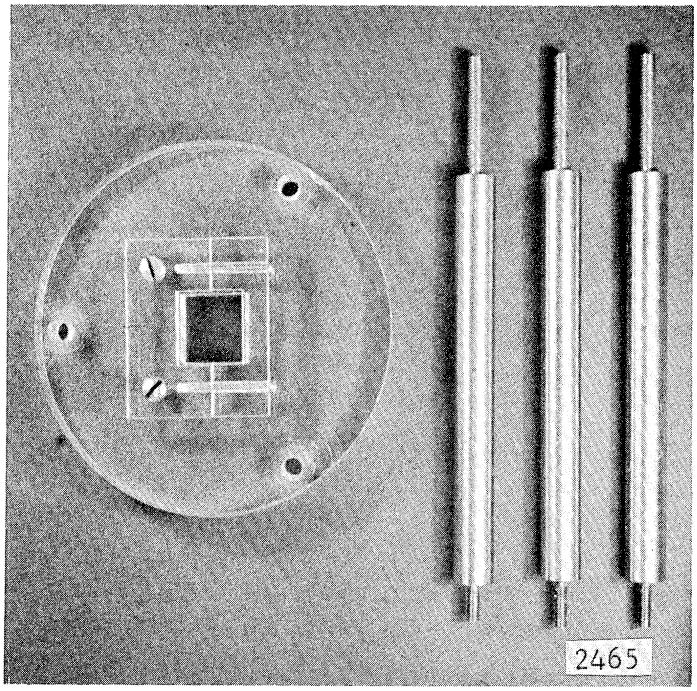

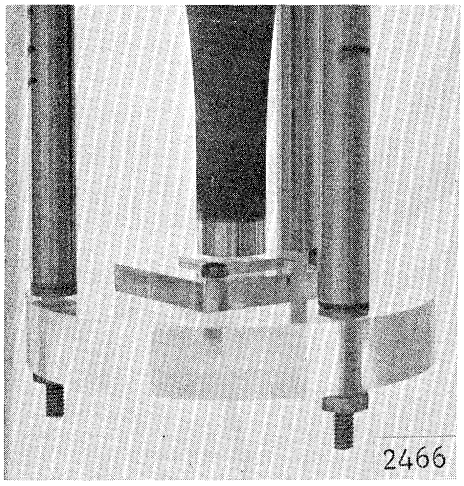

Fig. 33. Photographs of Early Close Proximity Specimen Holders and Supports

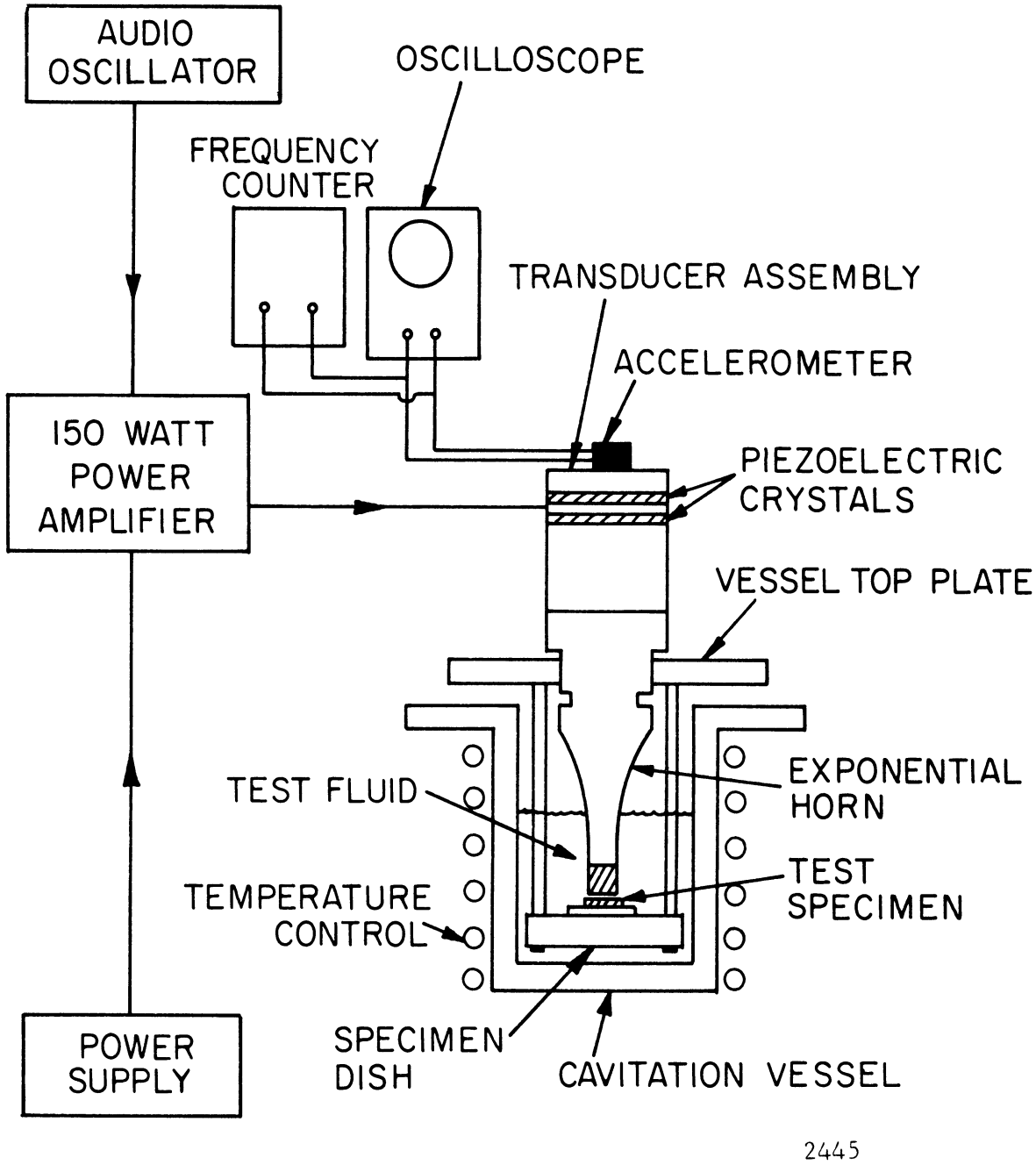

Fig. 34. Schematic Representation of the Stationary Specimen Vibratory Cavitation Test Facility

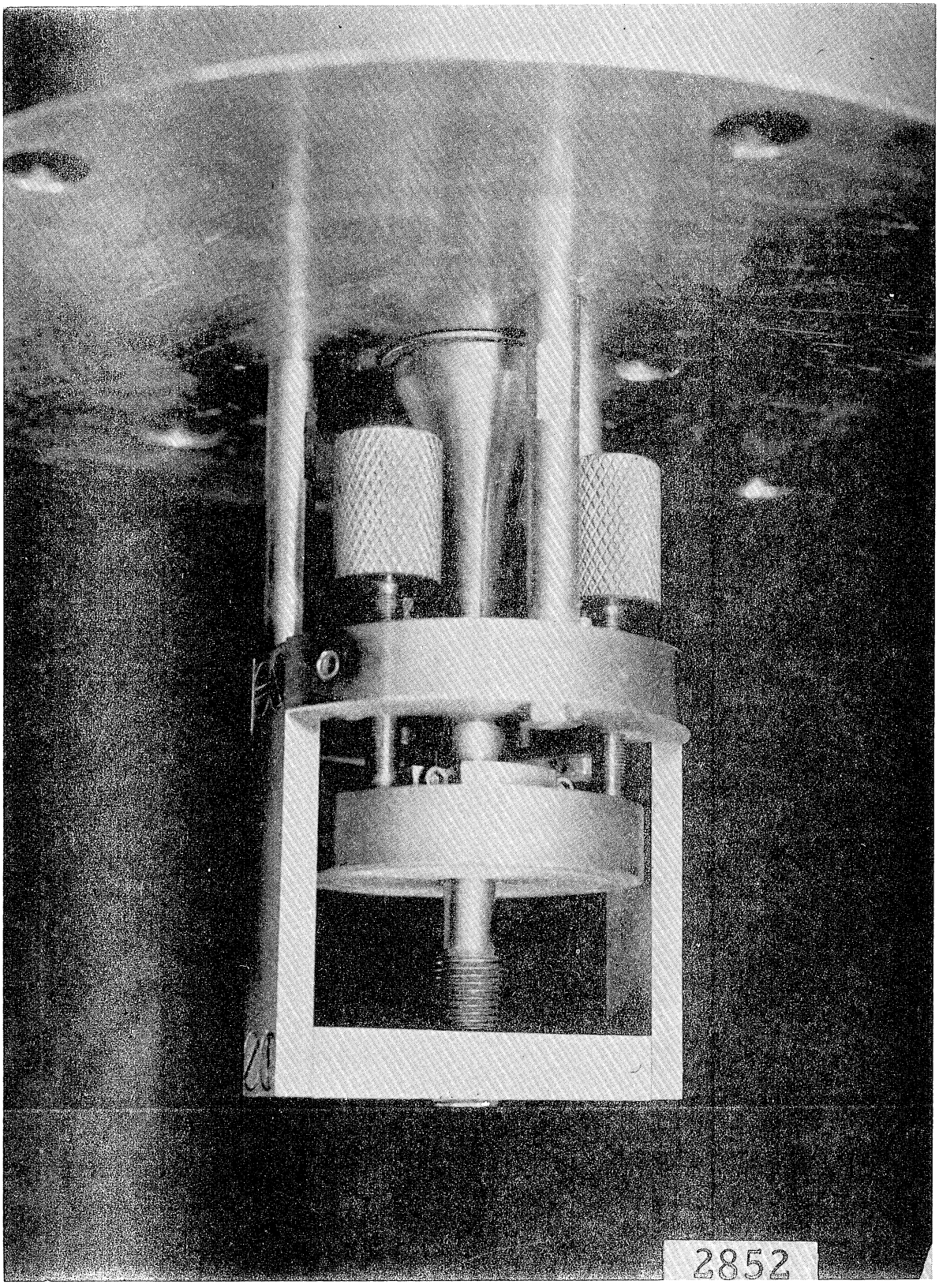

Fig. 35. Photograph of Adjustable Close Proximity Apparatus

where E = Elastic modulus

ν_o = Poisson's ration for outer ring

ν_I = Poisson's ration for inner material

$b + \delta$ = specimen radius

δ = shrink allowance

σ_θ = hoop stress in outer ring (limit for 304SS = 34,000lbf/in^2 corresponding to yield stress)

c = outside radius of outer ring

P_{sf} = compressive force

An additional item which must be considered here is whether or not such a shrink fit would cause a hoop stress, σ_θ, in the outer steel ring larger than the yield stress of the steel. The value of σ_θ for a particular P_{sf} can be found considering only the ratio of the radii:

$$\sigma_\theta = \left\{ \frac{1 + (b/c)^2}{1 - (b/c)^2} \right\} P_{sf}$$

Feasibility calculations of the relative magnitude of the forces involved were made for a number of specimen materials and sizes in steel rims. The following table shows some of the results of the investigation.

TABLE I

Calculated Stresses for Shrink Fit Specimens

Sample Material	b(inches)	c(inches)	δ (inches)	Specimen P_{sf} lb$_f$/in^2	Rim σ_θ lb$_f$/in^2
steel	9/16	1 1/8	.001	18,000	30,000
steel	3/8	15/16	.00076	22,800	31,600
copper	9/16	1 1/8	.00114	18,000	30,000
copper	3/8	15/16	.00084	22,800	21,600
aluminum	9/16	1 1/8	.0014	18,000	30,000
aluminum	3/8	15/16	.00112	22,800	31,600

The above table indicates the range of δ for three different materials, at two different test specimen diameters. From the calculated data it was apparent that this type of specimen preparation and testing was feasible. Due to the availability of equipment and the relative simplicity of the test specimen a test program along these lines was initiated.

b. Specimen Fabrication

In order to form the shrink fit, the test disc was submerged in liquid mitrogen (77.4^{o}K), while the steel ring was heated on a hot plate to $\sim$700^{o}F. The test disc was then quickly placed inside the steel disc and the combined ring-specimen was quickly cooled to slightly above room temperature. Extreme care was required to properly align the two pieces. Calculated compressive stresses for the initial tests were up to $\sim$18,000 lb/in^{2}.

The ring material was 304SS (nominal O.D. = 1.250 inches, I.D. = 0.7500 $\pm$ .0005). The plate thickness was nominally 1/4 in., since possible bending might be encountered for thinner plates on assembly. The test material slugs were 0.25 inches thick, and the outer diameters were made to a tolerance of $\pm$ 0.00005. The specimen and ring combinations (Fig.36) were selectively paired after accurate measurement of the diameters. The pairs were selected according to difference of fit, δ, thus providing the desired surface stresses to the inner slugs.

c. The Test Facility

The close proximity appartus was modified to accept the circular shrink fit specimens using a 3 inch diameter plate with slots to accomodate three movable jaws which could be tightened on the periphery of the sample to hold it in position. Fig.37 shows the adapter itself, whereas, Fig.38 shows the manner in which the test specimen was held.

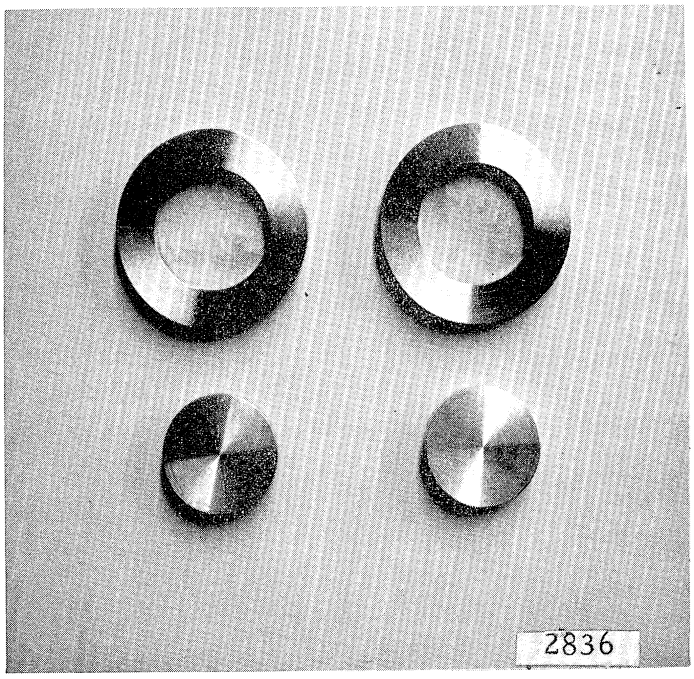

Fig. 36. Specimen-Ring Combinations for Shrink Fit Close Proximity Test

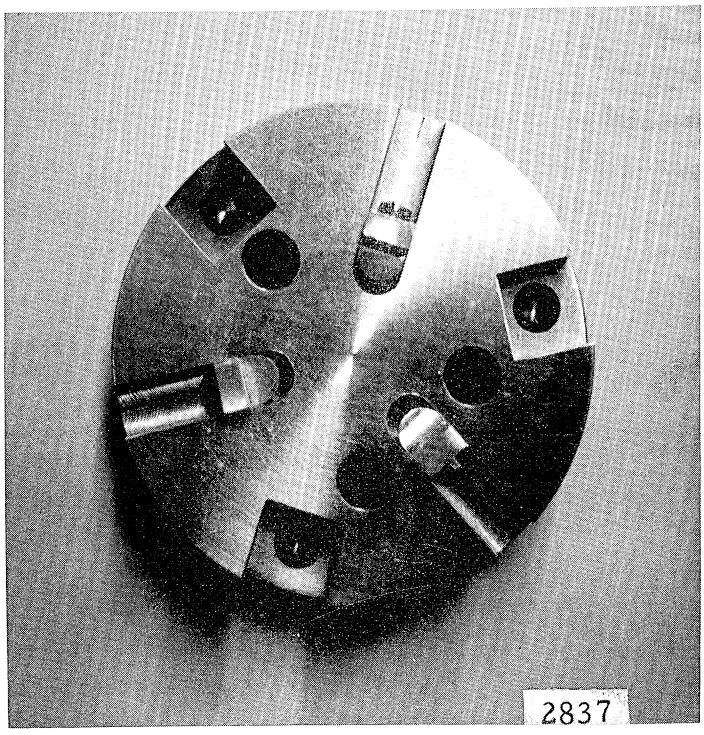

Fig. 37. Specimen Adapter Used in Close Proximity Test for Shrink Fit Specimens

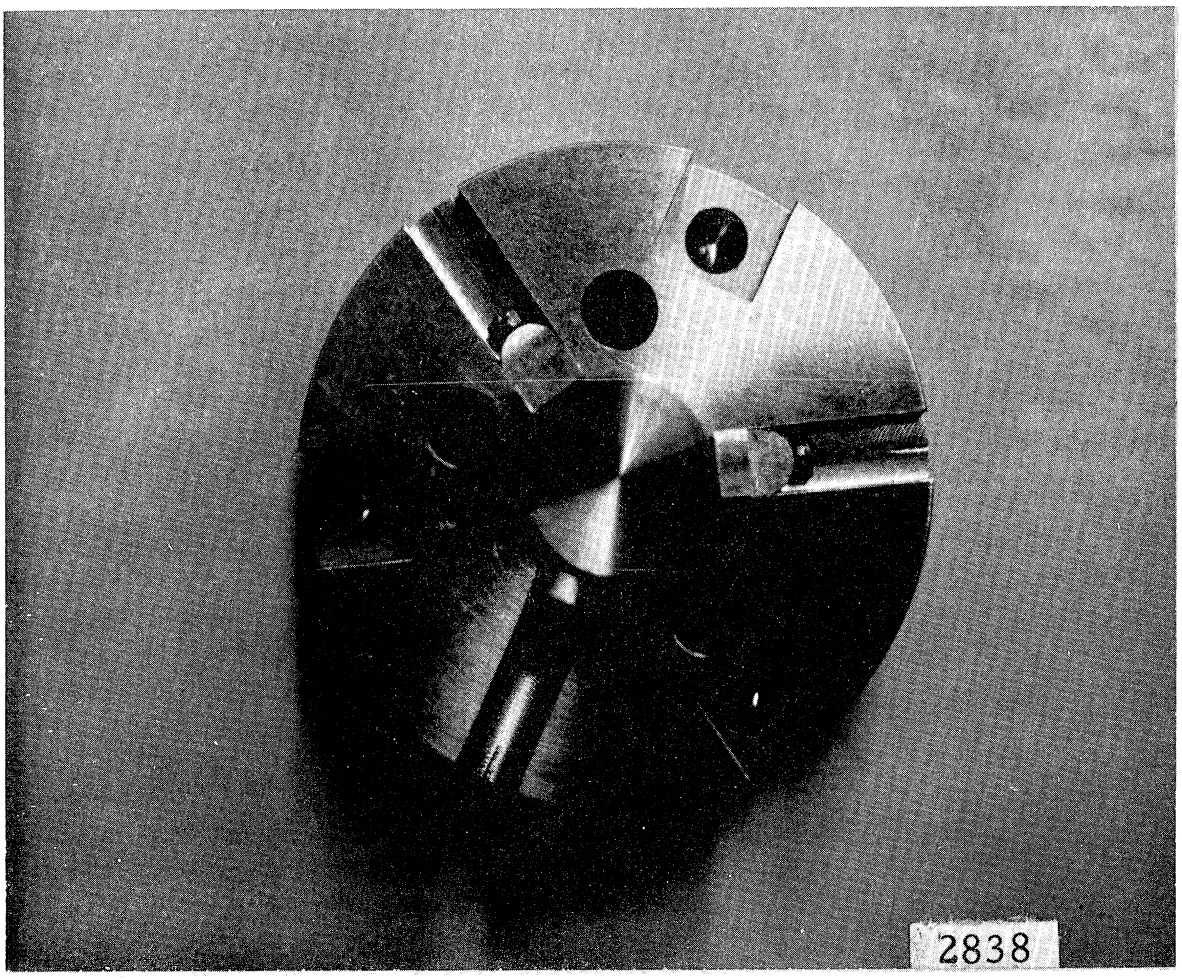

Fig. 38. Adapter with Slug Specimen in Place

After precision weighing the specimens were tightened into the holder. The holder was then positioned against the three micrometer thread lifts in the body of the test facility which were used to adjust both the vertical and horizontal position of the specimen. The distance between the horn tip and the specimen was set using a feeler gage. After the micrometer lifts had been set such that the specimen was at the correct distance from the horn tip, the holding screw in the bottom center of the apparatus was tightened. The initial tests were conducted at a spacing of 0.018 inches corresponding to the maximum damage clearance found in earlier tests (4).

Previous data reported from this laboratory (8) and elesewhere (20) indicated that the damage rate in water maximized at a temperature of approximately 120^{o}F. This temperature was chosen as the test temperature for the initial trials.

2. Test Results - Shrink Fit Specimens

a. Materials Tested

As mentioned previously, a broad selection of materials with the vibratory facility was possible. It was therefore necessary to consider the large number of possibilities and delineate the advantages and disadvantages of each. It was important that the materials be generally available and easily fabricated into the desired shape and size. Hence, O.F.H.C. (oxygen free high conductivity) copper and 2024 aluminum were chosen. An added advantage of these materials was their low cavitation damage resistance. Thus damage could be attained relatively quickly, allowing a rapid evaluation of the test method.

b. Results of the Vibratory Tests

The data obtained in this investigation are plotted in Fig. 39 as cumulative damage vs. time. It shows that the effect of the radially-symmetric compressive stress on both OFHC copper and 2024 aluminum is to decrease cavitation resistance. The damage

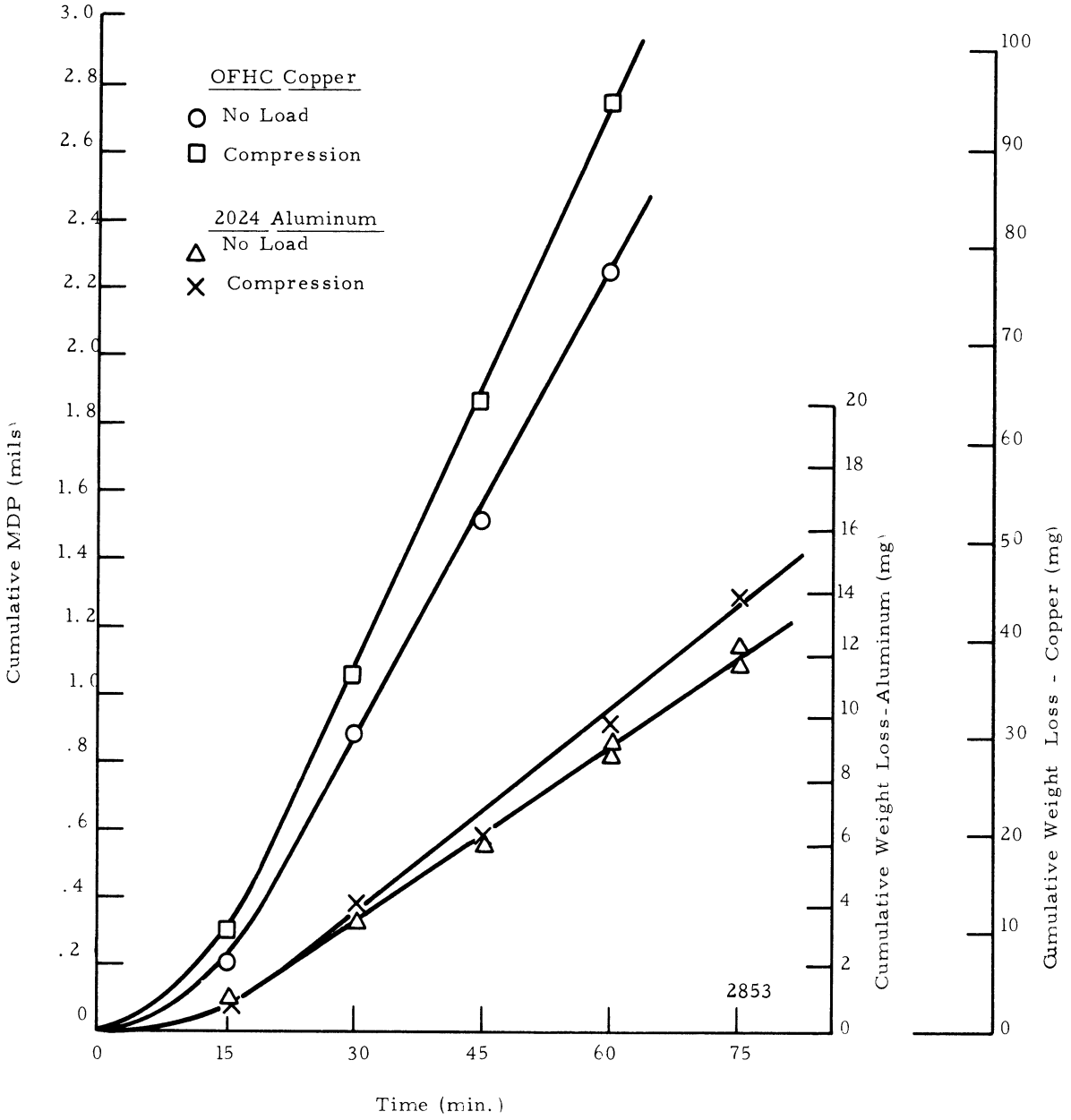

Fig. 39. Effect of Compressive Stress on Cumulative Damage of OFHC Copper and 2024 Aluminum Shrink Fit Specimens

rate for the stressed copper specimen is 114.3 mg/hr (1.91 mg/min) and that of the unstressed copper control specimen was 95.78 mg/hr (1.595 mg/min). The ratio of the two rates show a difference of 19.33%. i.e. the rate of damage when the copper specimen was under a compressive stress was 19.33% greater than when no stress was applied. Similar results were obtained for 2024 aluminum. The damage rate in the stressed condition was 11.70 mg/hr (0.195 mg/min) vs. 10.92 mg/hr (0.182 mg/min) for the unstressed condition. The ratio of the two rates however, is 7.14% for the aluminum. The copper damage rate was about 9x that of the aluminum.

A problem associated with this method of testing is that of determining precisely the actual stress distribution in the specimen, which is actually a complicated problem . Also, obviously, tensile stresses in the specimen cannot be generated in this manner. For these reasons a more versatile approach was required. The shrink-fit specimen method did, however, indicate that a substantial effect upon damage rate from the specimen stress condition did exist in some cases. Thus a further investigation was warranted.

F. The Vibratory Close Proximity Facility

1. Design and Fabrication

The equipment used for the subsequent tests which were conducted to determine the effects of tensile and compressive stresses, consisted to two coupled facilites. These were a.) the tensile-compression unit and b.) vibratory horn assembly. In order to provide a basis for explanation of the experiment, a short description of each of the above will ge given.

a. The Tensile Compression Unit

Fig. 40 shows the tensile-compression unit prior to assembly and after partial assembly. The facility consists of a Parker-Hannifin double-acting cylinder, model 2H-C. Its 4" diameter inner bore drives a 1 3/4" ram with a stroke of 2 inches. The cylinder is capable of operation up to an internal oil pressure of 3000 psi or a ram load of approximately 37,000 pounds. The ram end of the cylinder was fitted with a two-inch diameter adapter with a machined slot to accept the 1/4" thick test specimens designed for use in this experiment.

The mounting platform was manufactured from a 1 1/2" cold rolled steel plate necessary for adequate stiffness to prevent premature buckling of the specimens in the compressive mode. An initial design with a 3/4" aluminum plate was entirely inadequate. The stationary end of the test specimen holder was a dual block arrangement fitted with a tongue and groove perpendicular to the pulling direction. This particular design was chosen to enable future changes in the slotted specimen holder if desired without the need for costly replacement of the entire stationary end assembly. Figure 41 shows a close-up view of the assembled specimen mounting with a specimen in place between the test jaws. The longitudinal distance between jaw faces is 1.5 inches. The specimen is held in place by the two 1/2" socket head cap screws pictured.

Fig. 42 is a photograph of the total assembly of the machined parts shown in Fig. 41. The additional pieces are the solid horn-stabilizer and set up table which provides a flat steady surface as well as a reference for positioning the ultrasonic unit. The table top is capable of allowing the entire body of the exponential horn through a 2 1/4" dia. hole positioned just above the centerline of the test specimen. Three semi-spherical indentations were made in the table

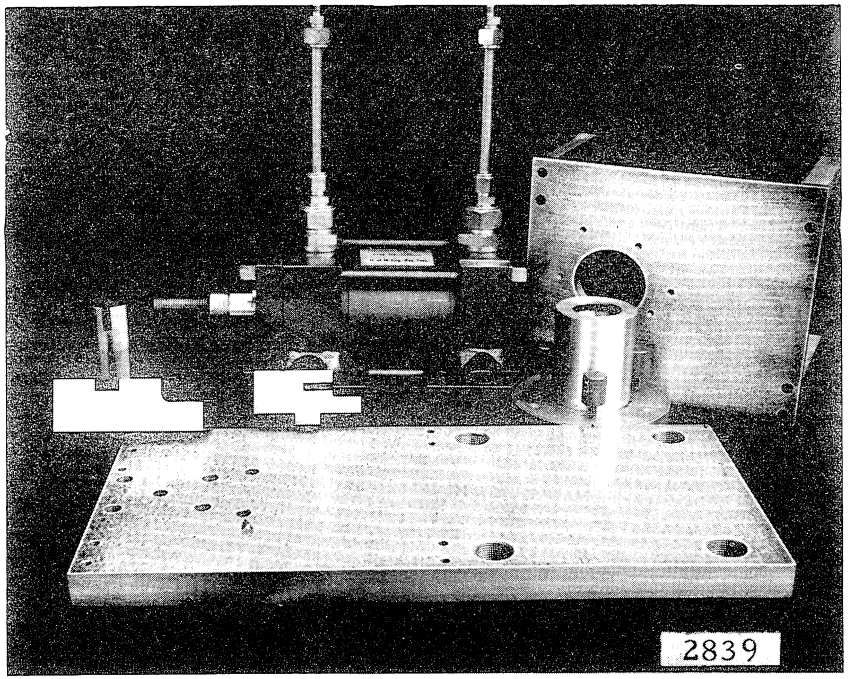

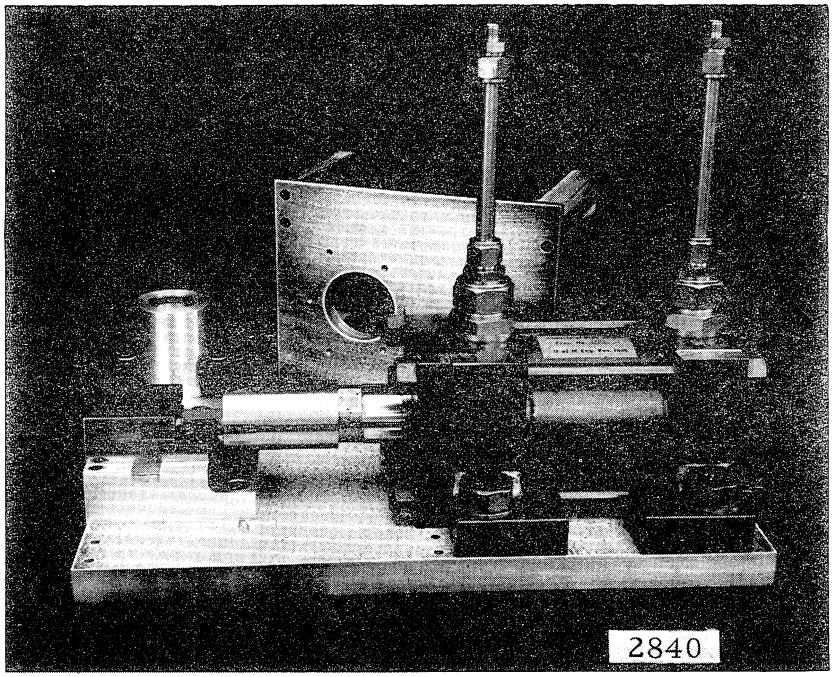

Fig. 40. Photographs of Tensile-Compression Unit in Partial Assembly

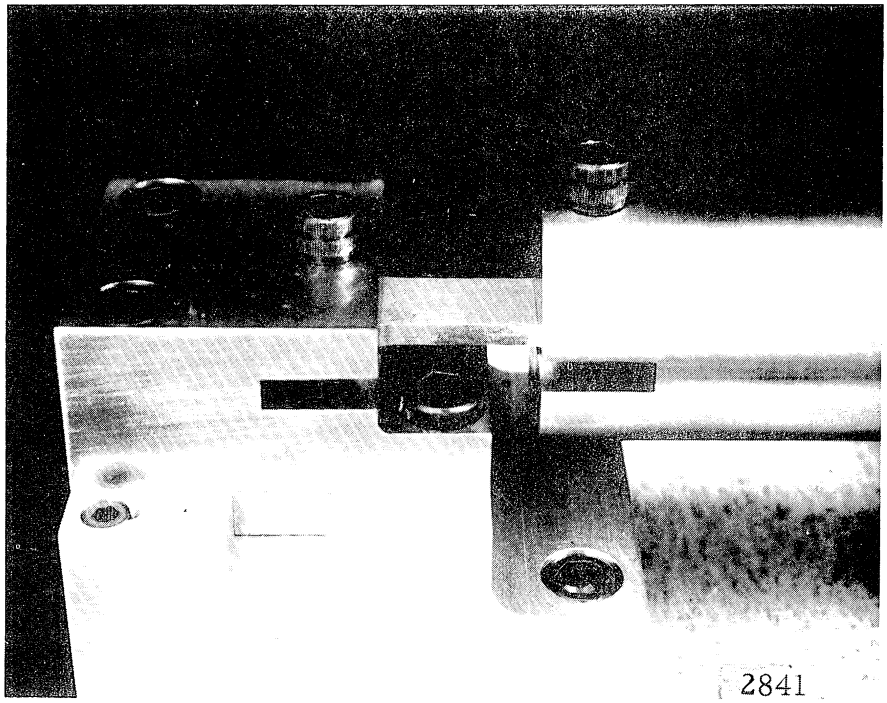

Fig. 41. Close-up View of Specimen Held in Position by Ram Adapter and Stationary Holder

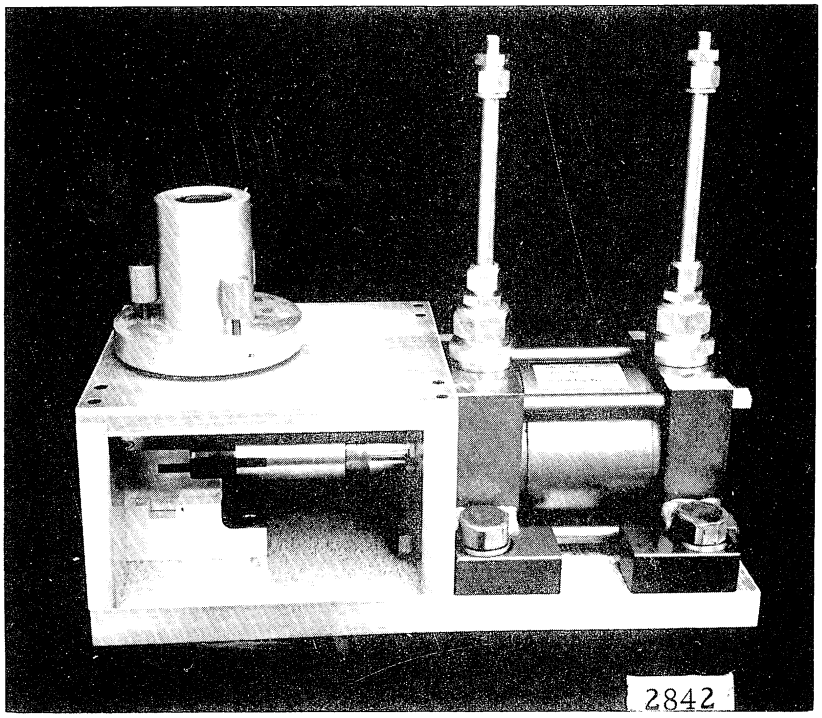

Fig. 42. Total Test Unit Assembly

top 120° apart to accept the semi-spherical ends of the micrometer legs which are set in the horn stabilizer unit.

In the table top are three tapped holes, also 120° apart, set midway between the spherical indentations. These three tapped holes provide for three 1/4-28 socket head cap screws which are used to secure the stabilizer unit to the table top during operations.

b. The Vibratory Unit Assembly

In order to couple the vibratory facility to the test unit it was necessary to have an appropriate holder or adapter unit. This consisted to two pieces solidly connected to form an assembly called the "horn stabilizer." The actual stabilizer unit was a hollow cylinder, 2 1/8" O.D, cut internally to accomodate the outside diameter of the horn (1.5 in.). To accomodate the vibratory facility the cylindrical tube was fitted just below its top with an internal O-ring. This O-ring was kept lightly greased so that it would allow free movement of the horn in the vertical direction but would be capable of suppressing all lateral movement of the horn assembly. Fig. 43 is a close-up view showing this stabilizer attached to its complementary part, a circular plate 5 1/4 inches in diameter.

The circular plate was cut to accept the stepped nodal flange of the exponential horn. This stepped hole allows for seating of the O-ring sealing the horn. The thickness of the circular plate was made such that it would serve as platform against which the snapring could be set as shown in Fig. 44.* This plate had three holes tapped with 1/4 - 40 micrometer threads which accomodated the three knurled micrometer screws. These were finished with semi-spherical tips. These micrometer lifts were used to adjust and establish the height of the horn assembly, thereby allowing the adjustment of the distance between the horn tip attachment and the damage specimen. The plate

*A patent has been obtained on this horn-sealing arrangement.

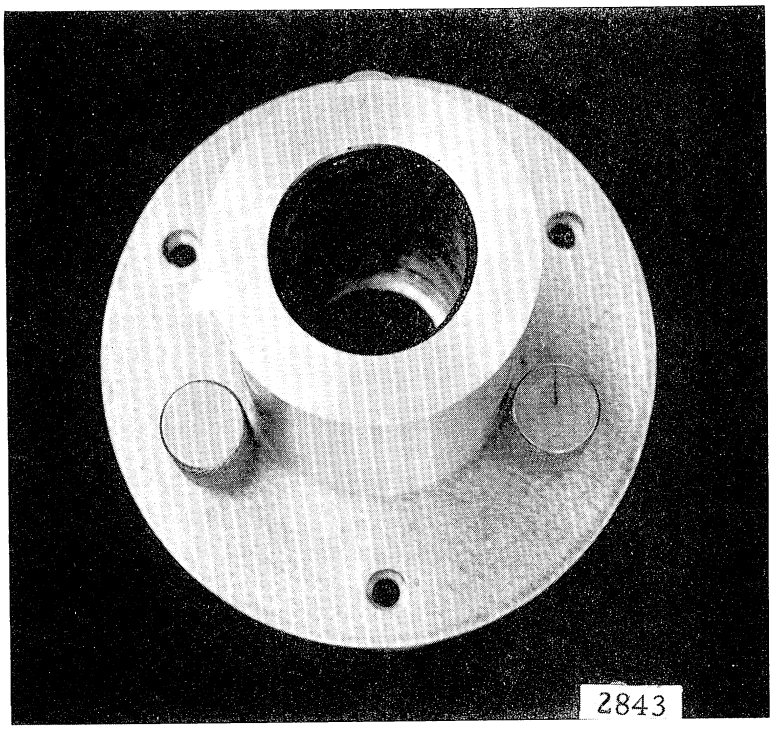

Fig. 43. Horn Stabilizer Unit on Adjustable Plate

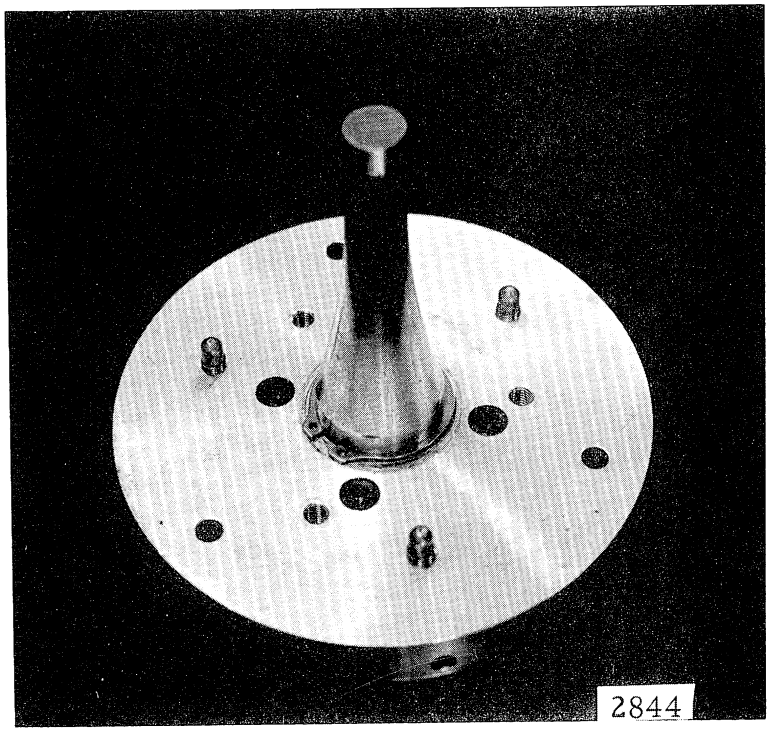

Fig. 44. Bottom of Adjustable Plate Showing Snap Ring Attachment

was also drilled and tapped on the edge at the same angular position as the 1/4-40 holes but at 90° to them to accomodate locking screws. These tapped holes were fitted with a 1/8 inch teflon plug which could be tightened against the micrometer lift to assure that no movement of these screws would take place while a damage test was being made.

To run a damage test the vibratory horn assembly (Fig. 45) was placed in the stabilizer and attached with the snap ring. The entire assembly was placed on the set-up table, and the three holding screws put in place. Proper adjustments were then made to perform the cavitation damage test.

c. The Horn Tip Attachments

The horn tip attachments shown in Fig. 46 were machined from 304SS stock. The button was a threaded specimen with a head length of 0.250 inches and a diameter of 0.5471 $\pm$ .0002 inches. The overall length of the attachment was 0.625 inches. The face of each of the specimens was ground to a surface roughness of approximately ten microinches. The outer diameter was made to a 20-30 microinch finish.

Fig. 47 indicates the position at which the replaceable horn tip is attached. The horn tip attachment is mounted in the exponential horn by use of a 1/4-28 NF threaded stub. The attachment is screwed into the end of the horn and tightened with a special adapter (Fig. 48) to a torque of 85 in-lb. The weight of horn tip attachments was maintained at 9.4 $\pm$ .10 grams, an optimum found (19) for the horn assembly.

d. Test Specimen Preparation

The test specimens were fabricated from plate stock (Fig. 49). The overall length of the specimen was 3 inches. The length of the cut-down central area subjected to the cavitation environment was 1.125 in. with a width of 0.630 in. The thickness was held to

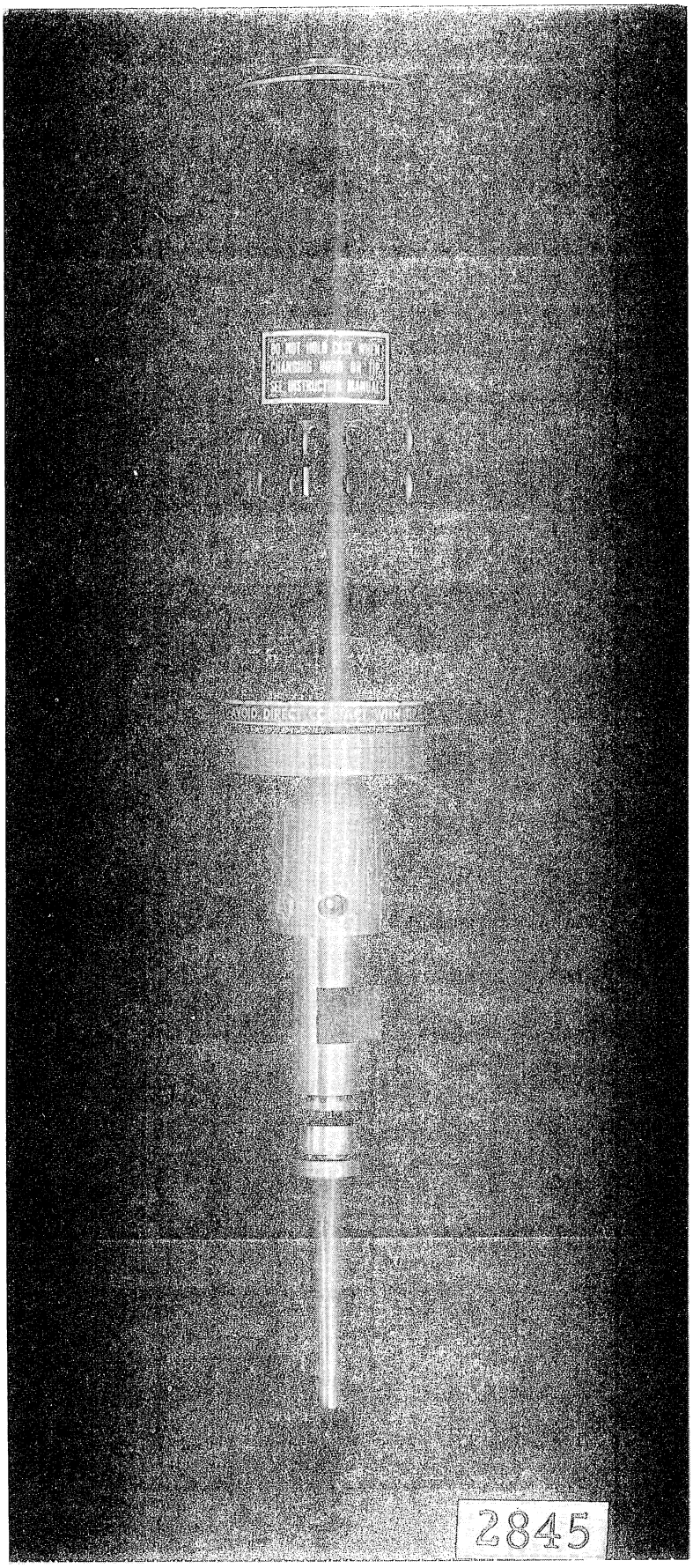

Fig. 45. Vibratory Horn Assembly

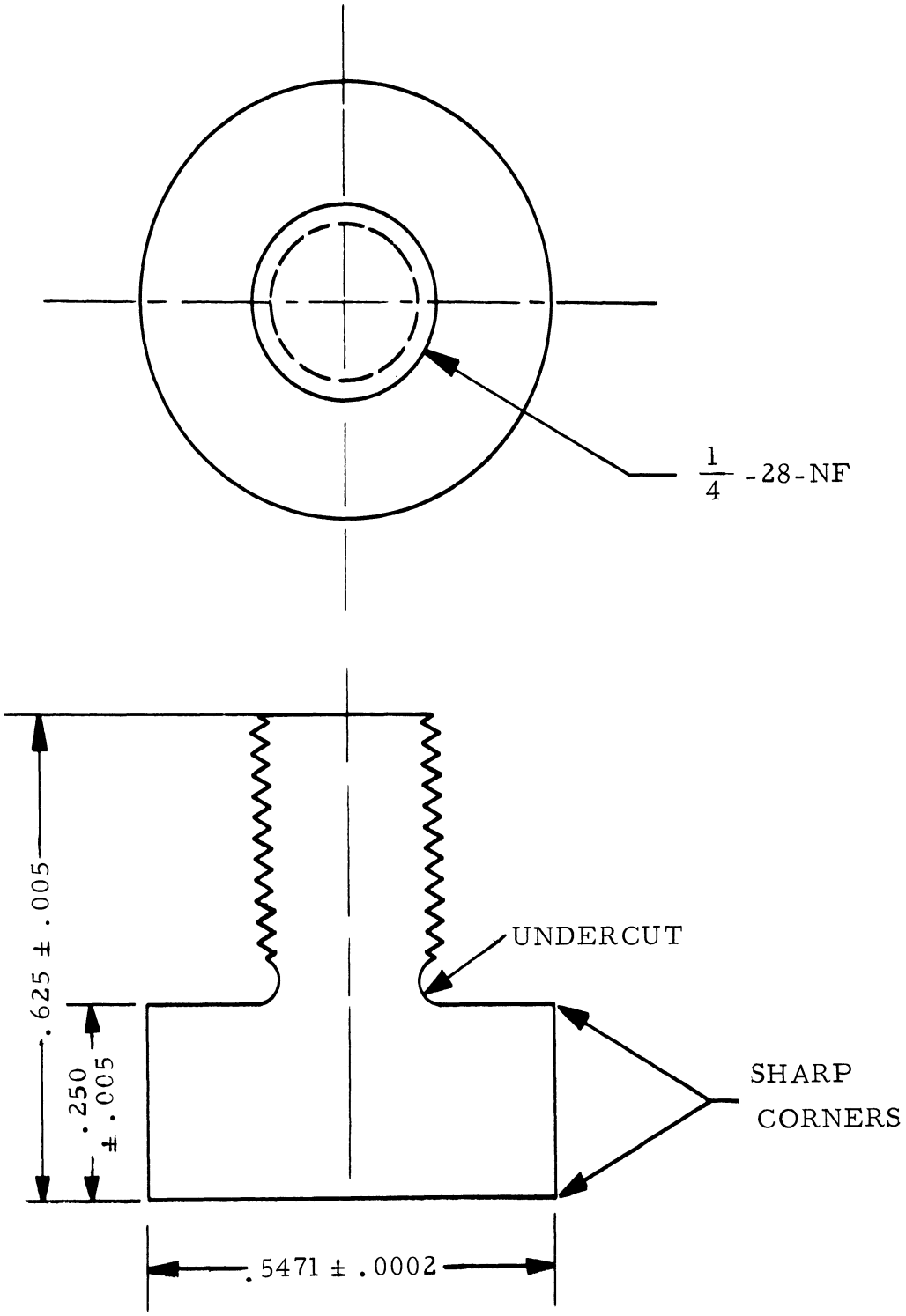

Fig. 46. Dimensional Drawing of Horn Tip Attachment

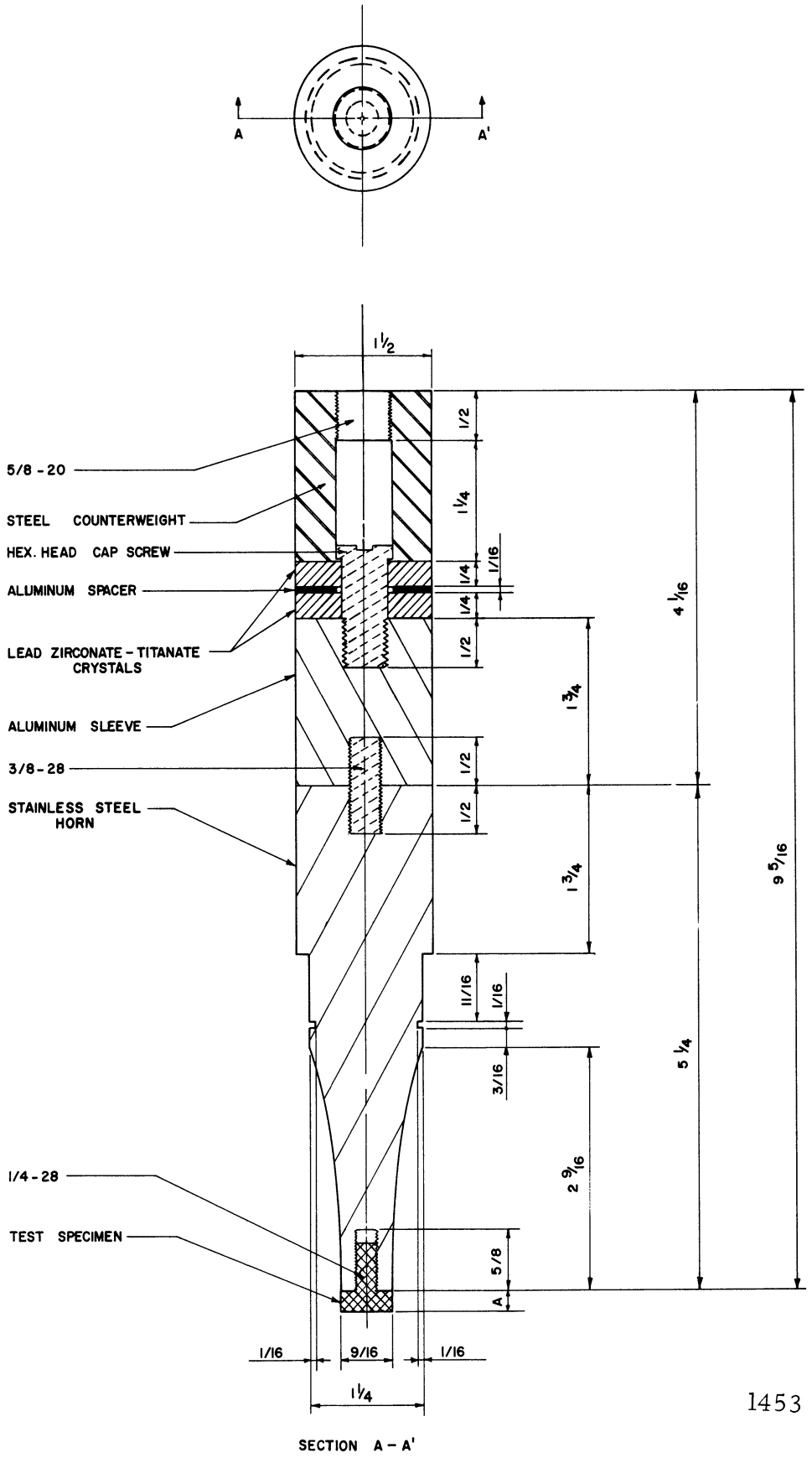

Fig. 47. Diagram of Vibratory Horn Showing Horn Tip Attachment in Place

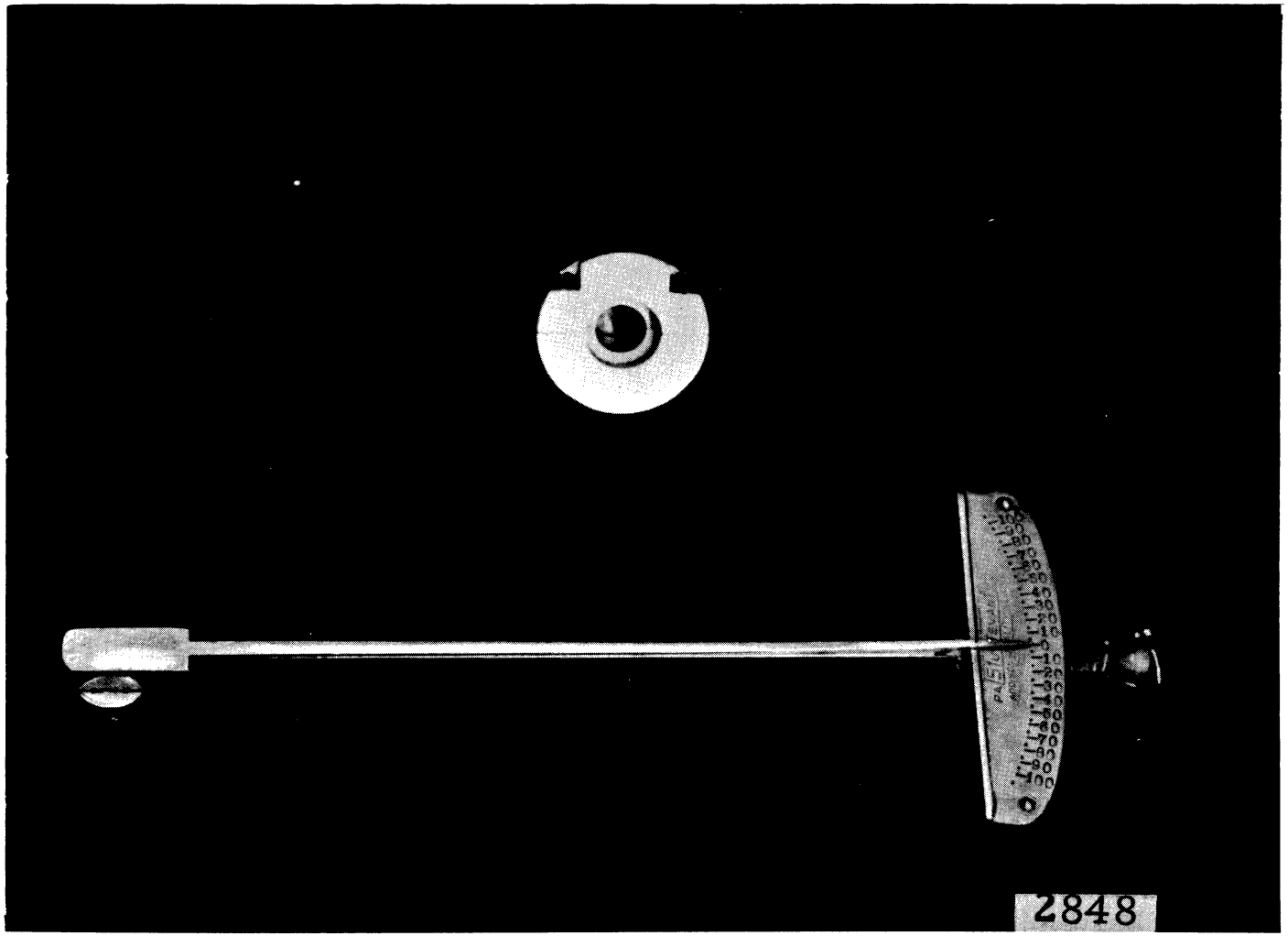

Fig. 48. Special Tip Placement Adapter with Torque Arm

approximately 0.150 in. After fabrication, the surface in the test area was finished with 600 grit paper to remove grinding marks which would possibly alter the fluid flow pattern on the surface. The test surface and the specimen ready for test are shown in Fig. 50.

Data Aquisition

The specimen is placed between the ram adapter and the rigid element and secured by two 1/2 " socket head capscrews (Fig. 51). The ultrasonic horn assembly is then placed on the table with the three micrometer screw bases set into the shallow wells in the top plate. The specimen is then stressed by the hydraulic ram as desired.

To set the specimen into compression or tension the valve to the volume ahead of or behind the ram plate is opened (Fig. 52). The valve to the oil return is opened to allow transfer from the front or back portion of the cylinder depending upon which mode is desired. Pressure is applied by the use of a Black and Decker Porta Power hand pump. The pressure is monitored to a pre-assigned level on a Teledyne 2301 pressure transducer connected to a Budd strain indicator. The calibration of this system is explained in Appendix I. When the desired pressure has been reached and set, the separation distance between the horn tip and the specimen is then measured. The teflon spacers on the three micrometer screws are loosened such that adjustment of the micrometer lifts can be made. The lifts are adjusted by placing a feeler gauge between the horn tip attachment and the stressed specimens.

When the spacing reaches .024 inches uniformly over the entire button surface, the teflon set-screws are tightened to eliminate premature back-off of the micrometer lifts. The stabilizer plate is then secured by the three socket head screws to prevent vibration of the horn assembly. The spacing is again checked to assure that no

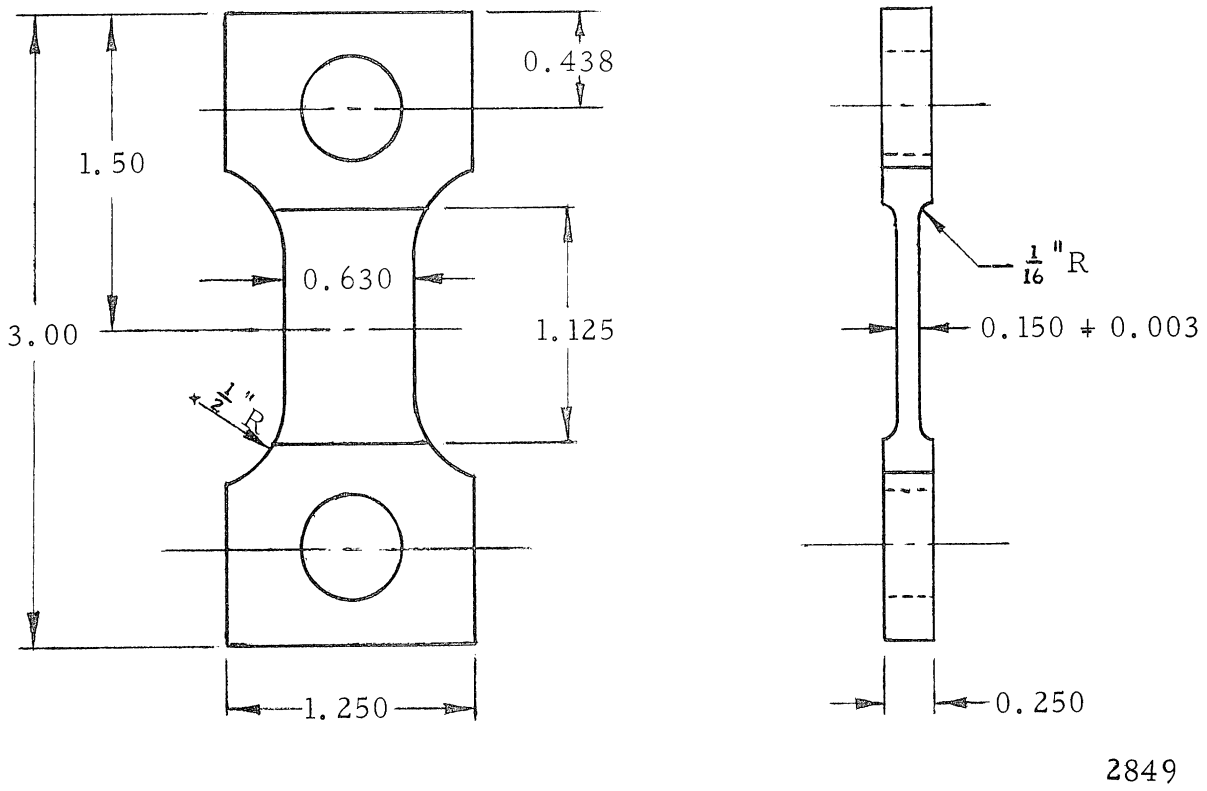

Fig. 49. Dimensional Drawing of Tension-Compression Specimen

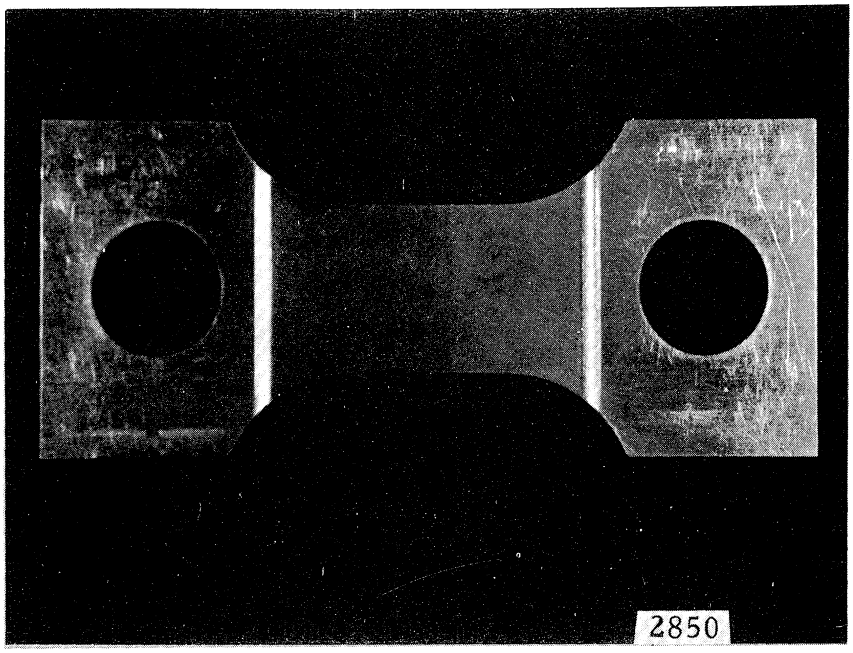

Fig. 50. Fabricated Tension-Compression Specimen Showing Smooth Center Test Section

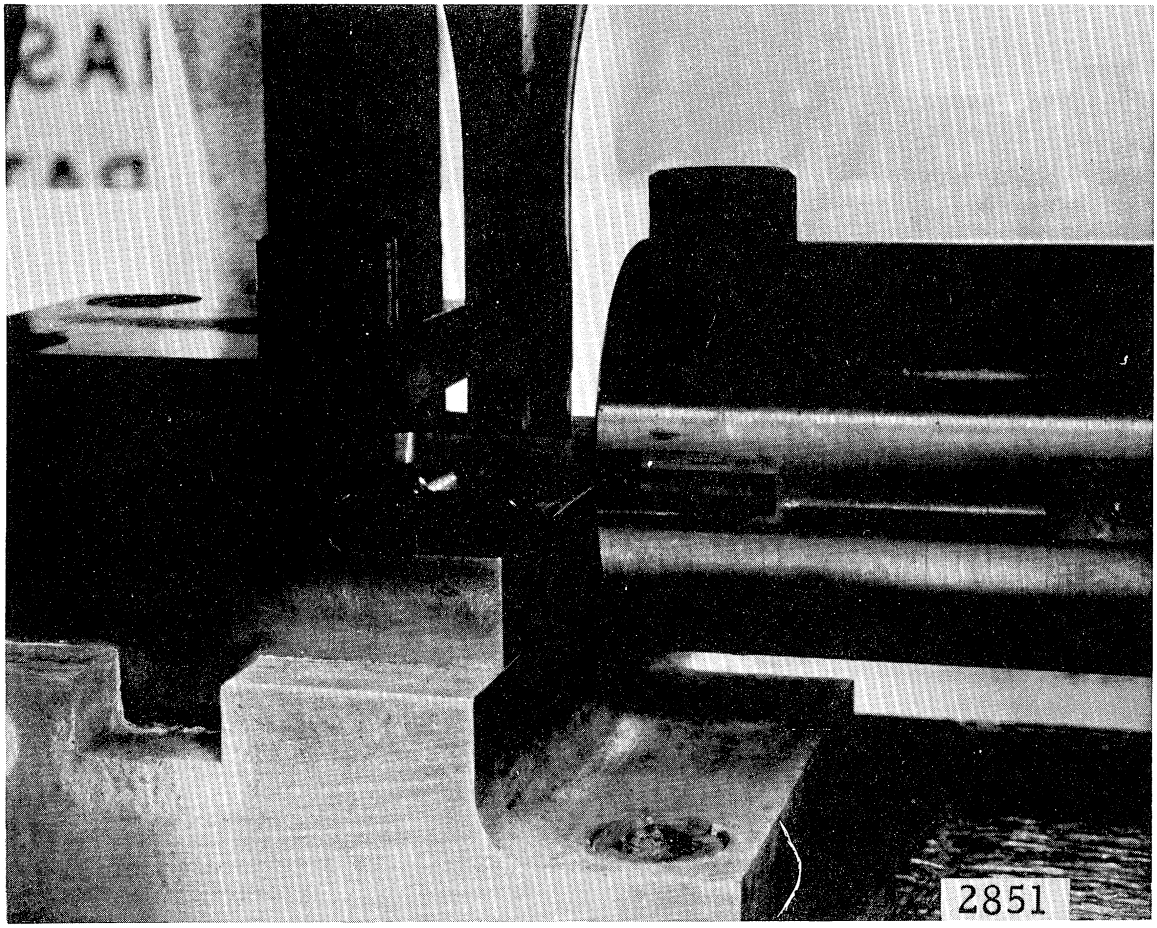

Fig. 51. Specimen Being Held in Test Position

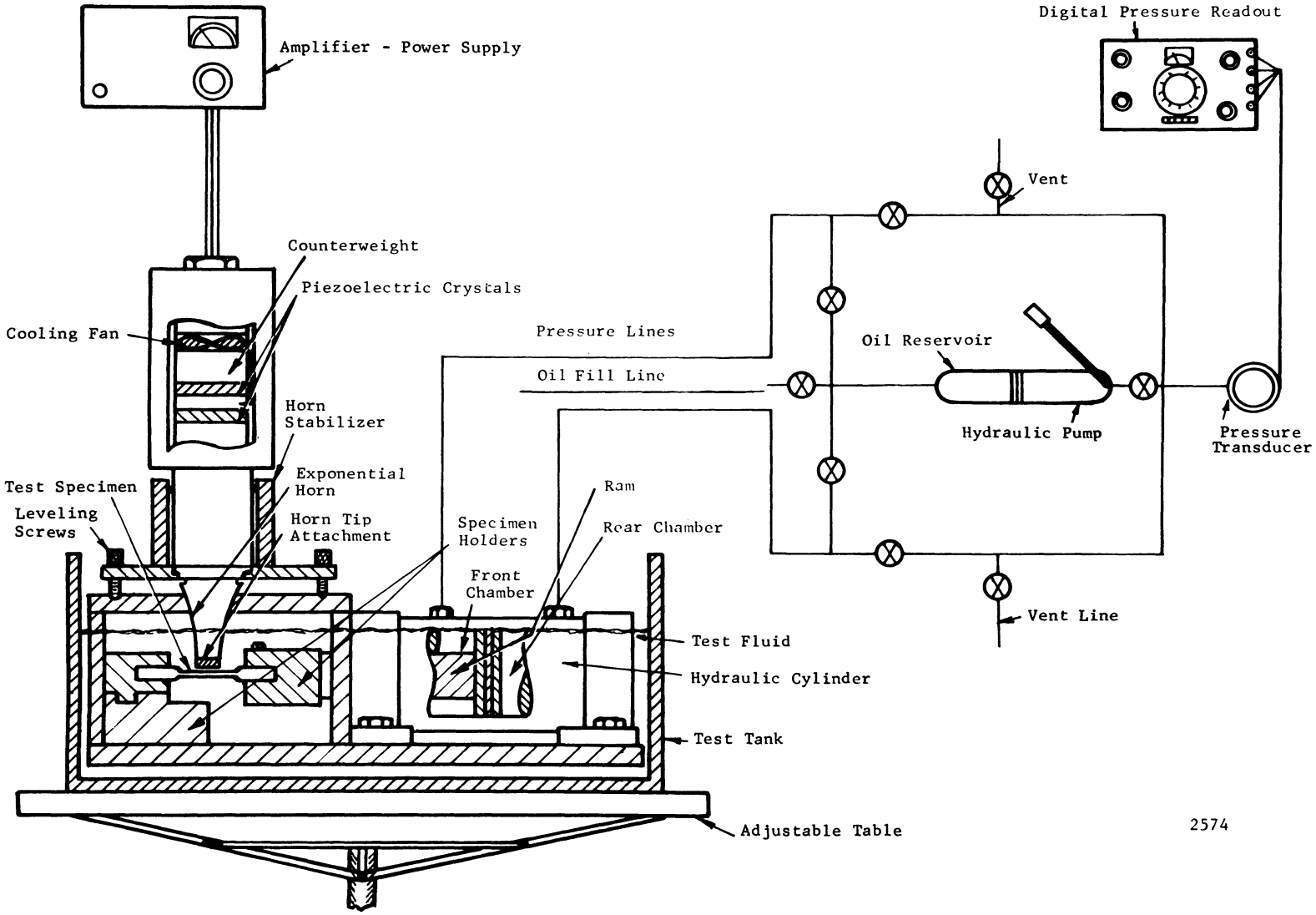

Fig. 52. Schematic Diagram of Test Facility

undesired closure had taken place. The entire system is then immersed into the test tank to a specimen depth of 1.5 inches of water above the lower face of the vibratory horn tip. The test time is preset on a Gralab Universal timer, and the amplifier is started. The horn amplitude is adjusted by setting the output meter to a pre-assigned reading. The setting is calculated as explained in Appendix II which deals with the calibration of the ultrasonic horn. The amplifier output (amplitude), test water temperature, and cylinder pressure are monitored periodically during each test. The entire test system used in this portion of the experiment is pictured in Fig. 53.

IV. CLOSE PROXIMITY TEST RESULTS

A. Experimental Data

1. Conditions and Comparison

a. Comparison of Vibratory Facility and Close Proximity Test

A large amount of the data which has been published from this laboratory (8, 9, 16) has been acquired using the vibratory facility. The test specimens in these studies were the horn tip attachments described previously. When used independently (i.e., conventional open-beaker test) the damage to the tip attachment is much greater than when operated in conjunction with the test specimens in the close proximity test herein described. Since a large amount of damage data had been taken on the material Azarcan 773, (SAE 660), this material was chosen to compare the conventional vibratory test with the vibratory close proximity test. Test results are shown in Fig. 54 as cumulative weight loss vs. total test time.

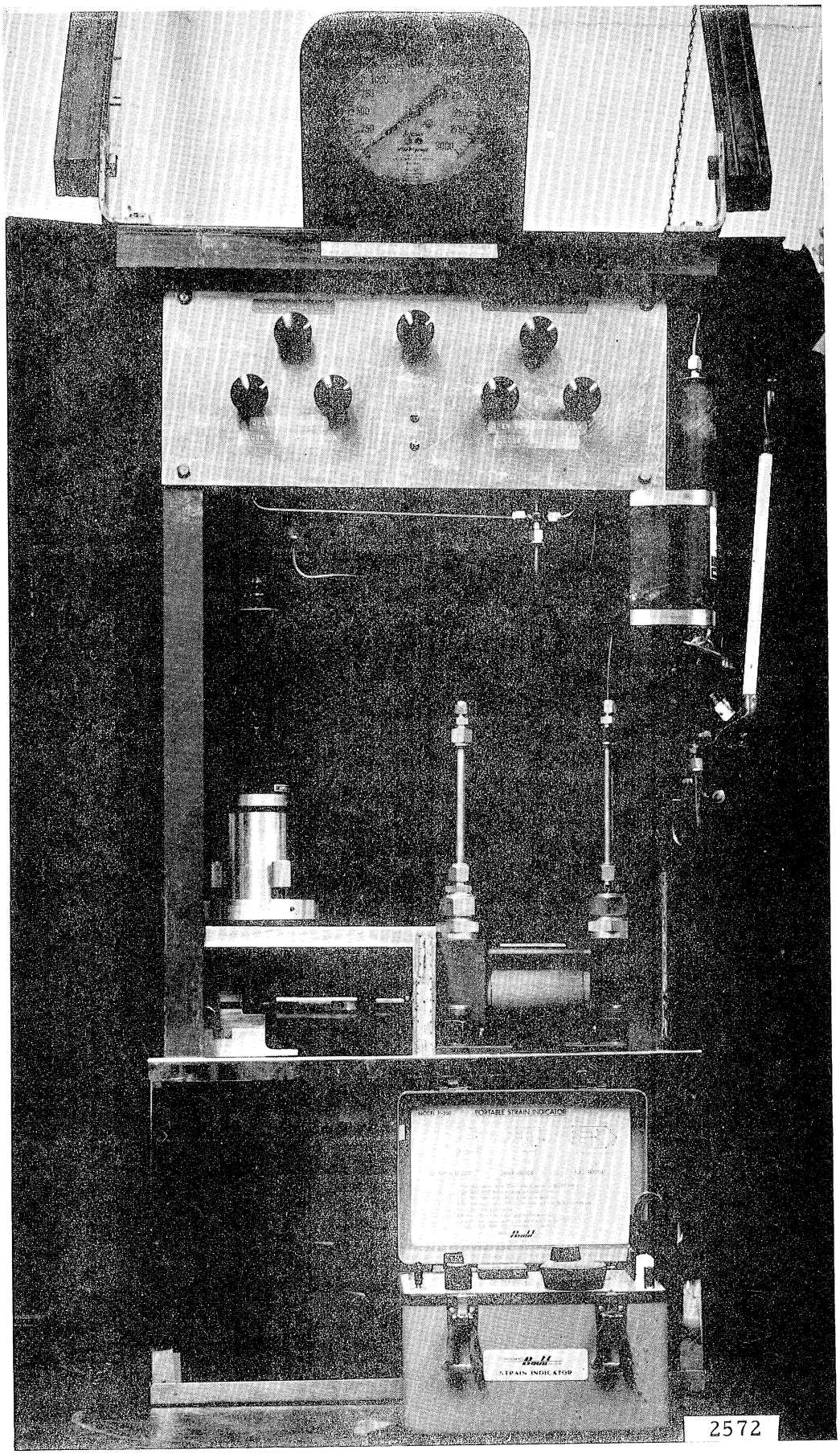

Fig. 53. Tension-Compression Test System

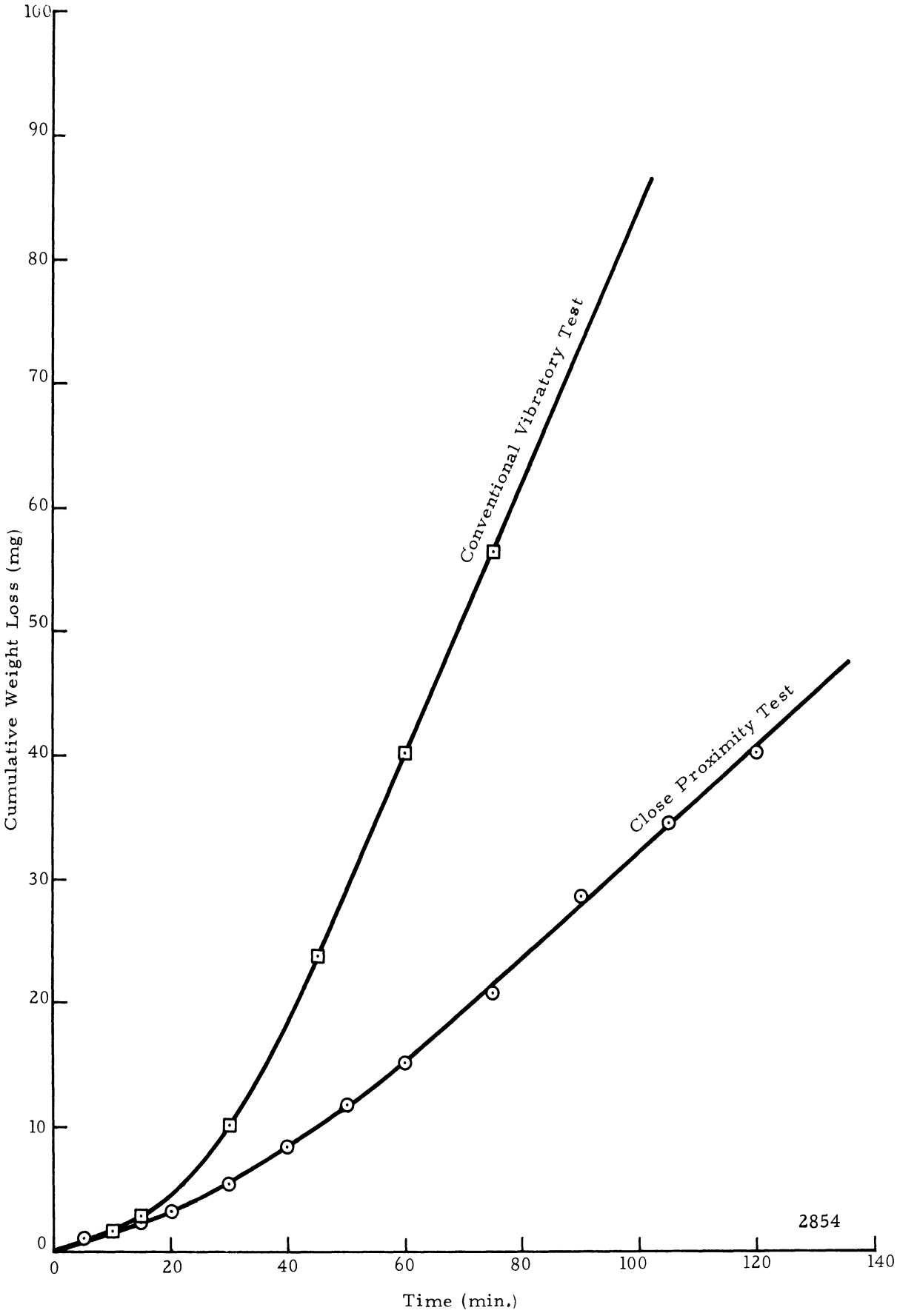

Fig. 54. Comparison of Close Proximity Vibratory Test with Conventional Vibratory Test Using SAE 660 as a Test Material

Both the vibratory and close proximity test show comparable periods of very little damage, as other investigators have mentioned (17, e.g.), and which have come to be known as the "incubation period." After this initial period of approximately 25 minutes, the damage curves separate. The vibratory facility shows a damage rate of about 1.1 mg/min. whereas the close proximity test shows about 39% of this rate (0.43 mg/min.).

b. Damage Versus Separation Distance

The early data published from this laboratory (4) concerning the separation distance between the horn tip attachment and the damage specimen showed a peaked curve of damage rate vs. separation distance. The optimum separation distance was approximately 0.018 inches. This data was run at less than the two mil double amplitude desired for this study. Hence, the experiment was rerun using a calibrated 2 mil double amplitude, and SAE 660 brass as a test material. The damage versus distance curve is plotted (dark solid line) in Fig. 55. The optimum separation distance was again about 0.018 inches. However, the curve shows a somewhat broader peak than in the previous test (4). Some liberty has been taken with the previous data (dashed line) by allowing one point to fall below the curve, so the peak is much broader than previously reported. Even though the material previously used was much less cavitation resistant (1100-0aluminum) and the amplitude substantially less, these opposing factors approximately cancel so that the two curves are quite similar. These new data were used as the criterion for separation distance. A distance of 0.024 inches was chosen so that the results would be relatively insensitive to distance and avoiding the rather sharp decline in damage rate below 0.018 in. separation. All tensile-compression test reported here were made at this distance.

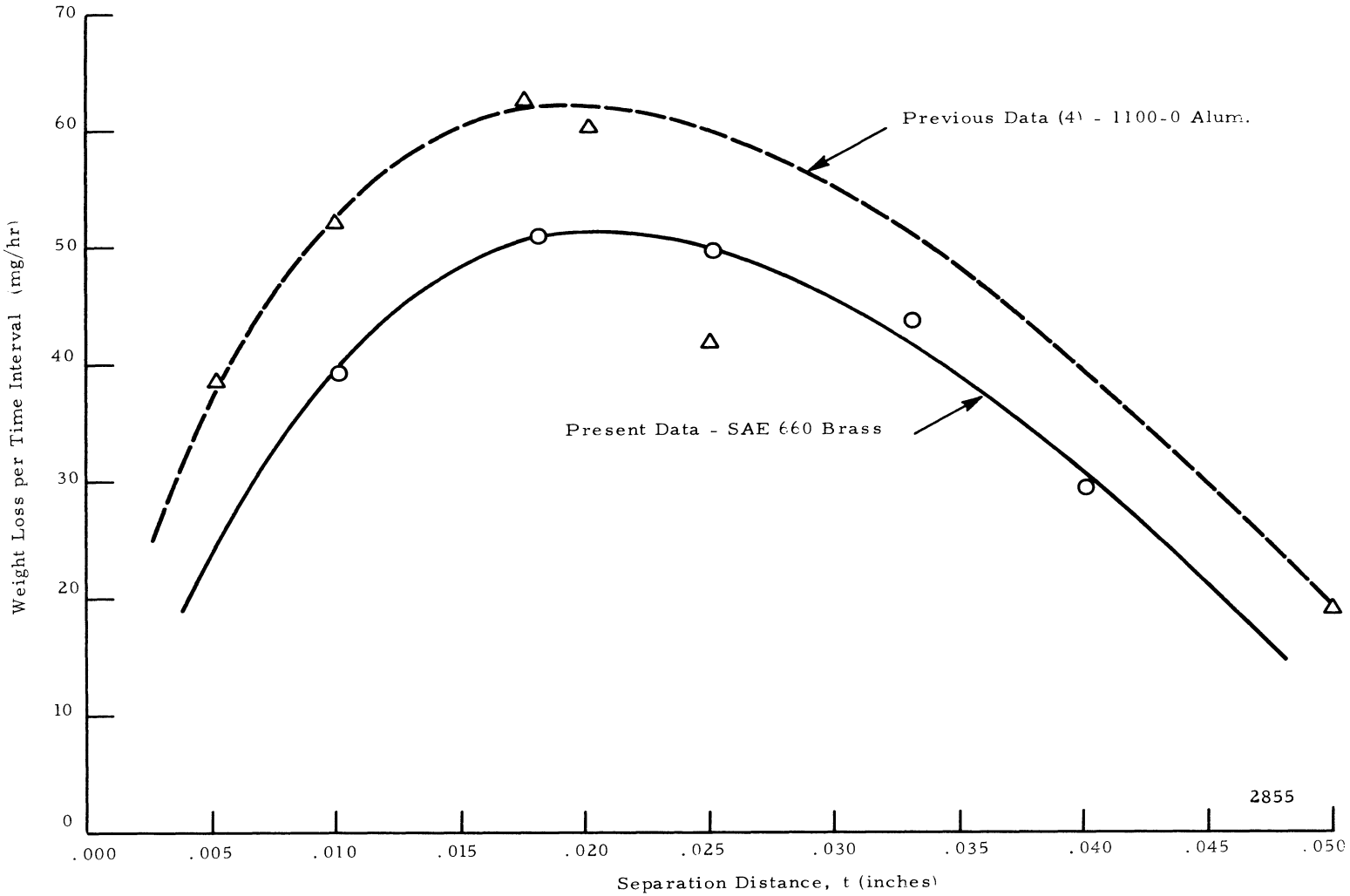

Fig. 55. Effect of Separation Distance on Damage in the Close Proximity Test

c. Wear Patterns

1.) Horn tip: During the first stages of test an interesting circular damage pattern was observed on the horn tip attachments. These erratic patterns became the limiting factor in the longevity of these components which were fabricated of 304SS. Fig. 56, 57, 58, 59, and 60 show a sequence of damage patterns. Fig. 56 shows the surface of a tip attachment as prepared (ground), and serves as a reference to the remaining figures. Fig. 57 shows a horn attachment after 3.25 hours of testing. An outer ring of damage is visible indicating that the outer portion of the surface is being selectively attacked. The narrow undamaged outer rim beyond the damage ring, as well as the center section, still show grinding marks, i.e. very little damage has occured here. Fig. 58 shows the same attachment after 10 hours. The outer rim still shows an area with no damage, however; although some damage is now visible in the center section. The highest concentration of damage still occurs in a ring at a radius of about 0.250 in. The damage now begins to show deep holes or gouges in this area. Fig. 59 shows the same attachment after 13.5 hours. Fig. 60 is a different attachment after 27.5 hours of exposure. The center section is considerably damaged. However, even more interesting are the holes in the outer rim. As the time of exposure is increased the damage of the center becomes greater and the holes in the outer damage area become even more pronounced.

The surface of the attachments shown in the above figures were traversed using a Bendix proficorder, along the diameter of the specimen (Fig. 58, 59, and 60). The traces all have the same basic pattern showing a deep ridge near the outer edge. The O.D. of the deep outer ridge is about 0.515 inches. The low point in the profile (i.e., pit apex) occurs at about 0.491 inches. The differences in depth from between alternate sides of the attachment are due to the pattern as shown in Fig. 59 and 60. The trace, as taken, passed through one of the deep

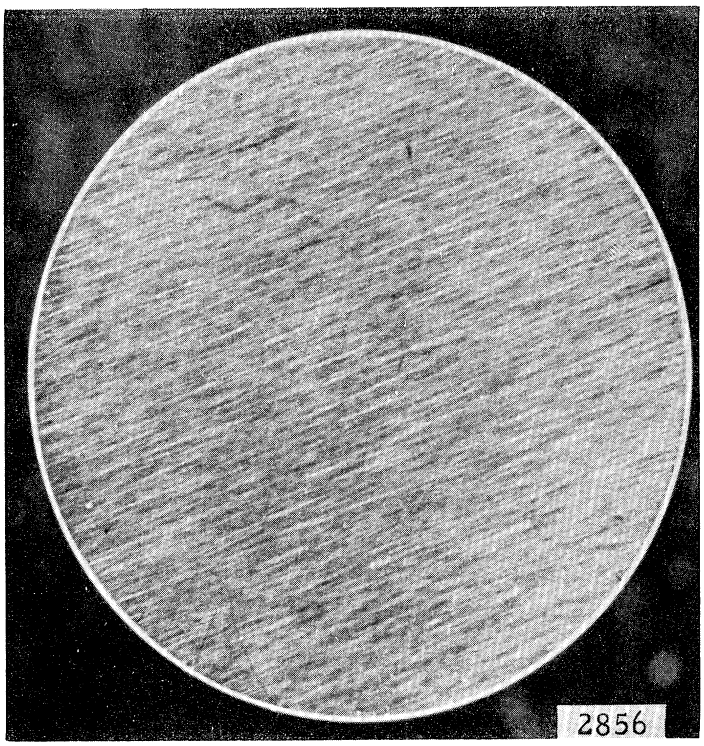

Fig. 56. Ground Surface of Horn Tip Attachment Prior to Test

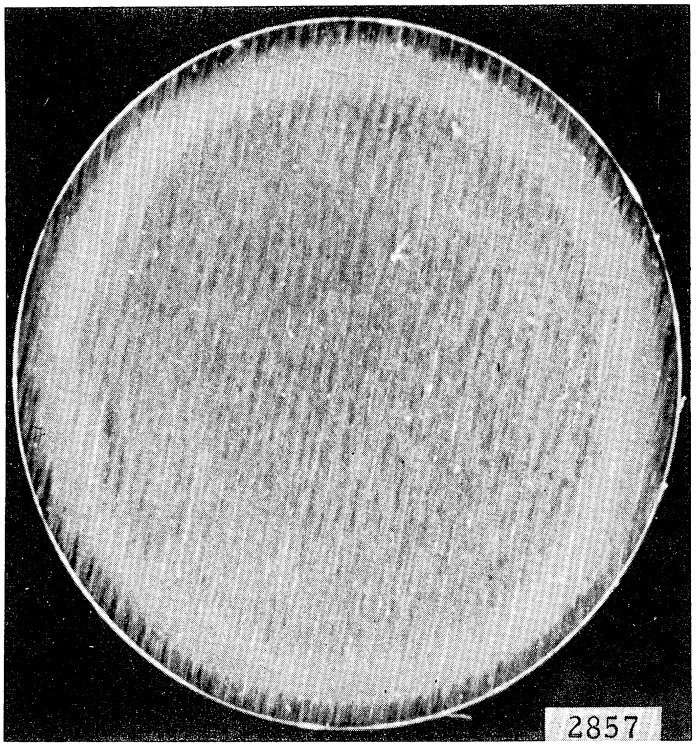

Fig. 57. Horn Tip Attachment After 3.25 Hours of Testing

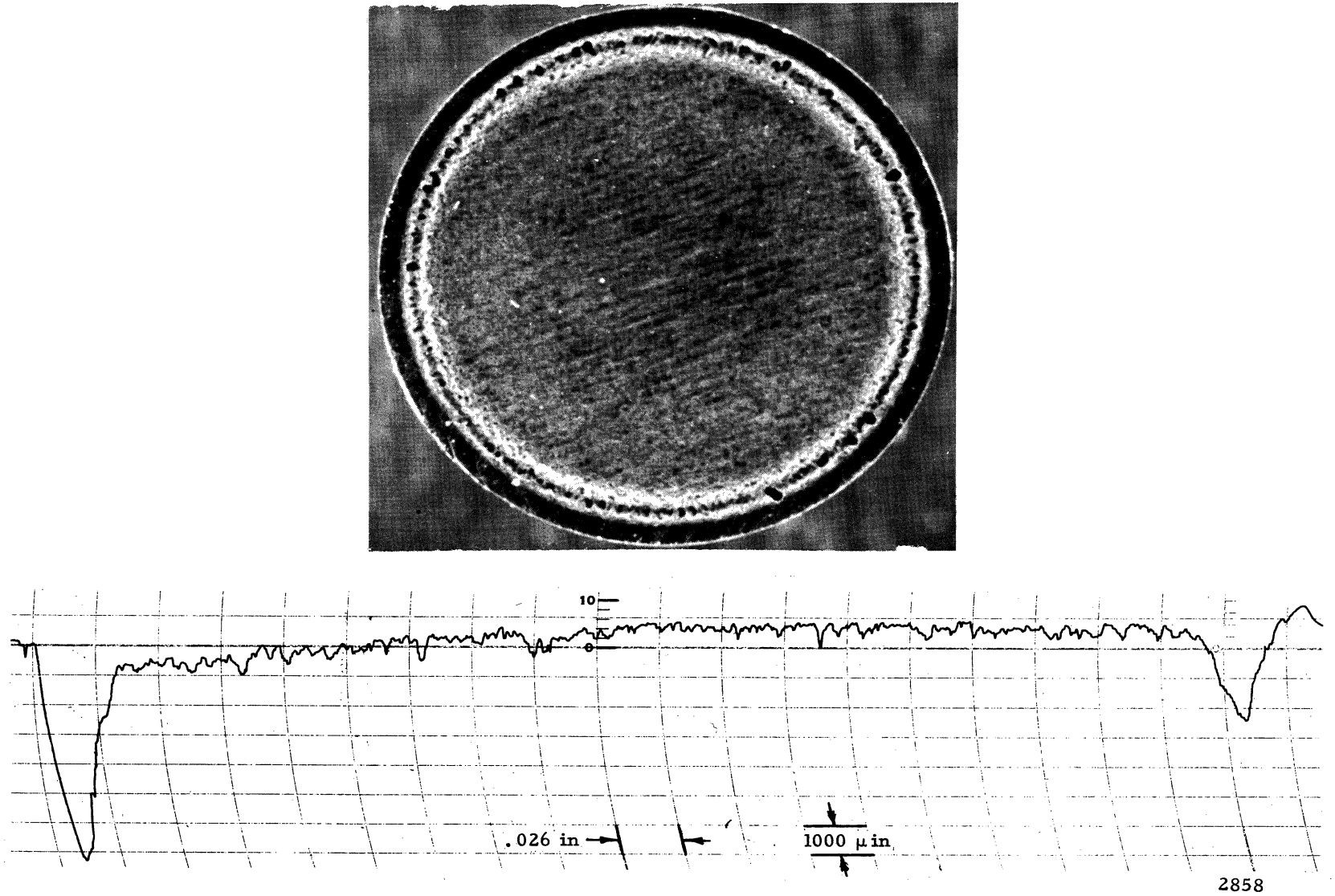

Fig. 58. Horn Tip Attachment After 10.0 Hours of Testing and Assoiciated Proficorder Trace Across Surface

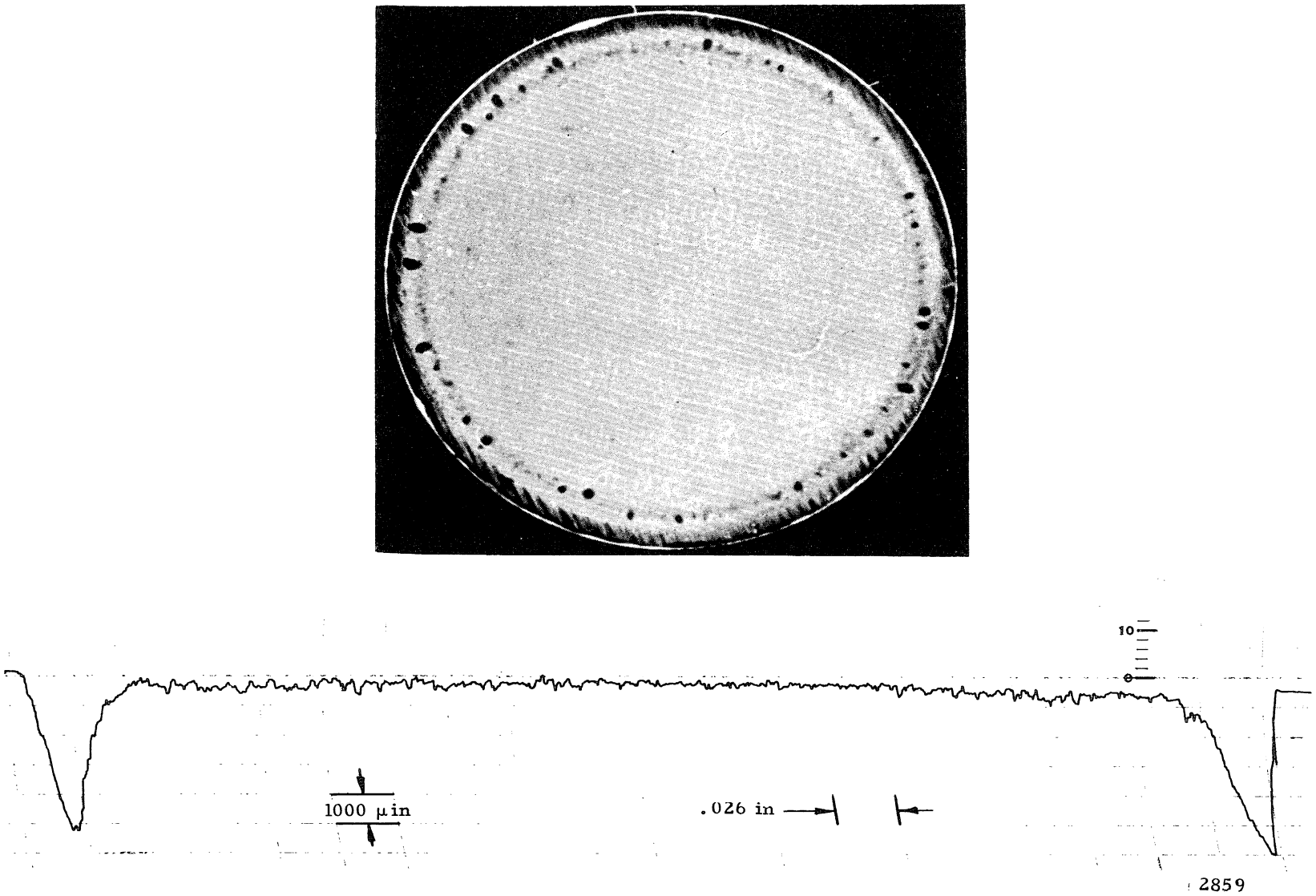

Fig. 59. Horn Tip Attachment After 13.5 Hours of Testing and Assoiciated Proficorder Trace Across Surface

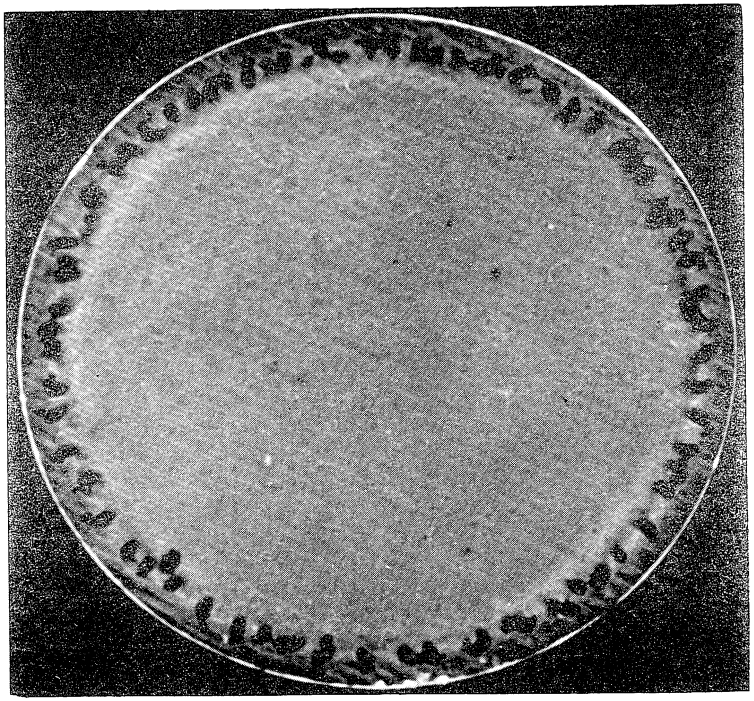

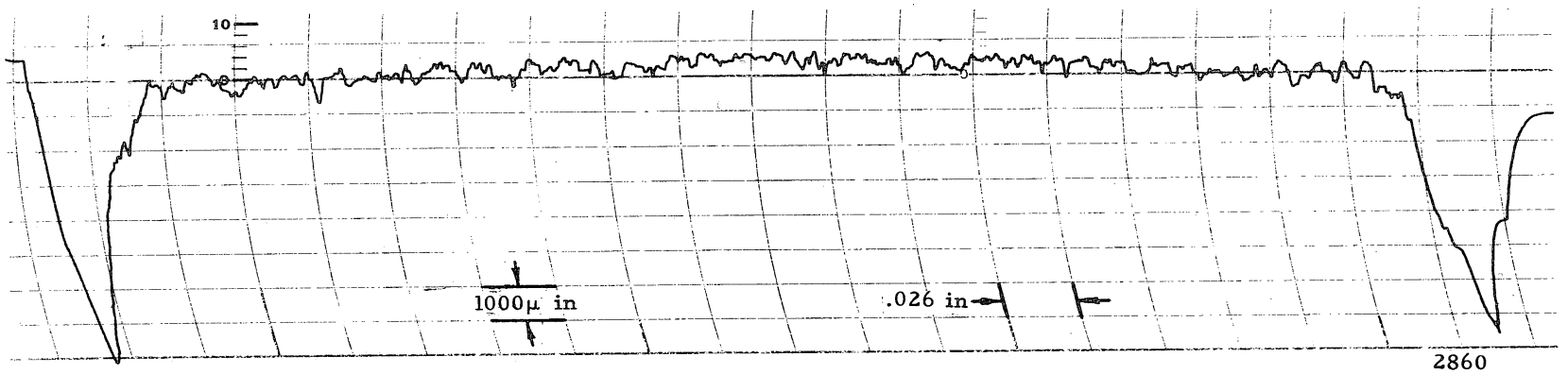

Fig. 60. Horn Tip Attachment After 27.5 Hours of Testing and Associated Proficorder Trace Across Surface

depressions and did not pass directly through a depression on the opposite side since their location is not entirely symmetrical.

2.) Plate Type Specimens: A non-uniform damage pattern similar to that of the horn tip attachment would greatly affect the evaluation of the tensile-compression specimen results. Hence, a number of samples were traced both transversely and longitudinally. It was found that even though the horn tip was greatly deformed at the outer edge, the tensile-compression sample showed a fairly uniform depth of damage pattern across the damage area. It was further found that the damage on the sample was not preferentially oriented, confirming the assumption that edge effects on this type of sample were not a serious problem. (Fig. 61)

d. Slip Film Flow Patterns

The damage patterns generated during the tests suggested that the flow pattern generally concentrated the cavitation cloud near the outer edge of the horn tip attachment. To confirm this a photographic test arrangement was built for use with the vibratory assembly. A schematic diagram of this arrangement is shown in Fig. 62. The camera used was a Beckman-Whitney rotating prism camera capable of 10^6 frames per second. The camera was set at 90^o to the vibratory horn. A 60/40 reflecting mirror was used to transfer the light from directly below the horn tip to the surface of the attachment and then back to the camera lens. The stainless steel horn tip had a highly polished surface giving a high degree of reflection. The fluid container was a glass plate rectangular box with an optically clear glass plate bottom. The horn tip was positioned 0.024 inches distant from the container bottom in order to closely approximate the specimen spacing used in the test program.

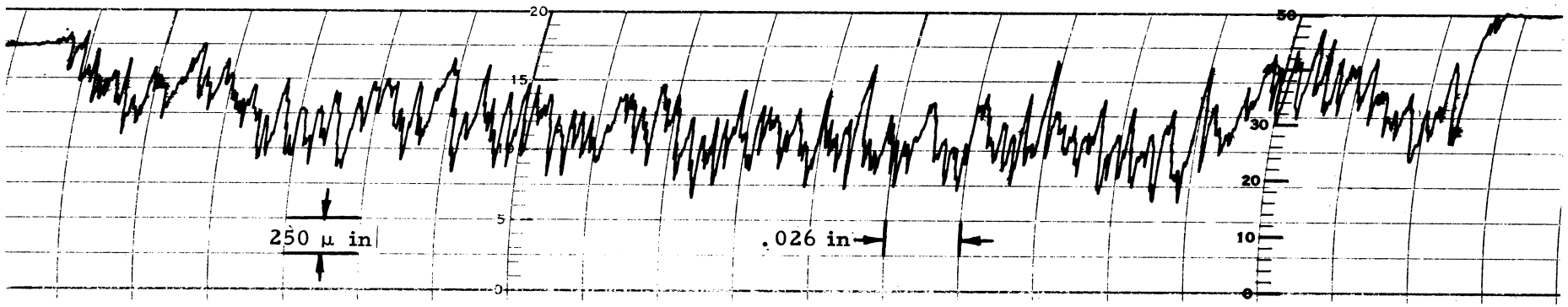

Transverse Trace

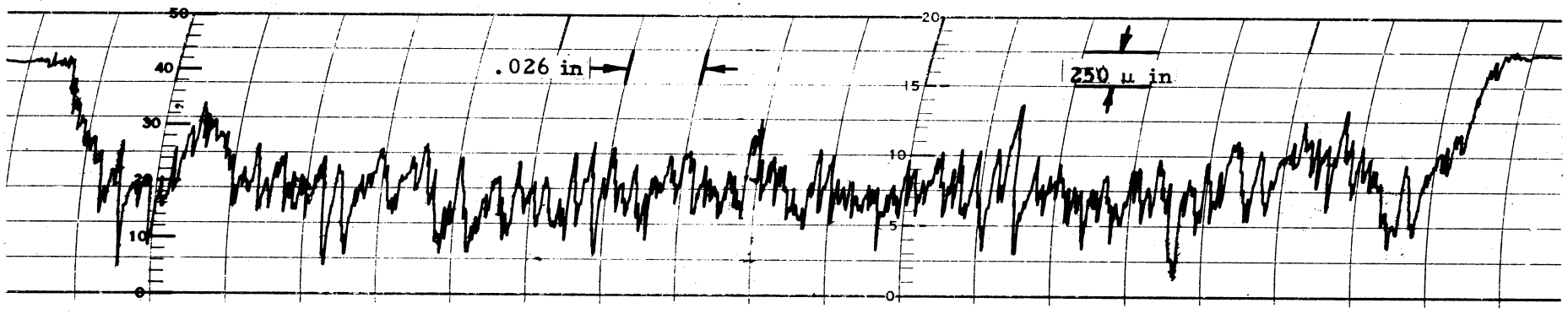

Longitudinal Trace

2861

Fig. 61. Transverse and Longitudinal Proficorder Traces Across Damaged Area of 304 Stainless Steel Specimen

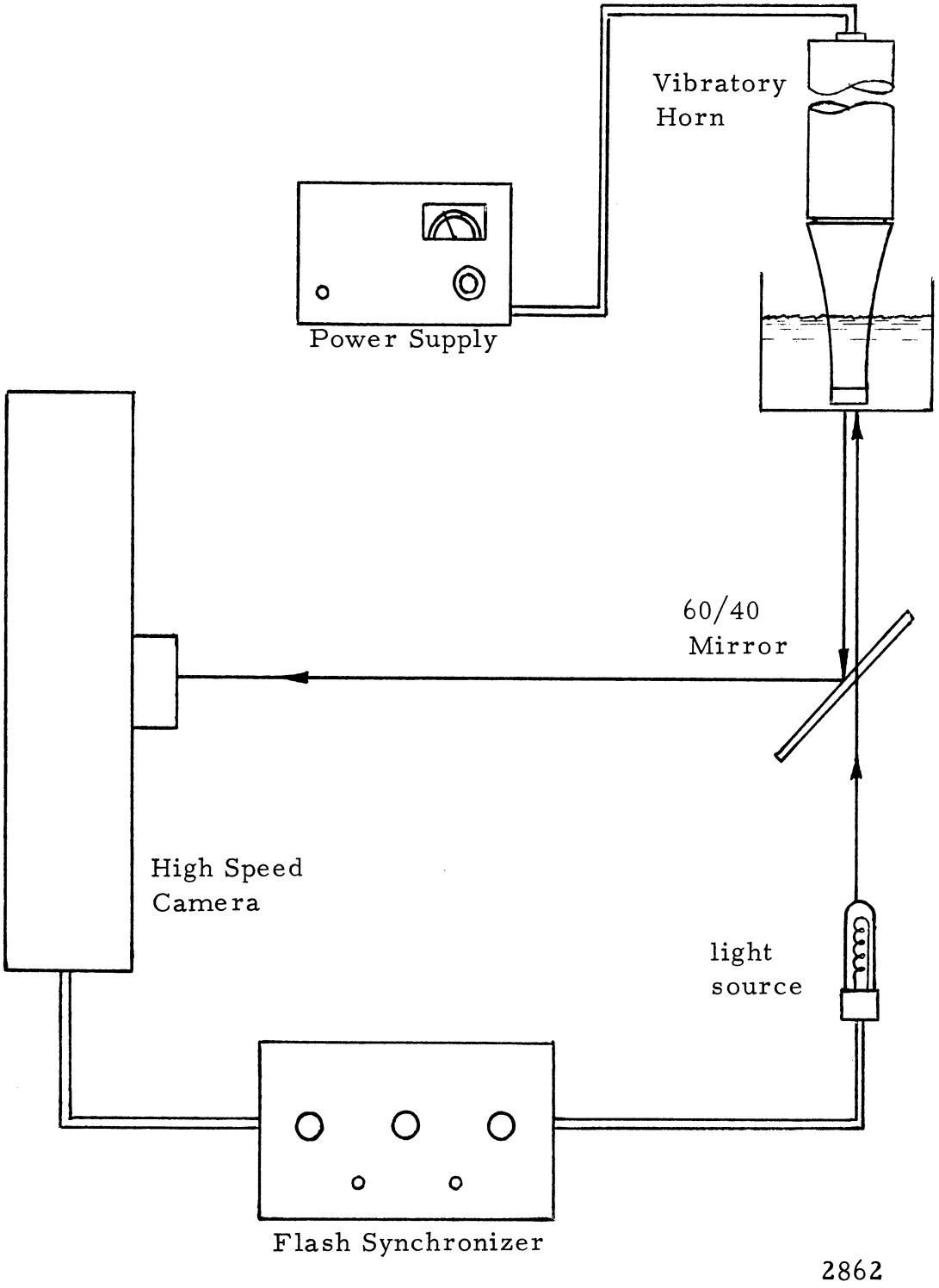

Fig. 62. Schematic Diagram of High Speed Photographic Arrangement for Study of Slip Film Movement

The procedure used in taking the picture was to first start the ultrasonic assembly but hold the amplitude near zero or at such a point where no cavitation was apparent on the horn tip, so that damage would be caused to the polished surface. The turbine of the camera was then brought up to the proper speed to attain 240,000 frames per second. When the appropriate speed was reached, the amplitude of the horn tip was set to 2.0 mils. A flash duration of 0.004 ms was used.

A typical 18 picture sequence of one and one-half oscillations of the horn tip is shown in Fig. 63. The bubble cloud does persist for longer periods of time at the outer edge. The sequence, (each frame is 3.93 microseconds apart) shows the cloud as the dark region in the picture since the bubble cloud has a different diffraction index from the continuous water layer, and the amount of light reflected back to the camera from the cloud is decreased. As the horn tip moves away from the glass surface the bubbles begin to form due to the decrease in pressure near the horn tip surface. The cloud becomes more dense as the tip moves away. When the apex of the oscillation is reached, the cloud becomes most dense. It remains quite dark as the horn tip begins to again descend, increasing the fluid pressure. The bubbles of the cloud begin to collapse rapidly as they slowly move in the radial direction. The outer radial movement is slight as can be noted by following the sequence of Fig. 63 This sequence of photographs was enlarged to 10.5 X in order to measure the movement of the bubble clouds on the face of the horn tip attachment during one cycle. These measurements indicated that the film velocity, as measured by the movement of the center of a particular bubble cloud area, was calculated to be about 54 feet per second. It was also observed that the bubble cloud persists, i.e., not all bubbles collapse, in any one cycle.

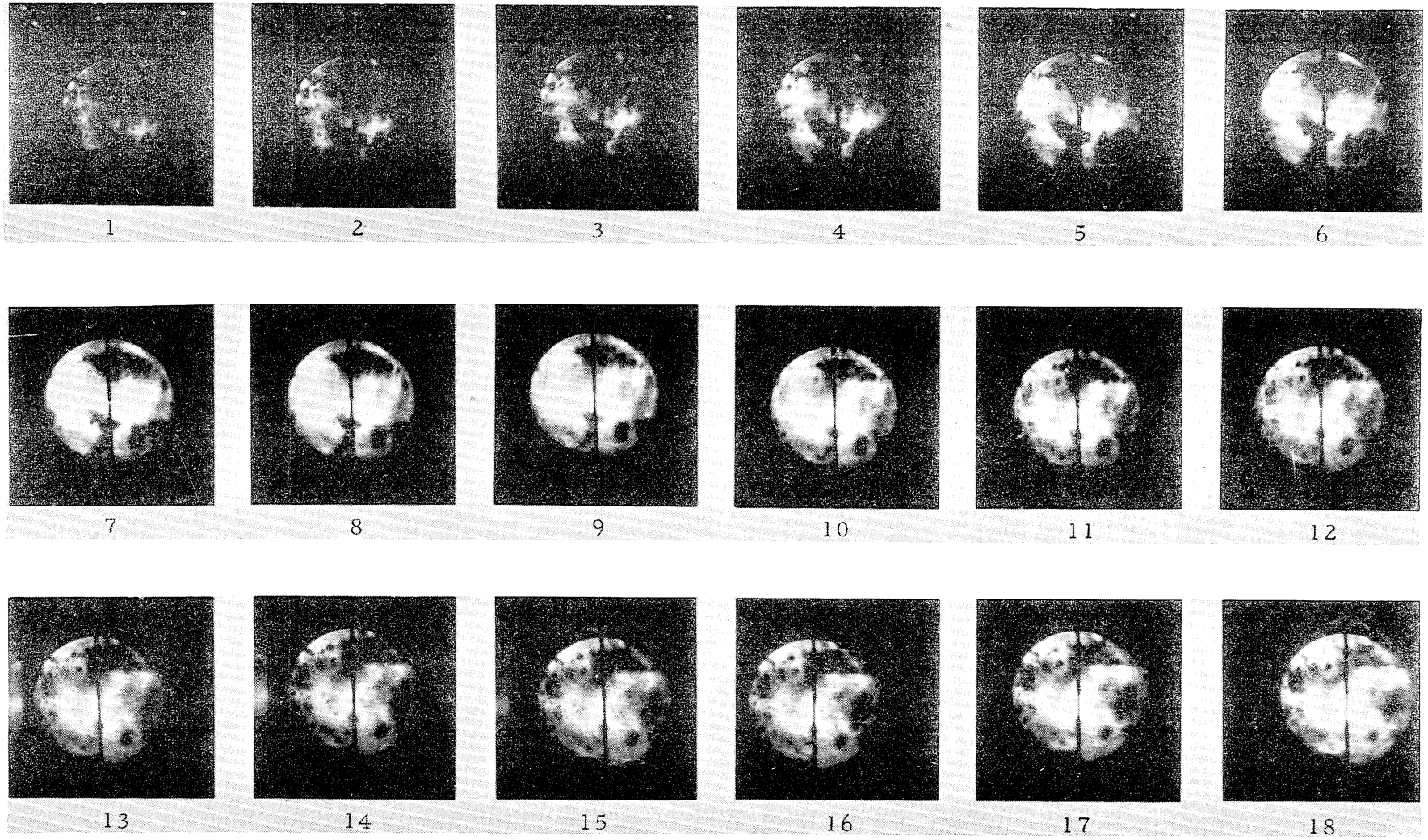

Fig. 63. High Speed Picture Sequence of Cavitation Cloud between Horn Tip and Flat Surface

e. The Test Fluid

The test fluid used in the vibratory test was distilled water with pH about 7.4. The air content was about saturation at room temperature. Since the test vessel was open and the stirring, as the tank was raised and lowered about the hydraulic cylinder to install and remove specimens, was quite vigorous, the air content of the water remained at its saturated value.

The mean test fluid temperature varied somewhat with test period. Its rise was approximately 0.7° C per hour for the long duration tests. In the 15 minute tests, the temperature remained substantially constant over a number of tests since the pause between tests and assembly-disassembly allowed cooling of the water by the $\sim 0.2^{\circ}$C acquired during the test. In general the water temperature was always in the range $23 \pm 3^{\circ}$C for the entire test program. Each individual test was held to $\pm 0.2^{\circ}$C.

2. Materials and Material Properties

a. Materials Selection

The bases for selection of materials for these tests were multifold. As a first consideration it was desirable to choose some materials on which previous work in our laboratory had been done, thereby, possibly giving rise to comparison of data from these tests to previous data. Secondly, it was desired to provide a range of materials with differing yield stresses and hardnesses. Thirdly, it was desirable to investigate the different crystal structures easily available for general fabrication of reactor or fluid system components.

The following materials were finally selected for test: 70/30 brass, Azarcon 773 (SAE 660), OFHC copper, 3003-0 aluminum, magnesium tool plate, 304 stainless steel, and 1020 cold rolled steel.

b. Preparation of Material

The materials were machined from as received stock except for Azarcon 773 (SAE 660) and the aluminum. Azarcon 773 is a specially cast bearing material so that the surfaces of the half inch thick plates were pincushioned with holes left from the casting process. The specimens were cut from the center 1/4 inch of material thereby eliminating as much of the porous material as was possible.

The aluminum as received was 3003-F. It was desired to test a material such as 3003-0, i.e. dead-soft aluminum. To accomplish the required annealing to the dead-soft condition the material was held in a preheated furnace at a temperature of 775^{o} for 30 minutes. The material was then allowed to furnace cool at a rate of 115^{o}/hour to room temperature.

c. Physical and Chemical Properties

Table II lists the chemical compostion and physical property data as reported in the literature (18) for the test materials. Since a comparison of materials with differing yield stress was to be made it was necessary to have the yield and tensile stress values. The available data from manufacturers' handbooks showed wide variations of these particular values for the same alloys and materials. A program of tensile tests was thus initiated using the cavitation test specimens as tensile samples also. In this way the applicable material properties could be evaluated for the specific test specimen configuration. The materials could thus be evaluated on a relative basis since all physical property values were obtained in the same manner. This data is shown in Table III.

TABLE II

Literature Values of Chemical and Physical Properties of Test Materials (21)

Chem. or Phys.	ASTM B 30 SAE 660	ASTM B 36 65/35 Brass	ASTM B 48 OFHC Copper	ASTM B 209 3003-AL	AISI 304SS	AZ31 B Magnesium Alloy	SAE 1020 Cold Roll
Cu (%)	82-84	64-65.8	99.95 min	0.2 max		.05 max	
Fe (%)	.15 max	.05		0.7 max	Remainder	.005 max	Remainder
Sb (%)	.30 max						
Mn (%)				1.0-1.5	2.0 max	.2	.3-.5
Zn (%)	2.5-4.0	34-35.8		0.1 max		.7-1.3	
Al (%)	.005			96.9-97.4		2.5-3.5	
Mg (%)						95.55	
Sn (%)	6.5-7.75						
Pb (%)	6.5-7.75	.15 max					
C (%)					.08 max		.18-.23
P (%)	.03						.04 max
S (%)	.08 max						.05 max
Si (%)	.003 max			0.6 max	1.0 max	.05 max	.1 max
Cr (%)					18-20		
Ni (%)	.5 max				8-11	.005 max	
Others (%)			.05	.05 max		.3 max	
Density(#/m^3)	0.322	0.306	0.323	0.099	0.291	0.064	0.29
Hardness	50-60 BHN	55 R_B	25 R_B	28 BHN	135-185 BHN	73-80 BHN	110-145 BHN
Coef. of Exp. (/^oF)	10×10^{-6}	11.3×10^{-6}	9.9×10^{-6}	12.9×10^{-6}	8.8×10^{-6}	14.5×10^{-6}	9.1×10^{-6}

TABLE III

Measured Material Properties for Test Materials

Item / Material	Hardness $DPH_{1\ kg\ load}$	Density gm/cc	Elongation %	Yield Strength	Tensile Strength	Modulus of Elasticity
Brass (65/35)	146.1	8.47	39.3	48,879	60,473	15.7×10^6
1020 Carbon Steel	227	7.70	25.9	89,725	96,515	31×10^6
304 Stainless Steel	315	7.85	16.75	40,990	99,419	29×10^6
SAE 660 Bronze ASTM B 144	174.3	8.93	17.3	17,545	22,488	6×10^6
Magnesium Tooling Plate	88.5	1.77	25.5	24,120	39,225	6.5×10^6
Alum. 3003-0	51.2	2.74	54.1	6,775	15,864	9×10^6
OFHC Copper (7/8 hard.)	96.8	8.94	54.3	28,200	33,345	$16. \times 10^6$

The effect of rolling direction on the tensile properties was also investigated for both aluminum and copper. Fig. 64 represents the tensile tests which compare the effect of rolling direction perpendicular and parallel to the force direction on the specimens. For copper specimens, the yield point of the parallel-rolled specimen is much higher (21.3%) than that of the perpendicular-rolled specimen, whereas the tensile strength of the perpendicular rolled specimen is only $\sim$ 2% less than that for the parallel rolling. The effect of direction here is then primarily on the yield strength of the material. No effects of rolling direction are noticeable for the aluminum tensile specimens.

3. Tension-Compression Tests

a. Results of Tension Compression Tests

The materials most extensively studied were brass copper and aluminum. Other materials reported here are a 1020 cold roll steel, magnesium alloy containing 3% aluminum, 304 stainless steel and a bearing bronze, SAE 660. The accummulated data are shown plotted in Figures 65 through 89.

The data acquired was analyzed by obtaining,first, cumulative weight loss data in short time intervals over a specific period of time for a number of specimens. The weight loss rate for that total accumulated time was then calculated based on the slope of the straight line portion of the weight loss versus time curve. These calculations were made for each of the three modes under test, i.e., no force (the control), compression, and tension. All data presented here are tabulated in Table IV.

Rather than take a number of different values of stress into account a standard stress level of approximately 75% yield stress of each material was adopted and used throughout both the tensile and compressive tests.

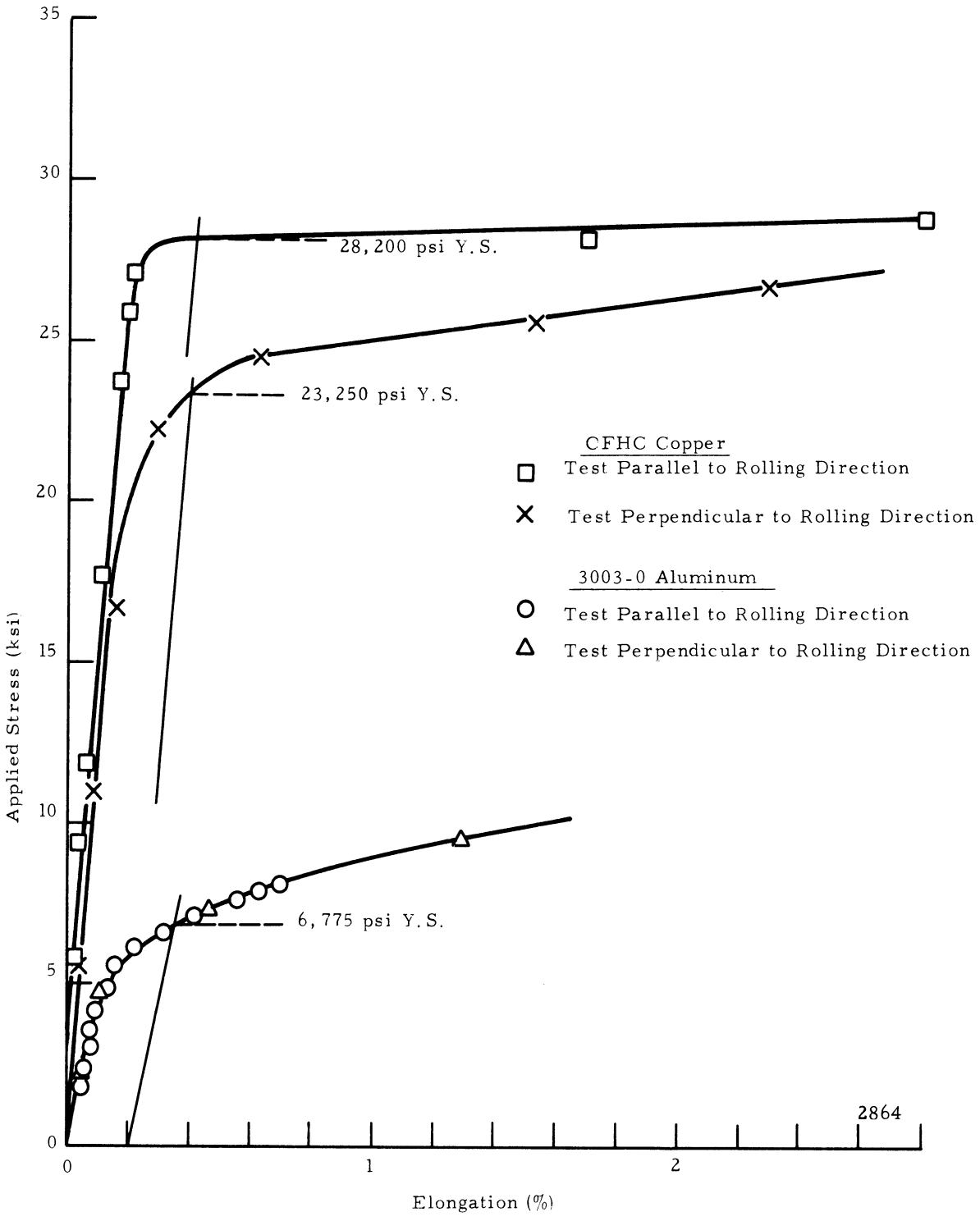

Fig. 64. Effect of Rolling Direction on Stress-Strain Curves for OFHC Copper and 3003-0 Aluminum

TABLE IV

Summation of Damage Rates for Tensile-Compression Test

Material	Structure	Damage Rate (mg/min)			Linear Rates $\Delta C\% = \frac{CR-ZFR}{ZFR} (\times 100)$	Linear Rates $\Delta T\% = \frac{TR-ZFR}{ZFR} (\times 100)$	Initial Rates $\Delta C\% = \frac{CR-ZFR}{ZFR} (\times 100)$	Initial Rates $\Delta T\% = \frac{TR-ZFR}{ZFR} (\times 100)$
		Zero Force	Compression	Tension				
Parallel Rolling Direction								
Brass (65/35)	FCC	0.4099	0.4026	0.4795	-1.78	16.94	+5.89	+53.7
Aluminum 3003-0	FCC	2.369	2.1845	2.518	-7.79	6.29	+7.67	+14.06
SAE 660 Bronze	FCC	0.3754	0.3733	0.3898	-0.56	3.84	-16.59	-16.09
OFHC Copper	FCC	1.708	1.735	1.761	1.58	3.10	+17.63	+9.32
304 Stainless Steel	FCC	0.07408	0.07510	0.07229	1.38	-2.42	-15.85	-53.4
1020 Carbon Steel	BCC	0.1772	0.1843	0.1831	4.46	3.33	-51.80	-18.0
Magnesium Tooling Plate	HCP	0.2186	0.1885	0.2469	-13.77	12.95	-47.8	+6.58
Increased Force - 150% Y.S.* **								
OFHC Copper	FCC	1.708	1.714	1.745	0.35	2.17	-16.2	-16.72
Perpendicular Rolling Direction								
Aluminum 3003-0	FCC	2.369	2.458	2.614	4.19	10.34	+56.40	+23.41
OFHC Copper.	FCC	1.708	1.664	1.740	-2.58	1.87	+18.77	+8.30
				Av =	-1.42	5.84	-4.24	+1.76

* $\frac{\text{Compression - Zero Force}}{\text{Compression}} \times 100$

** $\frac{\text{Tension - Zero Force}}{\text{Compression}} \times 100$

***All others 75% Y.S.

1.) Brass

Figure 65 is a plot of cumulative damage versus time for brass. The curves generated are all similar in shape to those found previously in the vibratory tests on the horn tip attachments alone.

In the first fifteen minutes of test the amount of damage appears to be highest for the group of specimens with the applied tensile load and lowest for that group which were tested under no applied load. The group of specimens tested under the tensile loading showed a very large difference in linear rate compared to the control or non-stressed specimens. This difference, due to the tensile loading, was calculated to be 16.94% greater than the non-stressed state and 18.72% greater than the compressive loading. The difference between the non-stressed control and the compressive loading is quite small as can be noted in Figure 65. Calculation of the rate indicates that this difference was approximately 1.78%.

2.) Aluminum 3003-0

The aluminum chosen for these tests was an alloy containing 1.2% manganese. This material was chosen for comparison with the other materials of the program having a F.C.C. (Face Centered Cubic) structure. Another consideration was that a paper, published by Shal'nev (3), also concerned with the effects of tensile stress presented data on a material of somewhat the same compostion. In this way a comparison of the data procured in this investigation could possibly be made with Shal'nev's data.

The test program which was initiated for this material was second in magnitude only to copper. Both copper and aluminum were studied to a greater extent than the other materials, due to the rapidity of damage and the rapid fabrication of specimens. The total test duration for the aluminum was held to 16 minutes, using two minute continuous tests with cleaning and weighing intervals between tests.

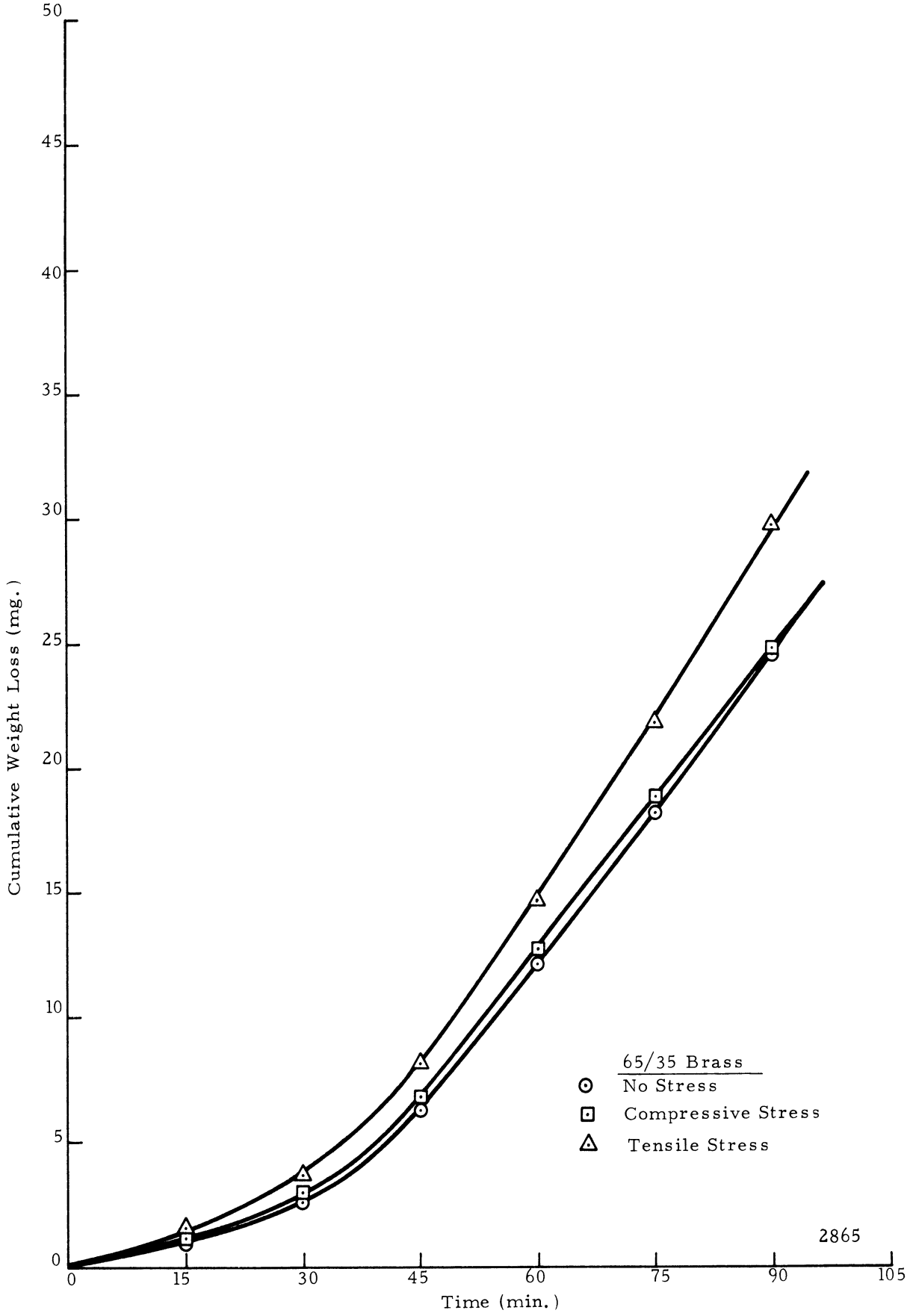

Fig. 65. Effect of External Stress on Cumulative Damage of 65/35 Brass

The scope of this investigation was first the evaluation of the effects of applied stress as compared to a non-stressed control, group, and secondly the evaluation of the effect of rolling direction on the damage rate when the same stresses are applied.

First the specimens with the rolling direction parallel to the direction of applied stress will be considered. The rolling direction here corresponds to that of the other specimens of the F. C. C. group tested. The results of these tests are shown in Fig. 66. As indicated particularly the points at 3 minutes duration, there is very little difference in the incubation period, which here appears to be only 2-3 minutes long. For a total weight loss of approximately 1.2 mg, no large differences could be seen between the different applied stresses. The greater amount of damage did, however, occur in the group which were tested with an applied tensile load. The damage rate stabilized to a constant rate after 4-5 minutes of total test time. The calculated rates indicated that the tensile stress was augmentative to the damage rate providing approximately 6.29% greater damage rate than the control. The effect of the compressive stress, like that of the brass,was to decrease the rate of damage in this case by 7.79%. This decrease was large compared to the other F. C. C. materials tested which showed decreases of only 2% or less, and at times of increases of the same amount. The difference between the tensile and compressive stress was of the order of 14%.

In Fig. 67 the data was plotted for the groups tested with the rolling direction perpendicular to the direction of the applied stress. In the first few minutes of these investigations the amount of damage was greater for the tensile and compressive stressed samples than for the control group. In contrast to the damage which occured with the applied compressive stress parallel to the rolling direction, the damage was considerably greater than the control group when the applied compression was perpendicular to the rolling direction. The effect of the tensile stress was to increase the damage rate even more than when the stress applied was parallel to the rolling direction. To

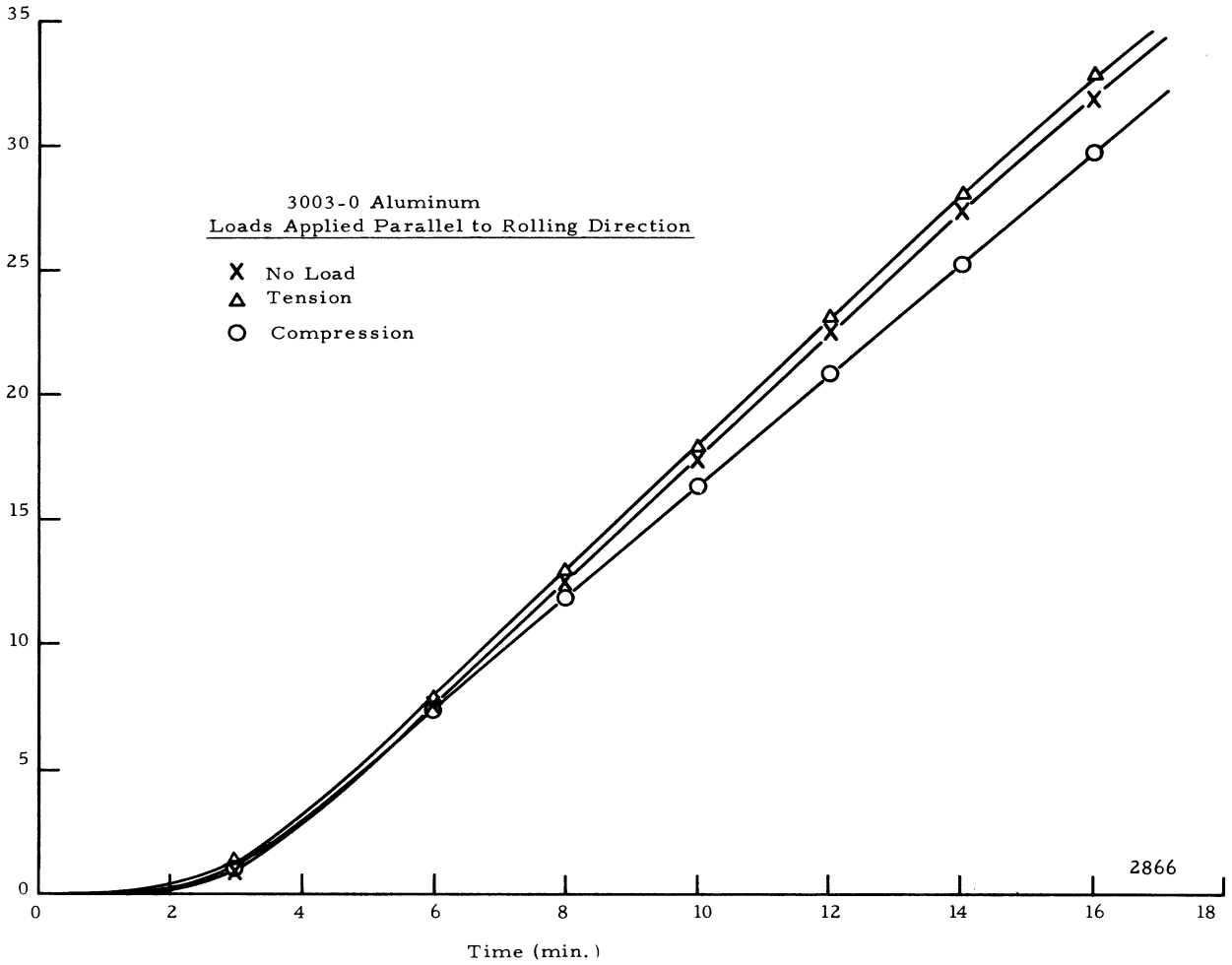

Fig. 66. Effect of External Stress Applied Parallel to the Rolling Direction on Cumulative Damage of 3003-0 Aluminum

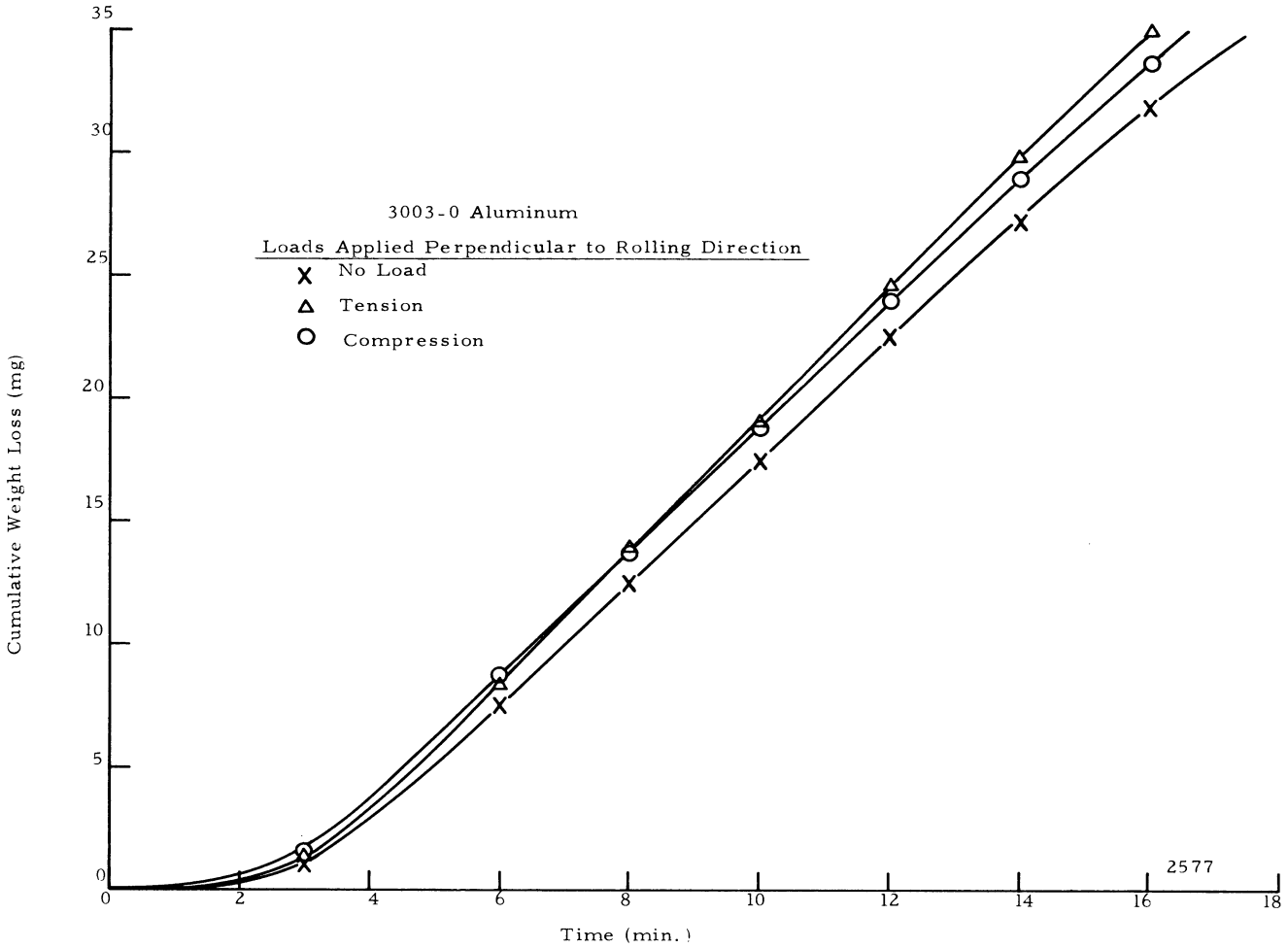

Fig. 67. Effect of External Stress Applied Perpendicular of the Rolling Direction on Cumulative Damage of 3003-0 Aluminum

make a comparison between the effects of tensile and compressive stresses for either rolling direction, the curves of Fig. 66 and 67 were replotted on Fig. 68 and 69. Fig. 68 shows the effect upon damage rate for compression. The rate corresponding to the perpendicular rolling direction was 12.53% higher than that which was tested with the axis parallel to the rolling direction. The differences were not only noticed in the rate, but were present even in the early stages of damage. Fig. 69 shows the effect of rolling direction on the damage rate under an applied tensile stress. The magnitude of the difference is not as great as that found in the case of the compressive load. There is very little difference in amount of damage in the first damage period as is indicated in the figure. The damage rate for the perpendicular direction was 3.81% greater than that for the parallel direction. In general then, the effect of rolling direction on the rate of damage is an increased damage rate in both stress modes when the stress is applied perpendicular to the rolling axis. The greatest effect is in the compression mode and actually causes an increase in rate over that of the control group.

3.) Azarcon 773 (SAE 660)

The damage rates of the SAE 660 as shown in Fig. 70 do not show substantial differences between the different modes of applied stress. The initial stages of damage show that the zero stress group of specimens has an average weight loss larger than either stressed group. The shape of the curves indicate, however, that the rate of damage after the incubation period is greater for the tensile loading than for the non-loaded group by approximately 3.85%. The effect of compressive load appears to be a slight decrease in the damage rate over that of the non-stressed specimens. The total difference between the tensile and compressive loading amounts to only a little over 4%.

4.)O. F. H. C. Copper

The largest amount of data, in terms of number of separate specimens per group, was generated with O. F. H. C. (Oxygen

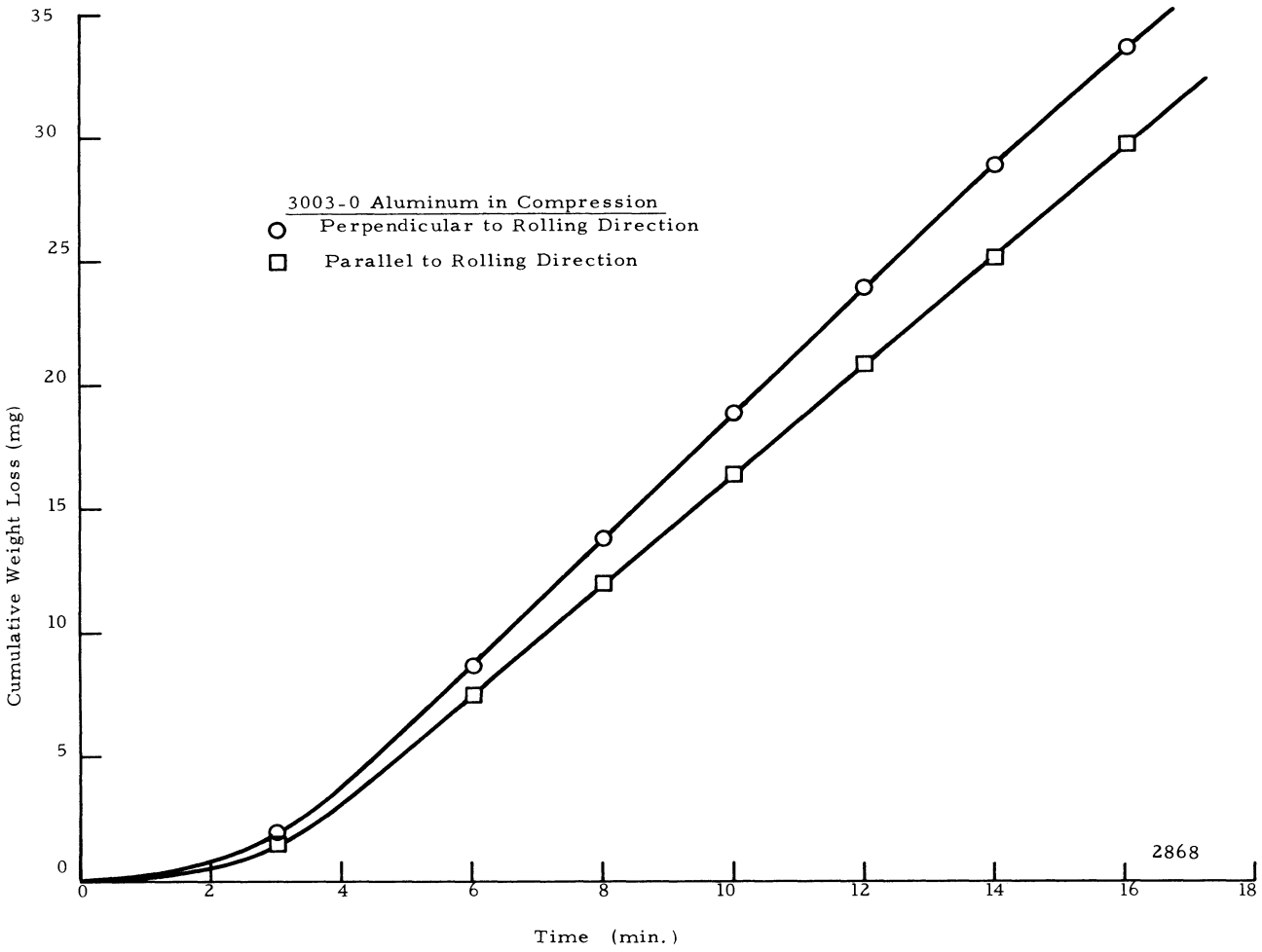

Fig. 68. Effect of the Orientation of External Compressive Stress with Respect of Rolling Direction on Cumulative Damage of 3003-0 Aluminum

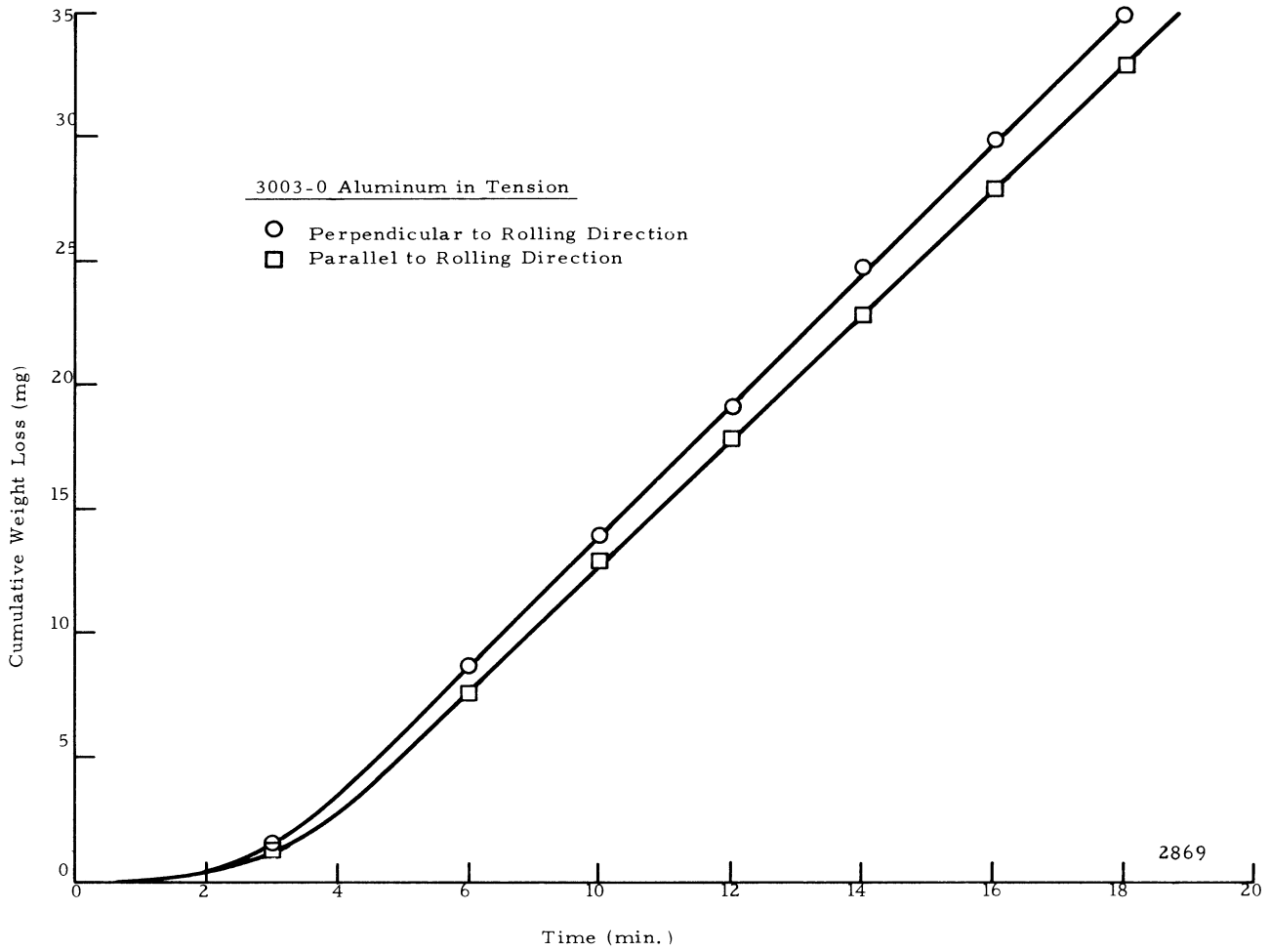

Fig. 69. Effect of the Orientation of External Tensile Stress with Respect to Rolling Direction on Cumulative Damage of 3003-0 Aluminum

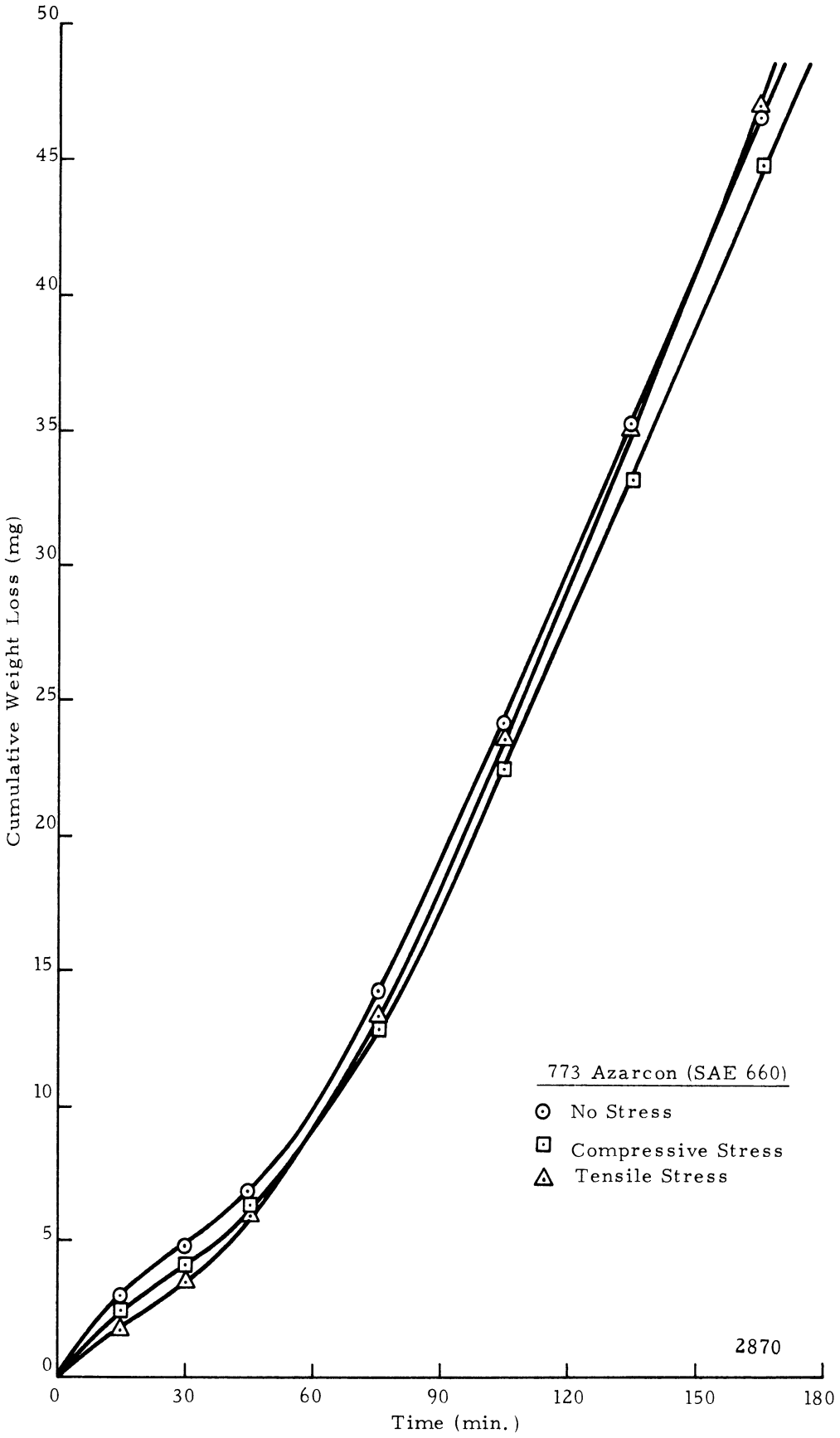

Fig. 70. Effect of External Stress on Cumulative Damage of Azarcon 773 (SAE 660)

Free High Conductivity) Copper. This material was unique to this experiment, since besides representing a F. C. C. structure it was the only pure metal tested. Three sets of separate data were acquired in this test. These represented, like the aluminum, (a) the effect of stress on specimens cut with the stress axis parallel to the rolling direction, and (b) the same effects with a perpendicular rolling direction. In addition, the effect of increasing the stress level to 1.5 times the yield stress was investigated. The latter test was run on specimens which had been fabricated with their axes parallel to the rolling direction.

The general results of applied tensile and compressive loads on the group with axis parallel to the rolling direction are shown in Fig. 71. The data indicated that the differences in damage rate between the different stress modes is not large. The damage vs. time curves are very close in magnitude of damage as well as in rate. The effect of the applied tensile load was to again decrease the resistance of the material to cavitation attack as was the case with most all of the other materials. This decrease, however, accounted for only a 3.10% difference in damage rate between this tensile group and the control. Unlike the aluminum, brass, and SAE 660 the effect of compressive stresses was to increase the rate of damage over that of the control by 1.58%. The calculated difference between the effect on rate between the tensile and compressive loading was 1.48%. The greater rate occurred in the material subjected to an applied tensile load.

Fig. 72 shows results for the group of specimens with axis perpendicular to the rolling direction. The spread for the different stress conditions is even less than that for parallel rolling direction. A decreased damage rate for the compressively stressed group over the control group was shown. The rate was approximately 2.58 % less than that of the control and 4.37% less than the rate due to the applied tensile load. The effect of the tensile load was again to increase the rate of damage over the unstressed group; however, this increase was 1.87%.

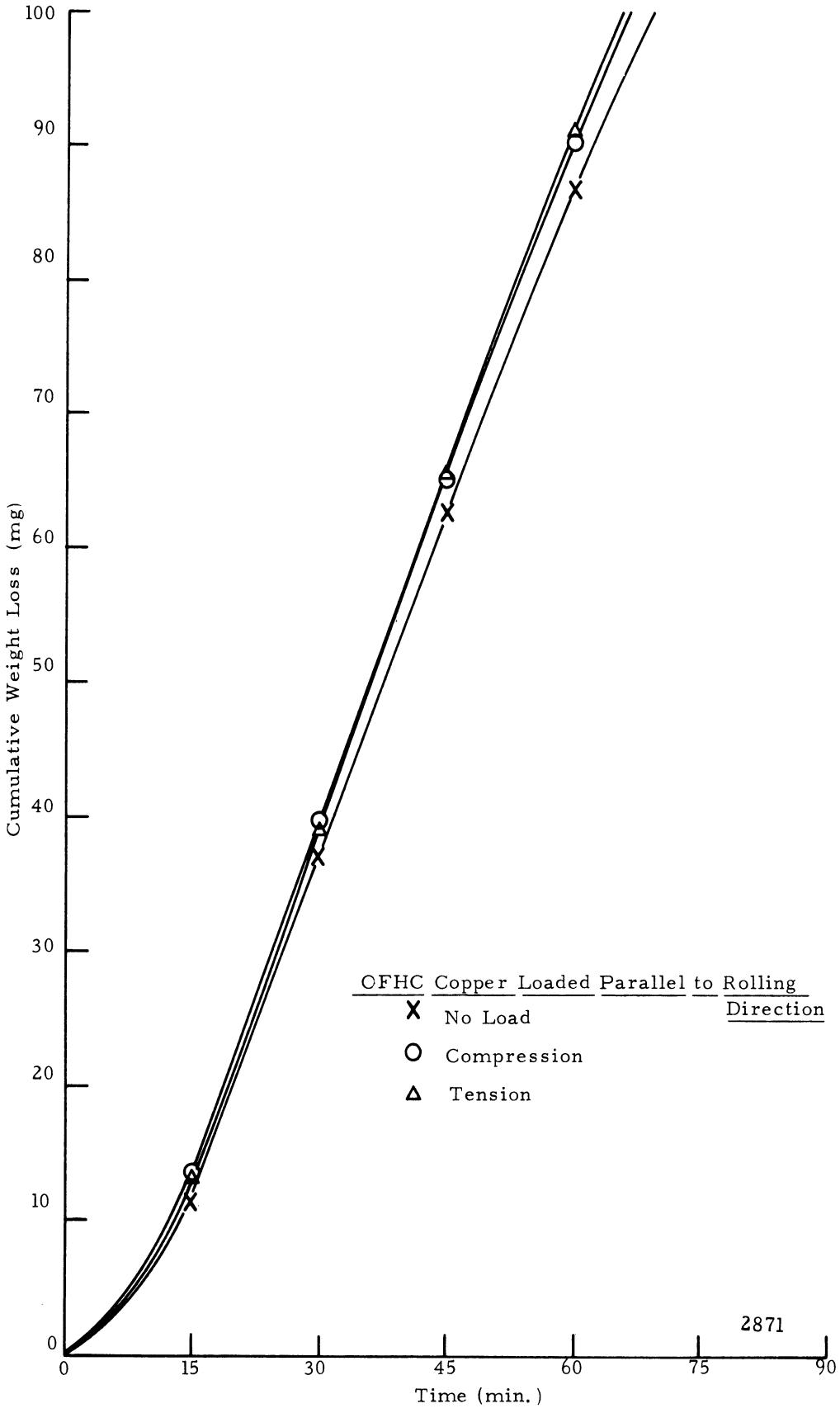

Fig. 71. Effect of External Stress Applied Parallel to the Rolling Direction on Cumulative Damage of OFHC Copper

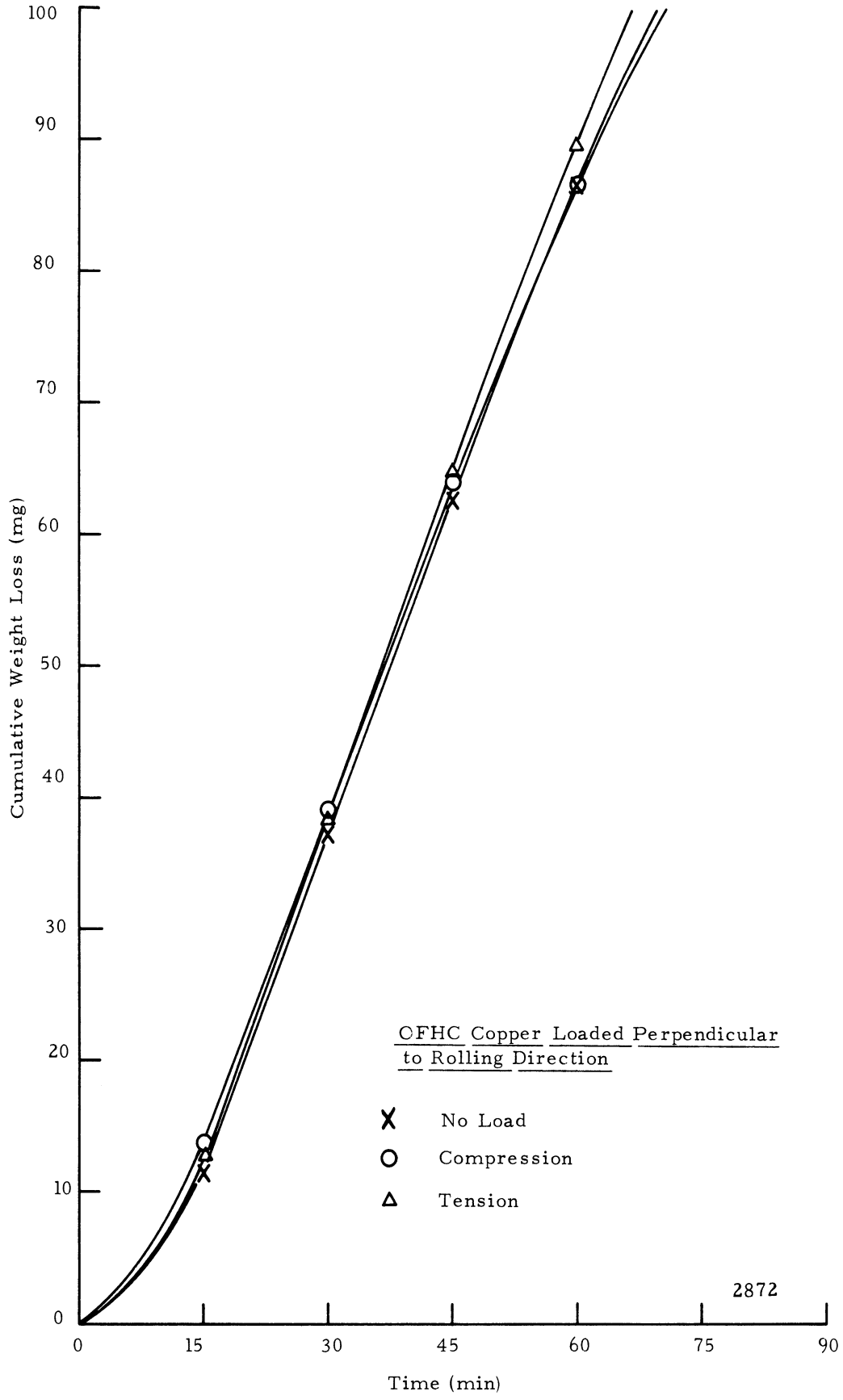

Fig. 72. Effect of External Stress Applied Perpendicular to the Rolling Direction on Cumulative Damage of OFHC Copper

To more closely examine the effect of changing the rolling direction on the fabricated samples the damage curves for tensile loading, Fig. 73 , and those for compressive stress, Fig. 74 were plotted on separate graphs. Fig. 73 shows that the effect of rolling direction on damage rate or on total amount of damage for applied tensile load was very small (1.2%), with the higher rate for the parallel rolling direction.

The effect of rolling direction on the damage rate of the compressive group was slightly greater (Fig. 74). The effect of the parallel direction was to increase the damage rate by 4.27% over that for the compressive load.

Fig. 75 is a composite graph of the data acquired in the third phase of the copper test program. This data was generated while the test specimens were in states of compression and tension at a level of 1.5 times the yield strength of the material. The total damage was very nearly identical for both compression and tension, and varied only slightly from the control group. The 150% yield applied tensile stress increased the damage rate by 2.17%, while the over-compression (i.e. 150% Y.S.) increased the damage rate by only 0.35%. These rate increases are both in the same direction as those tested at 75% of the yield strength; however, the rate changes are somewhat lower. To evaluate the relative effectiveness of these stress levels, plots were made of the data from both the 75% and 150% tests for compression, Fig. 76 and tension, Fig. 77 . Fig. 76 (compressive stress) shows that the major difference occurs in the first 15 minutes of the test, during which period the specimen under twice the compressive load damages 29.4% less than that group under the standard load.

The effect of the increased tensile stress(Fig. 77) was much the same as that of the increased compressive load in that it showed more damage in the beginning of the test and a decreased rate in the constant rate period. The decrease in damage in the first 15 minutes was about 23.6%. The decrease in rate was much less substantial (0.19%).

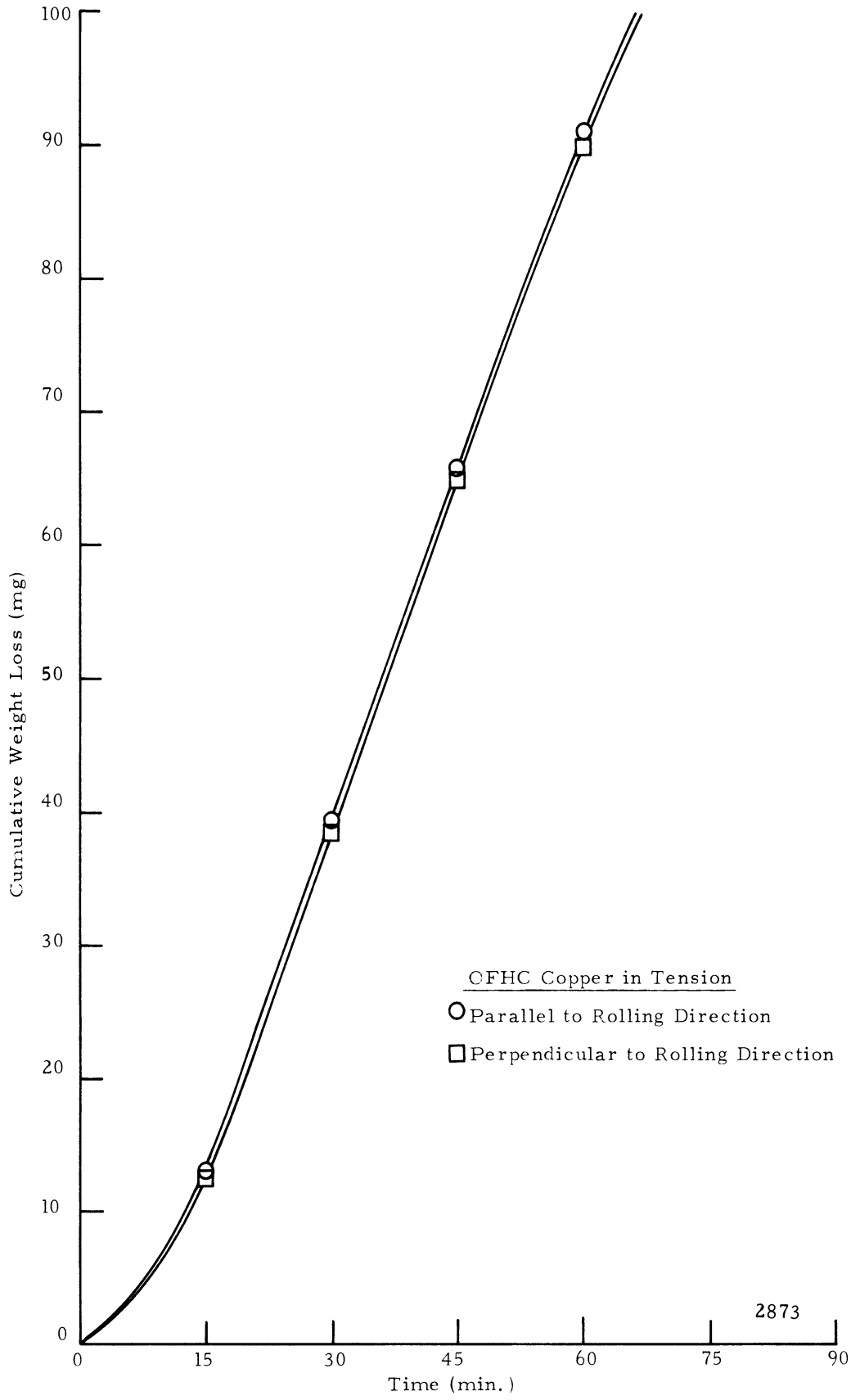

Fig. 73. Effect of the Orientation of External Tensile Stress with Respect to Rolling Direction on Cumulative Damage of OFHC Copper

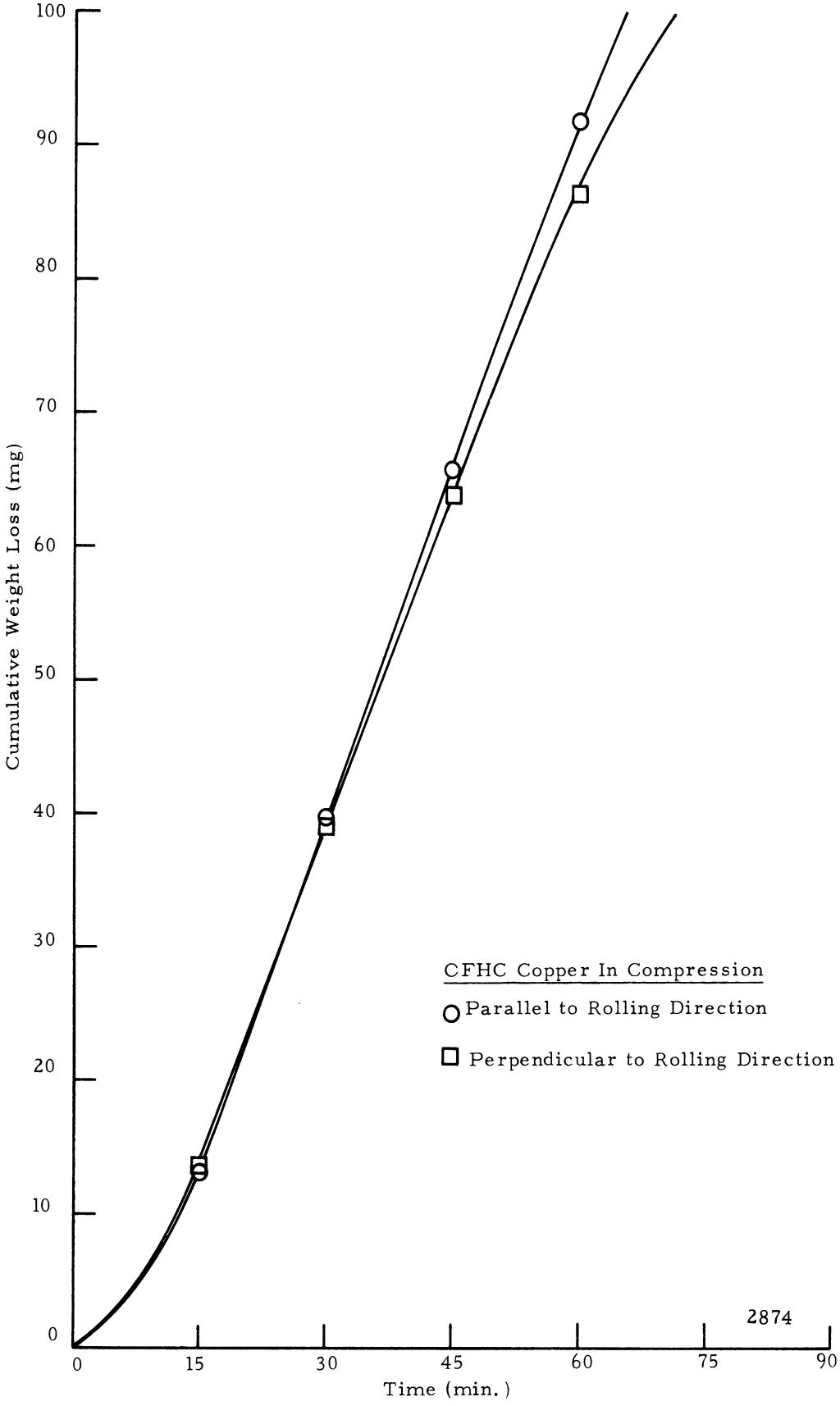

Fig. 74. Effect of the Orientation of External Compressive Stress with Respect to Rolling Direction on Cumulative Damage of OFHC Copper

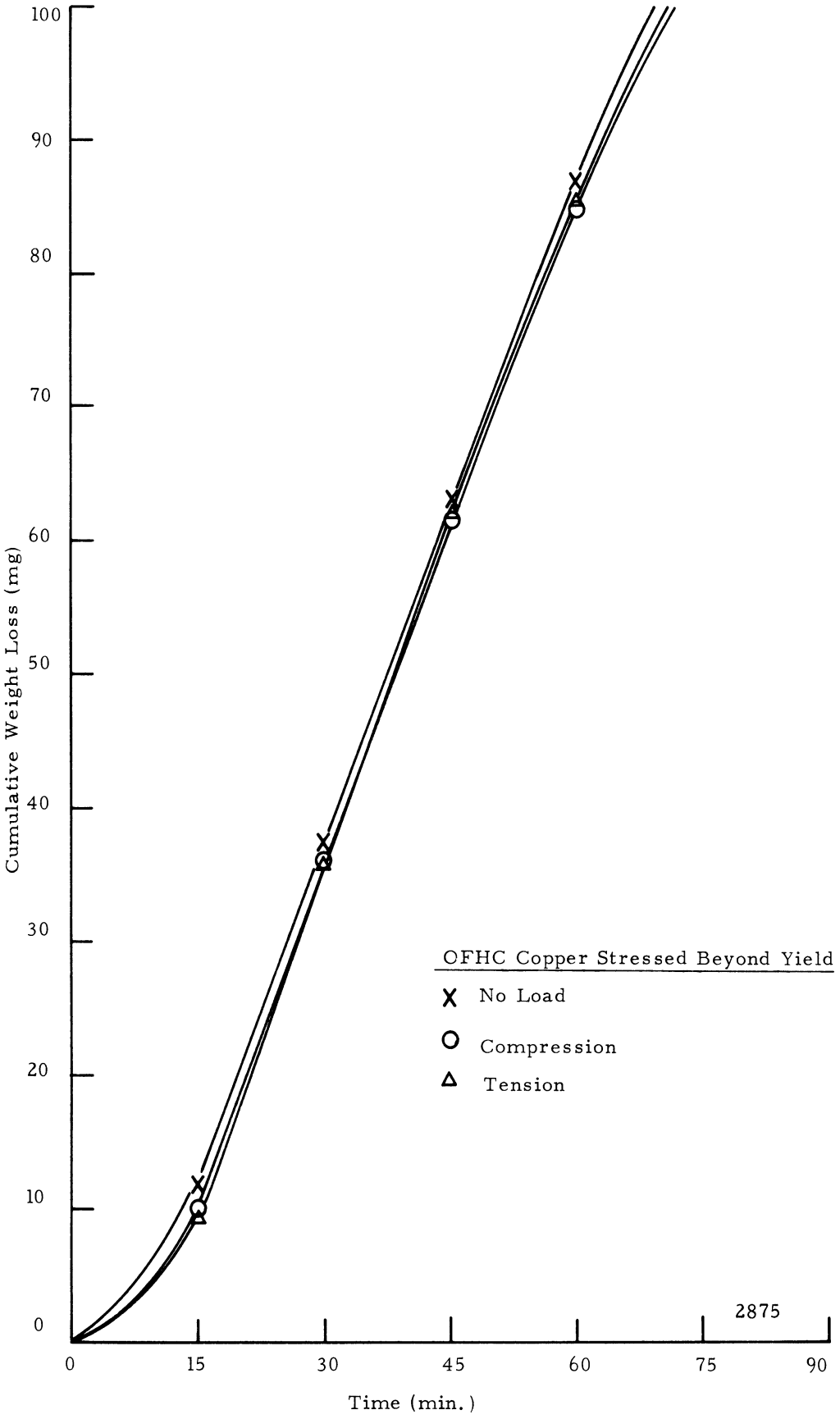

Fig. 75. Effect of External Stresses of 150% YieldStrength on Cumulative Damage of OFHC Copper

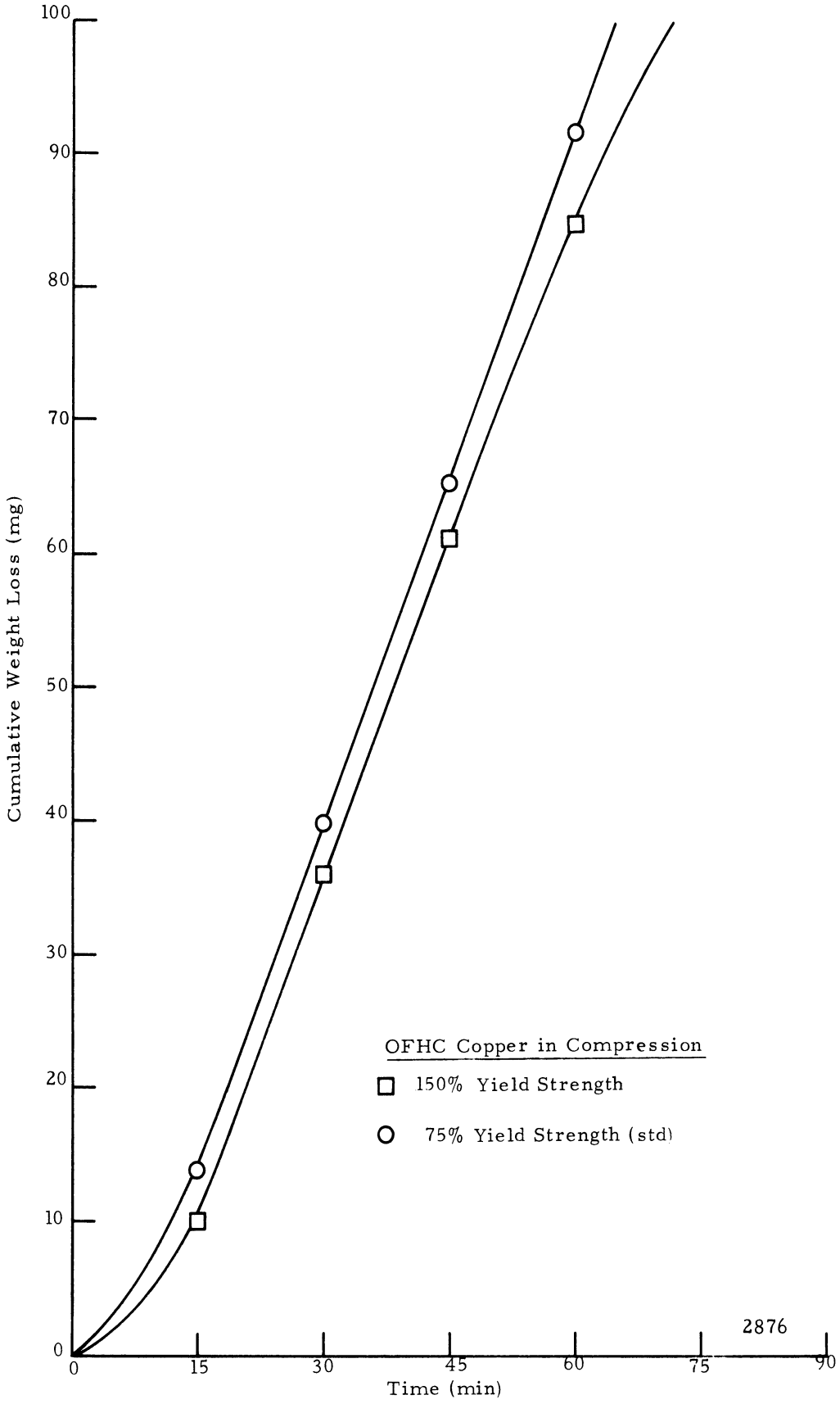

Fig. 76. Effect of External Compressive Stress Level on Cumulative Damage of OFHC Copper

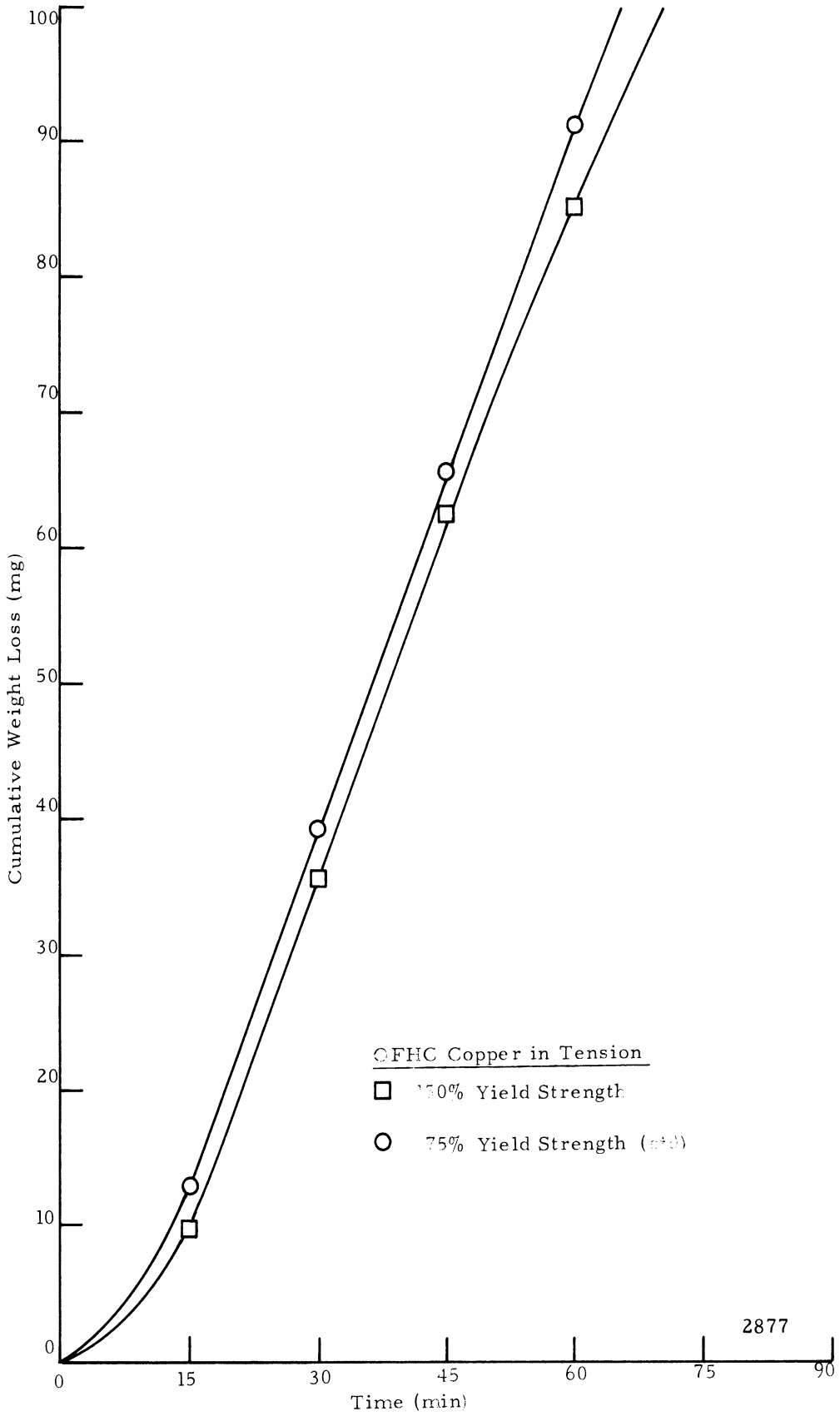

Fig. 77. Effect of External Tensile Stress Level on Cumulative Damage of OFHC Copper

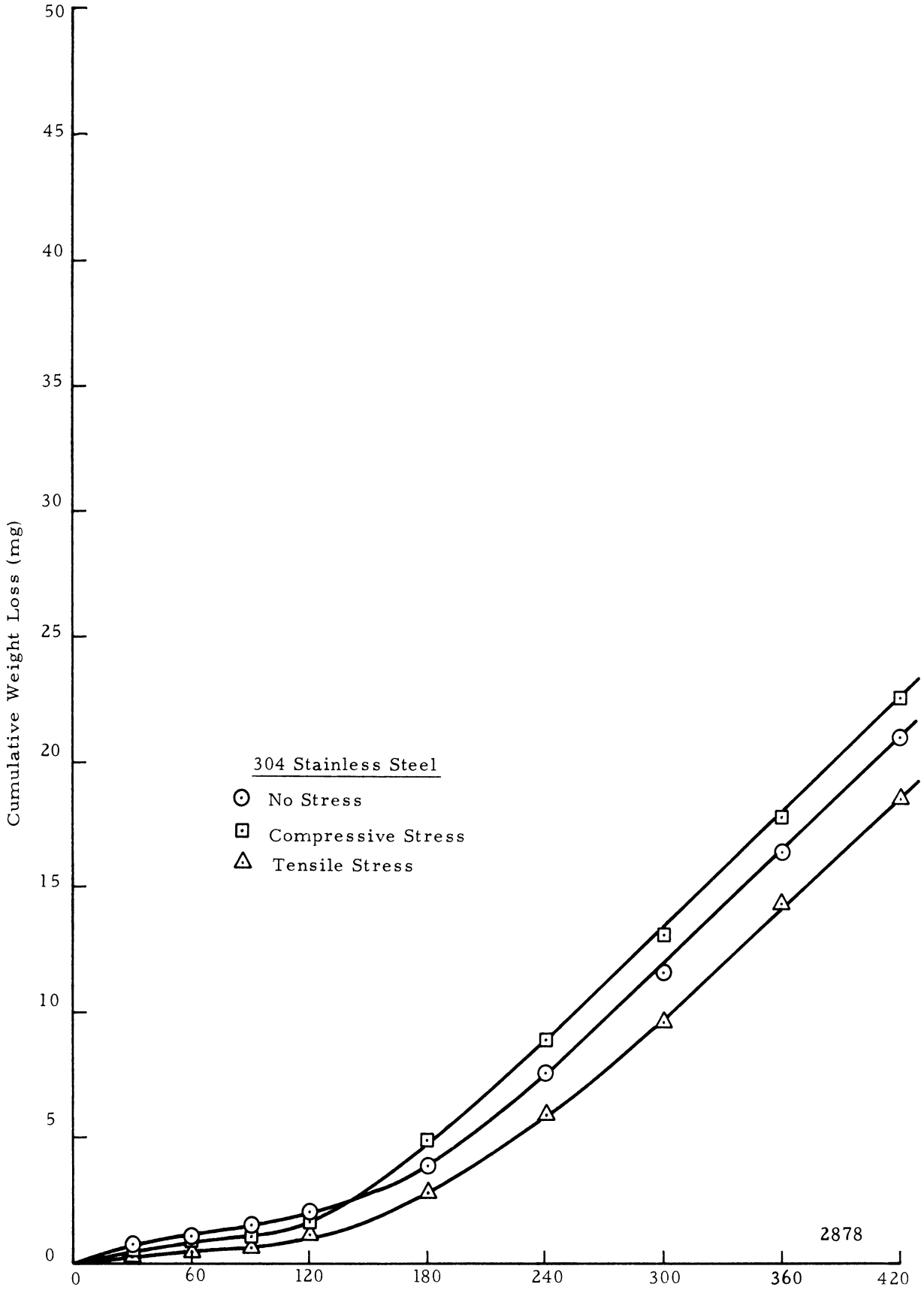

Fig. 78. Effect of External Stress on Cumulative Damage of 304 Stainless Steel

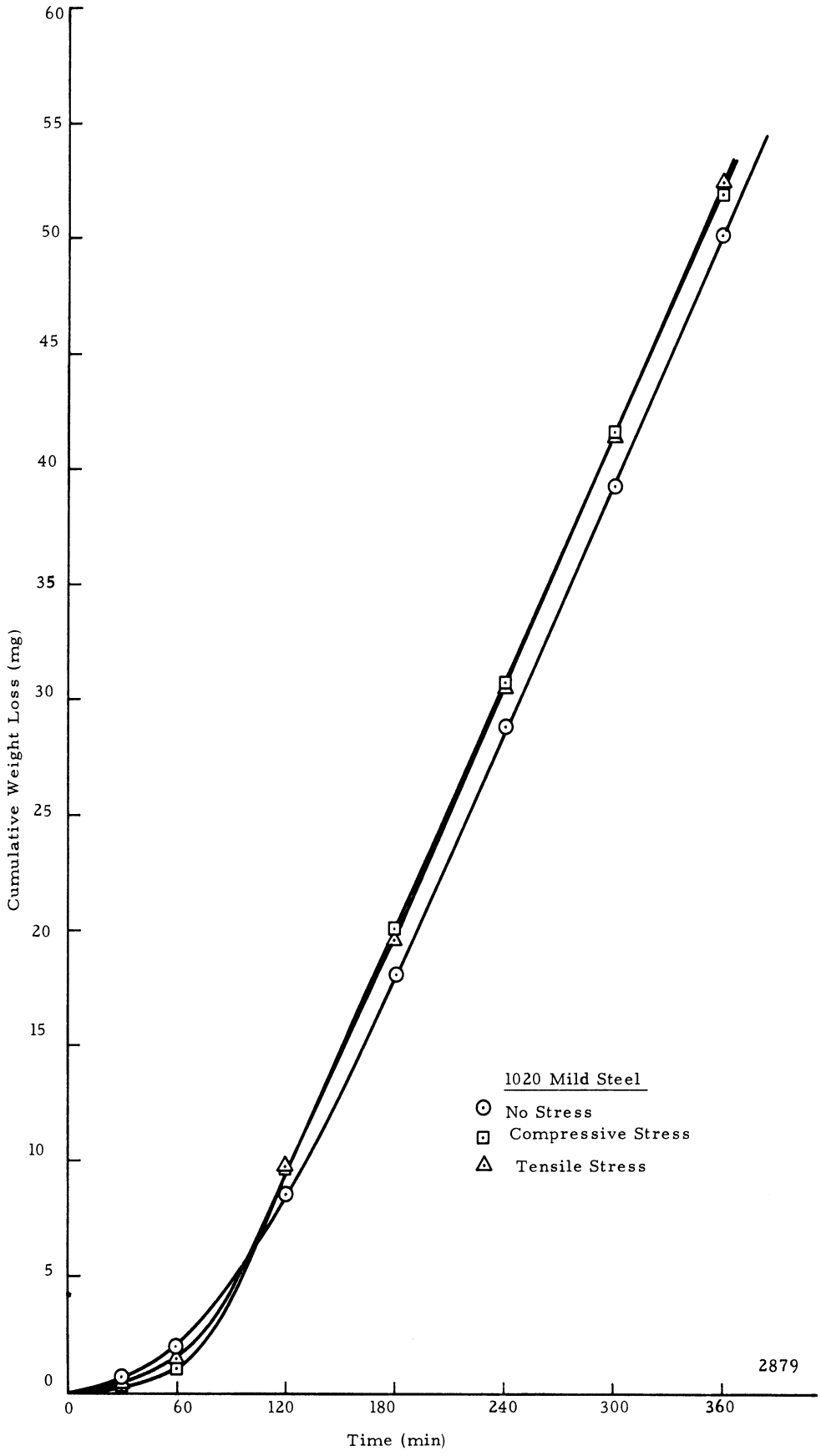

Fig. 79. Effect of External Stress on Cumulative Damage of 1020 Mild Steel

5.) 304 Stainless Steel

304 Stainless steel is unique in showing a decreased rate of damage when the specimens are tested under an applied tensile load (Fig. 78). The effect of the compressive stress was to increase the amount of damage. This reversal from the usual pattern was also seen in some of the other materials. The decrease in rate under tension was about 2.4% compared to the no-load condition. The rate for the compression specimens was 1.4% greater than for the non-stressed tests and about 3.8% greater than for the tensile-loaded test. During the incubation period the average weight loss while tested in compressive was less than for the non-stressed state. For longer periods the damage to the compressively loaded specimens became greater overall than that in the other stress modes. No explanation is apparent for the unusual behavior under a tensile load.

6.) 1020 Mild Steel

One of the program objectives was to evaluate the effect of different metal structures under an applied force on cavitation damage resistance. The 1020 steel was chosen because of its B. C. C. (Body Centered Cubic) structure and its general availability. However, its susceptibility to corrosion is a possible problem. After tests of several hours, corrosion was found, however, to be very small. Only slight discoloration was found after 3 to 4 hours of exposure.

The test results shown (Fig. 79) show a comparatively short initial low rate period, with a rapid increase in rate taking place within a test duration of 30 to 40 minutes. Initial damage showed a lower average rate for the applied tensile load and a much larger average weight loss for the specimens under compressive load. This difference amounted to 82%, i.e., the specimens tested under a compressive stress showed an average weight loss for the first thirty minute period 82% greater than those tested while in tension, and 71% greater than for the control group. The proportionate difference decreased as the total test duration

was extended to a total of two hours after which the average weight loss for the compressive group was 12% greater than that for the group with the applied tension, and 25% greater than for the control group.

As for the other materials, the damage rates stabilized after the incubation period. A constant rate occurred after a test duration of 120 minutes. The general effect of both tensile and compressive stress was to increase the stabilized damage rate (4.46% for compression and 3.33% for tension compared to the control specimen). The total test period used in these tests was 6 hours per specimen. No discernable decrease in damage rate was found up to this point, i.e., the damage rate remained constant.

7.) Magnesium Tooling Plate, AZ31B

The magnesium tooling plate was chosen because of its structure; i.e., H.C.P. (hexagonal-close packed). The material was alloyed with aluminum as mentioned in the table of properties, Table II. However, the low aluminum content (3%) was not enough to alter the structure. The damage curves for this material are shown in Fig. 80. The incubation period was not as long as with some of the other materials (stainless steel, e.g.) but was much like the copper. There was, however, a low inital damage rate period as shown. The rate of damage was considerably higher for the applied tensile load than for either the compressive load or for zero stress. The rates of damage were relatively (12.95%) higher than for the no-force condition for the applied tensile load, and 13.77% lower than the no-force condition for the applied compressive load. The above differences were larger than were found for most of the other materials, particularly the spread between tension and compression (26.7%).

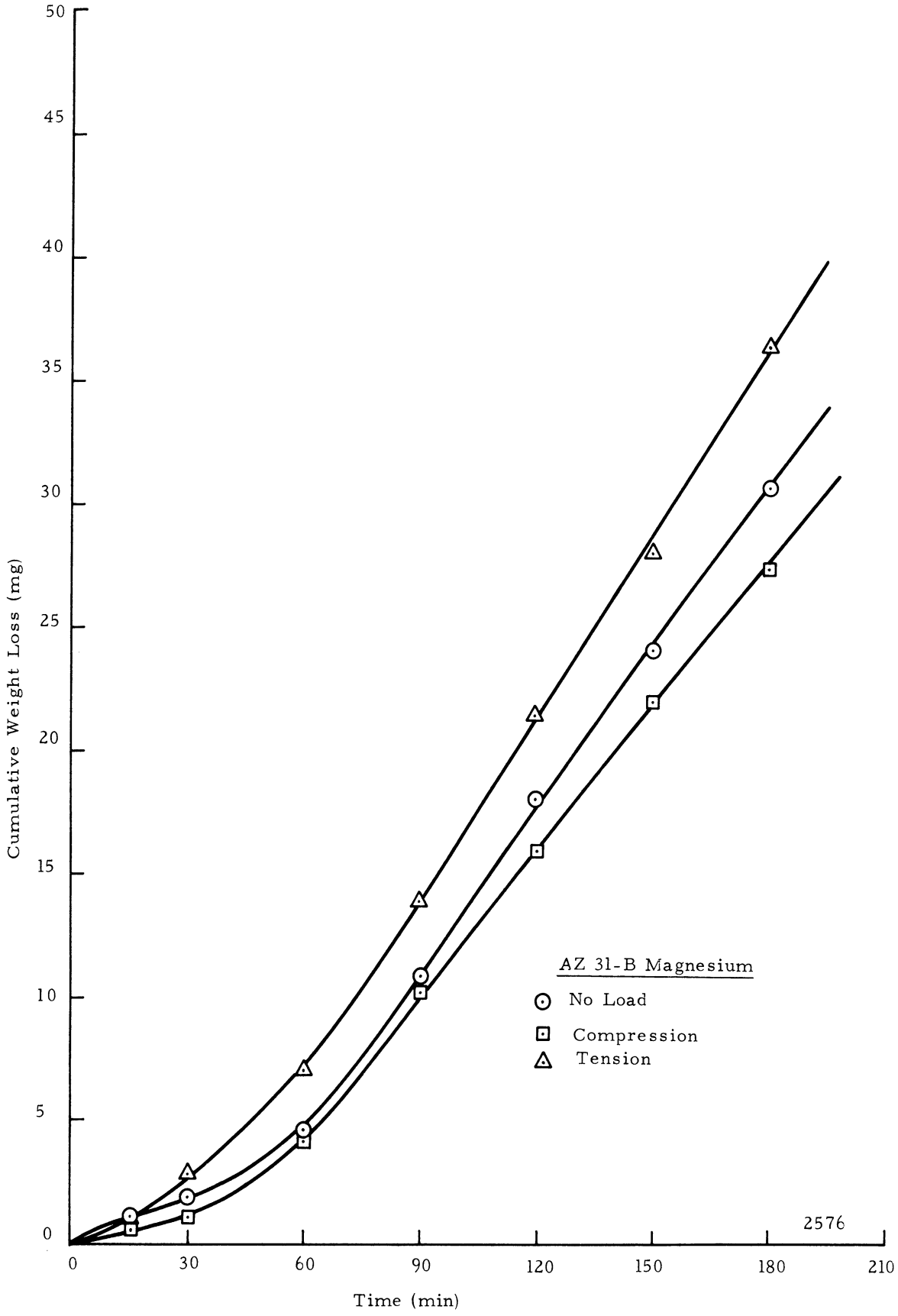

Fig. 80. Effect of External Stress on Cumulative Damage of Magnesium Tooling Plate, AZ 31B

b. Effect of Damage on the Tensile Properties

Previous work in this laboratory on the stress effect (2) indicated the possibility of microcracks emanating from the bottom of the cavitation pits. This supposition was based on an observed additional decrease in yield and tensile strength for materials damaged by cavitation while under tension as compared to specimens damaged under zero load. Such microcracks would act as stress raisers in addition to reducing the remaining cross section. To determine if there was such an effect and whether it was altered by the applied stress during cavitation, a study with copper and aluminum specimens was undertaken.

In the cavitation tests already described the specimens after damage had a mean decrease in cross section of 3-4%. This difference was not sufficient to define differences in breaking strength between the damaged and non-damaged specimens due to stress condition during the cavitation test. Various steps were taken, therefore, to provide a greater percentage decrease in cross sectional area due to cavitation damage.

The proficorder traces had indicated that the overall damage pattern was fairly uniform across the damaged portion of the specimen. Thus, the overall damage depth (MDP) becomes meaningful.

$$\text{MDP} = \frac{W}{\rho A}$$

where W = weight loss in milligrams

ρ = density in milligrams per cubic inch

A = damage area over which weight loss occurs, assuming uniform loss across the entire damaged area

MDP, therefore, represents a volume loss per unit area or an equivalent damage depth. The specimens to be tested for tensile properties were consequently run to an increased damage

equivalent MDP = 0.015 $\pm$ .001 in., which was adequate to give reasonable statistical validity to the later breaking tests. To assist the statistical situation, the overall cross sectional area of the specimens in the damage region was reduced after the initial damage tests had been completed. The specimens were then recut to a width of 0.550 $\pm$ .001 in. so that the damaged region extended almost all the way across the surface. Fig.81 shows the relative specimen sizes prior to and after cutting. Fig. 82 is a close up view of the damage area after the width of the specimen had been reduced as described.

The materials tested were copper and aluminum. The copper specimens were chosen to have a rolling direction parallel to the direction of the applied force while the aluminum specimens were rolled both perpendicular and parallel. Tables V, VI, and VII show the results of these tests. Table VII shows the decrease in cross sectional area, $\Delta\%A$, due to cavitation damage. As an example, for the copper specimen with no applied force there was a decrease in cross-sectional area, $\Delta\%A$, of 9.02%, whereas the yield strength, $\Delta\%Y.S.$, decreased by 19.43%. The tensile strength, $\Delta\%T.S.$, was decreased 14.07%. These effects were the largest found. For the specimen run under tensile stress, the decrease in cross-sectional area, $\Delta\%A$, was 8.92%, the decrease in yield stress was 15.6%, and that in tensile strength, 12.98%. The specimen tested while under a compressive load shows an area decrease of 8.6%, a 15.96% decrease in yield strength, and a 12.98% decrease in tensile strength. Since the decrease in areas were not quite the same for these three cases, a relative rating number was used to allow a direct comparison of the data. The relative rating numbers shown in Table VII (Y.S.# and T.S.#) were calculated by dividing the percentage decrease in yield strength,

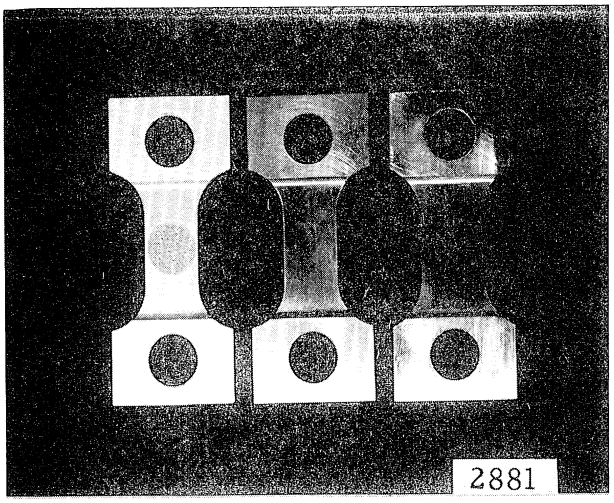

Fig. 81. Photograph of Tension-Compression Specimens Before and After Cutting for Reduced Cross Section Tensile Test

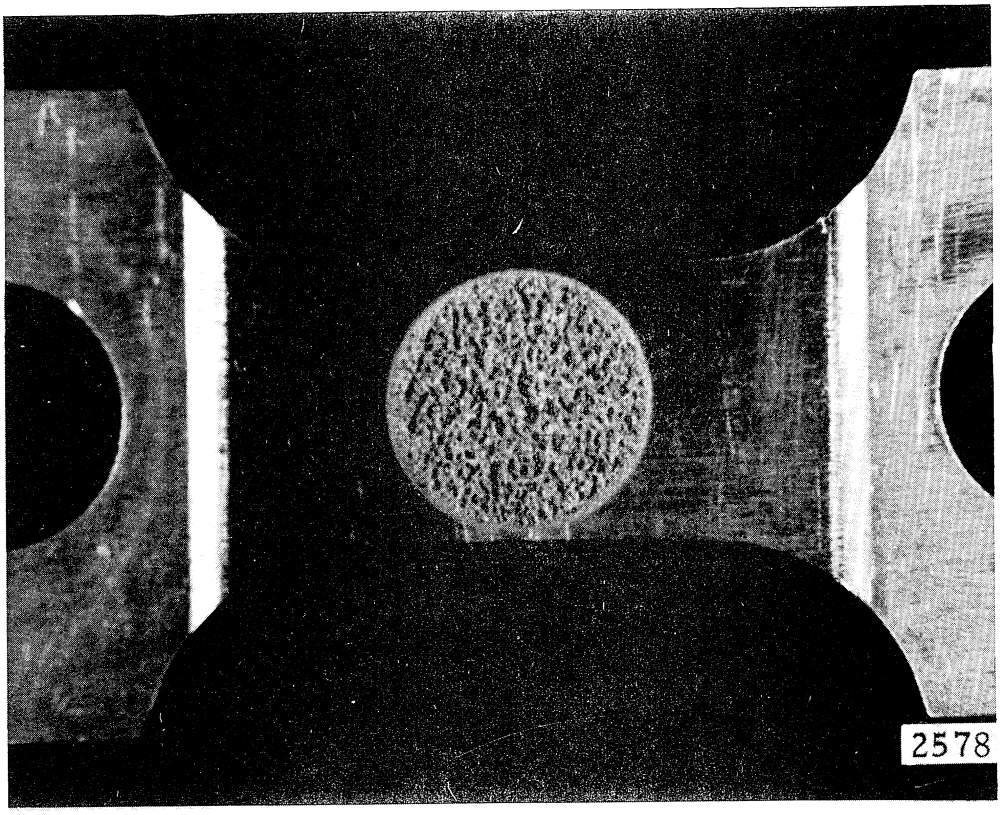

Fig. 82. Center Damage Area of a Specimen with a Reduced Cross Section Prior to Tensile Pull

TABLE V

Tensile Properties of Damaged Specimens

Material-Description	Yield Strength**	Tensile Strength	Ultimate Strength*	$\frac{Y_s}{Y_o}(100)$ %	$\frac{T_s}{T_o}(100)$ %
Copper-Control ⊥ Grain	23250	32702	47508		
-Control ∥ Grain	28200	33345	48114		
Damaged-NoForce ∥ Grain	22720	28656	20595	80.57	85.93
Damaged-Tensile Force ∥ Grain	23800	29014	24365	84.40	87.01
Damaged-Compressive Force ∥ Grain	23700	29012	34505	84.04	87.01
Aluminum-Control ⊥ Grain	6775	15296	15525		
Damaged-No Force ⊥ Grain	6500	13411	18105	95.94	87.68
Damaged-Tensile Force ⊥ Grain	7500	13423		110.70	87.75
Damaged-Compressive Force ⊥ Grain	6075	13038	19515	89.67	85.24
Aluminum-Control ∥ Grain	6775	15864	14472		
Damaged-No Force ∥ Grain	5950	14288	13860	87.82	90.01
Damaged-Tensile Force ∥ Grain	7180	14368	12962	105.98	90.57
Damaged-Compressive Force ∥ Grain	6500	14390	15343	95.94	90.71

* Since Ultimate Strength is based on the measured area after break, it is felt that this figure it not significant due to large errors occurring in measuring.

** Yield Strength represents the value for 0.2% offset yield stress.

TABLE VI

Area and Volume Losses of Damaged Specimens

Material-Description	A_o - Original x Sect. Area	W_L - Total weight loss	V_L - Volume loss A_o/ρ **	D_L - Equivalent damage depth	A_L * - Lost Equivalent x Sect.
Copper-Control ∥ Grain	.08472				
Damaged-No Force ∥ Grain	.08388	434.3 mg	.00297	.01514	.00754
Damaged-Tensile Force ∥ Grain	.08375	428.5	.00293	.0149	.00747
Damaged-Compressive Force ∥ Grain	.08411	414.3	.00284	.0144	.0722
Aluminum-Control ⊥ Grain	.08369				
Damaged-No Force ⊥ Grain	.08872	139.69	.00311	.0158	.00792
Damaged-Tensile Force ⊥ Grain	.08865	141.80	.00316	.0161	.00805
Damaged-Compressive Force ⊥ Grain	.08899	140.2	.00312	.0159	.00795
Aluminum-Control ∥ Grain	.08321				
Damaged-No Force ∥ Grain	.08885	134.81	.0030	.01527	.00764
Damaged-Tensile Force ∥ Grain	.08684	128.76	.00287	.0146	.00733
Damaged-Compressive Force ∥ Grain	.08477	127.02	.00282	.0144	.00719

*A_L = lost equivalent cross section based upon a measured damage diameter of 0.5 inches

**ρ = density of test material

TABLE VII

Calculated Stress Numbers of Damaged Specimens

Material Description	A_p*, residual cross section area	$A=\frac{A_p}{A_o}$	$\Delta\%A=(1-A)(100)$	$\Delta\%$ YS $(1-Y_s/Y_{s_o})$ x100	$\Delta\%$TS $(1-T_s/T_{s_o})$ x 100	YS** # = $\Delta YS/\Delta A$	TS*** # = $\Delta TS/\Delta A$
Copper Control ∥ Grain							
Damaged-No Force ∥ Grain	.0763	.9098	9.02	19.43	14.07	2.15	1.56
Damaged-Tensile Force ∥ Grain	.0763	.9108	8.92	15.60	12.98	1.74	1.45
Damaged-Compressive Force ∥ Grain	.0769	.9142	8.60	15.96	12.98	1.85	1.50
Aluminum-Control ⊥ Grain							
Damaged-No Force ⊥ Grain	.0808	.9107	8.93	4.06	12.32	0.455	1.379
Damaged-Tensile Force ⊥ Grain	.0806	.9092	9.08	-10.70	12.25	-1.182	1.353
Damaged-Compressive Force ⊥ Grain	.0810	.9107	8.93	10.33	14.76	1.155	1.65
Aluminum-Control ∥ Grain							
Damaged-No Force ∥ Grain	.0812	.9140	8.60	12.18	9.99	1.417	1.164
Damaged-Tensile Force ∥ Grain	.0795	.9155	8.45	-5.98	9.43	-0.696	1.10
Damaged-Compressive Force ∥ Grain	.0776	.9152	8.48	4.06	9.29	0.480	1.10

A_p* = Residual Cross Sectional Area = $A_o - A_L$

**YS # = Yield Stress Number

***TS # = Tensile Stress Number

Δ%Y.S., or tensile strength, Δ%T.S., as the case may be, by the percentage decrease in cross sectional area, Δ%A. This gives a value of 1 for a change equivalent to the change which would be expected if the only effect of the damage was a uniform decrease in cross-sectional area.

Using this criteria the largest relative strength reductions were those for the zero-force specimens. The samples for applied compressive stress showed a slightly greater effect than the tensile stress specimens. In each case the greatest effect was in the yield strength. This may indicate the formation of microcracks under the damage. The reduced decrease in tensile strength may be attributable to the fact that micro-effects are probably of less effect in determining breaking strength than yield strength.

The effects of damage on the tensile properties of the specimens (aluminum) having their central axis perpendicular to the rolling direction will be considered next. Table VII shows the relative decrease in area of these specimens. The greatest effect upon yield strength was 10.7% increase (Table VII). This increase is probably the result of strain hardening in the annealed aluminum due to the applied tensile stress. This hypothesis is strengthened by the fact that there was a decrease in yield stress for the sample which was run with no applied stress. However, it was not as great as would be expected from the decrease in cross-sectional area, indicating apparently the effect of cold work from the cavitation damage itself. The specimen tested under applied compressive stress did show a definite decrease in yield stress above and beyond that which could be due to just a decrease in effective cross sectional area. This effect was in the range of 15% greater than expected, indicating

that for this material the deleterious effect of cavitation damage is increased by pre-compression. We may then postulate that for this material the cavitation damage may be primarily due to tensile failure since pre-compression would then increase the maximum difference between principal stresses.

In all cases with aluminum the tensile strength (not yield strength, which is more senstive to cold work) of the material was decreased to a greater extent than anticipated on the basis of area reduction. This may be partially attributed to the effect of microcracks as stress raisers.

For aluminum with rolling direction parallel to the direction of the applied tensile load, the same general trend is visible. For the compressive condition, however, the yield stress increased after cavitation.

Comparison of copper with aluminum indicates that approximately the same degradation in tensile strength occurs for both materials. The sometimes inverse effects on yield strength have been discussed. This seems to indicate less stress hardening of the copper than of the aluminum.

c. Metallurgical Examination of Damaged Specimens

Samples for sectioning were prepared following standard metallurgical practices. A cut-off wheel was used to provide both a transverse and longitudinal section, as shown in Fig. 83.

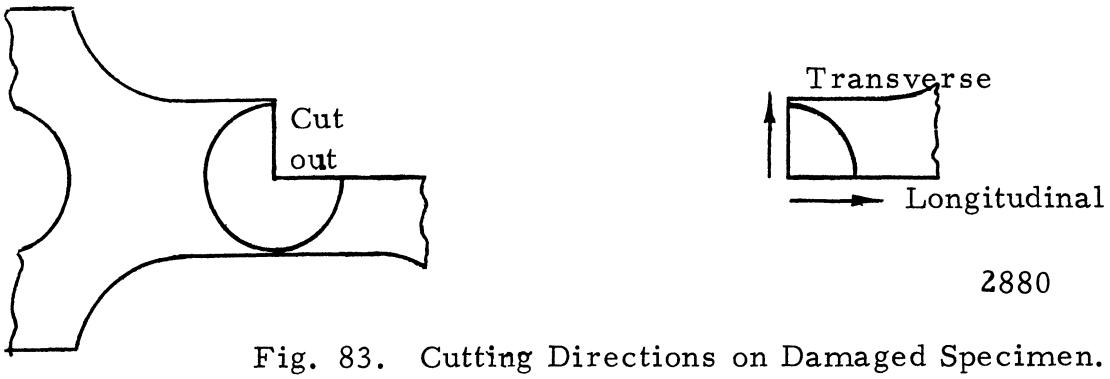

Fig. 83. Cutting Directions on Damaged Specimen.

The samples were then mounted in clear plastic boat resin to expose the surfaces indicated by arrows (Fig.83). They were then polished on successively finer grit sand papers, with final polishing being completed on 6 micron and 1 micron diamond-imbedded polishing wheels to minimize edge distortion and rounding.

When the final polish on the 1 micron diamond was completed the samples were etched, examined, re-polished and re-etched until visual examination showed the removal of all traces of cold work from the original cutting and polishing operations. Finally the samples were photographed at 400 diameters. This magnification was chosen to best show the relative attack on each sample and still detect any slip lines near the damaged surface.

Fig. 84 shows four photographs of a damaged SAE 660 specimen. Photographs A and B are taken in a transverse direction to the specimen while C and D are taken in the longitudinal direction. The apparent holes in the sample are porosity in this cast material. The specimen (Fig. 84) had been tested under zero applied load. In the transverse direction only a few cracks are visible. Slip lines, however, can be seen in photograph A at the base of the pit on the top right. Slip lines are also visible in photographs B, C, and D. These indicate that the material just adjacent to the pits has experienced some amount of cold work. In photographs A and B the slip lines appear almost perpendicular to the pit apex.

The longitudinal photographs show some evidence of micro cracks at the base of the pits. In the center of photograph D a large pit has at its apex a number of microcracks emanating in different direction. There is also evidence of slip lines on either side of the pitted region, and particularly to the right of the apex. The concentration of slip lines in this area would indicated that considerable cold work was done in this region. Fig. 85 shows two sets of photomicrographs taken also of other samples of SAE 660.

A
Transverse

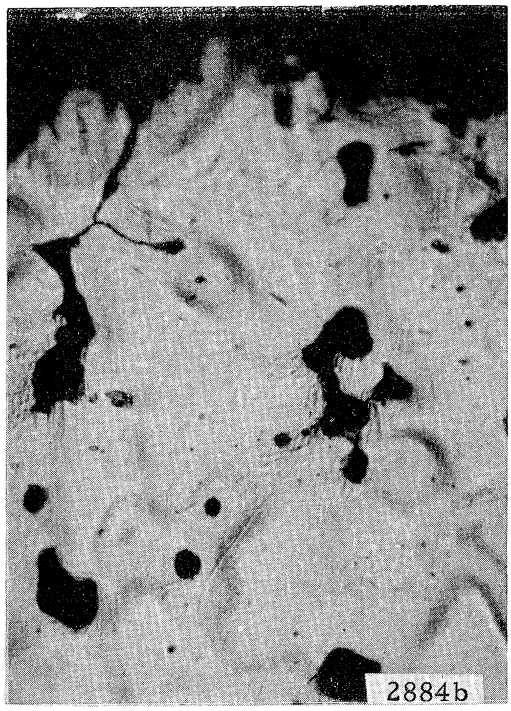

B
Transverse

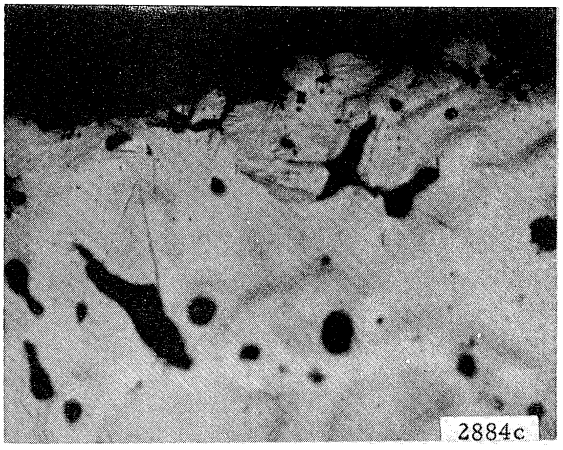

C
Longitudinal

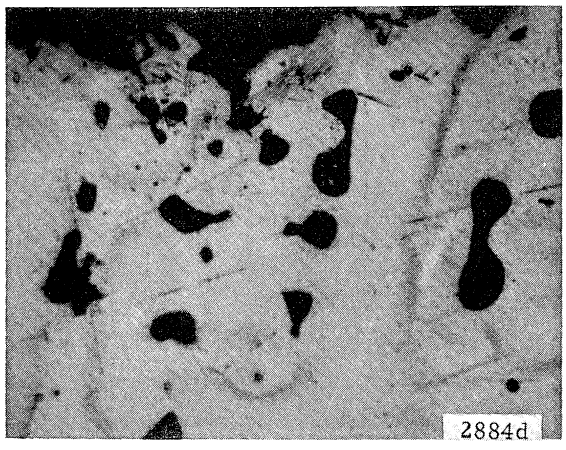

D
Longitudinal

Fig. 84. Photomicrographs of Cavitation Damage Area of a No Load SAE 660 Close Proximity Specimen (400x)

A
Compression-Longitudinal

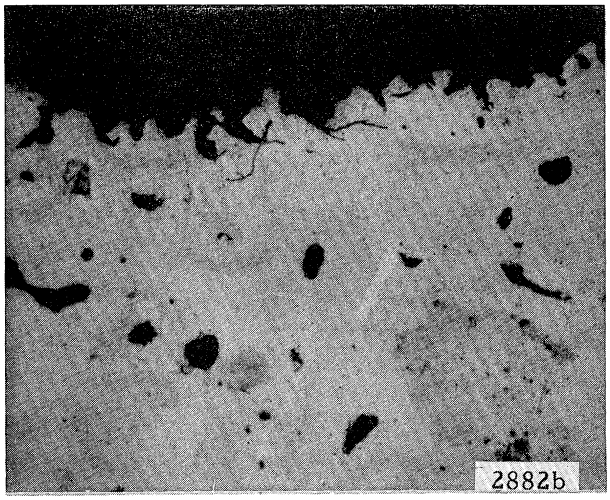

B
Compression-Transverse

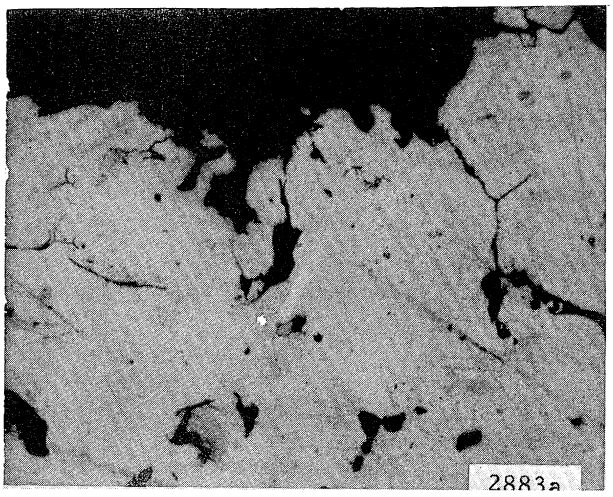

C
Tension-Transverse

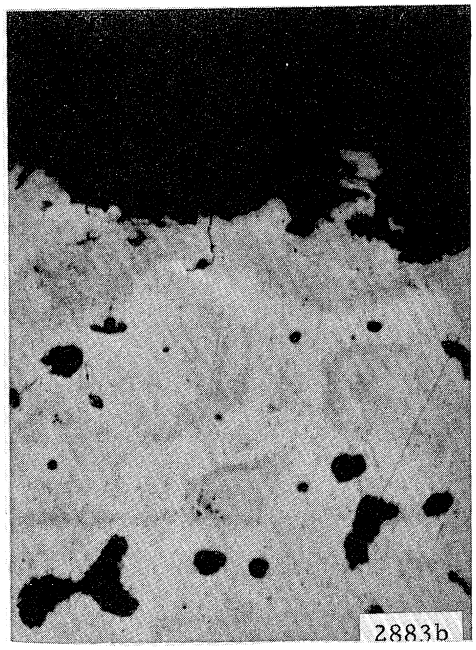

D
Tension-Longitudinal

Fig. 85. Photomicrographs of Cavitation Damage Area of Tension and Compression SAE 660 Close Proximity Specimens (400x)

Photographs A and B are of a specimen tested with applied compressive load. Photograph A is longitudinal and B transverse to the sample. Photograph C is a transverse picture of a SAE 660 specimen tested under tensile load and photograph D is a longitudinal picture of the same specimen. In both stress modes the longitudinal pictures show the microcracks running vertically to the surface and the transverse pictures show the micro-cracks angled off from the pitted surface. None of these photos show slip lines. There is no apparent difference between specimens tested under compressive or tensile load. In each case microcracks are definitely present in the area of the pit apex.

Fig. 86 , photos A and B show a copper specimen damaged with zero applied force, and C and D a copper specimen damaged under tensile load. In A and B there appears to be no difference between the transverse direction (A) and the longitudinal direction (B). There are however, a few small microcracks at or near the apex of the damage pits. There are no discernable slip lines in these photographs, perhaps indicating little or no work hardening of the damaged surface.

Photos C and D also show no slip lines. However, both the transverse (C) and the longitudinal (D) direction show larger more prominent microcracks emanating from the base of the damage pits. As for the SAE660, the cracks in the longitudinal direction appear to come away from the pits at an angle almost perpendicular to the centerline of the pit.

Fig. 87 shows both the transverse (A) and the longitudinal (B) directions of a copper specimen cavitated in compression. Close examination of the photographs shows a number of microcracks at the base of the damage pits. These seem to start at the very apex of the pit and continue until they intersect a grain boundry, at which point

A
No Force - Transverse

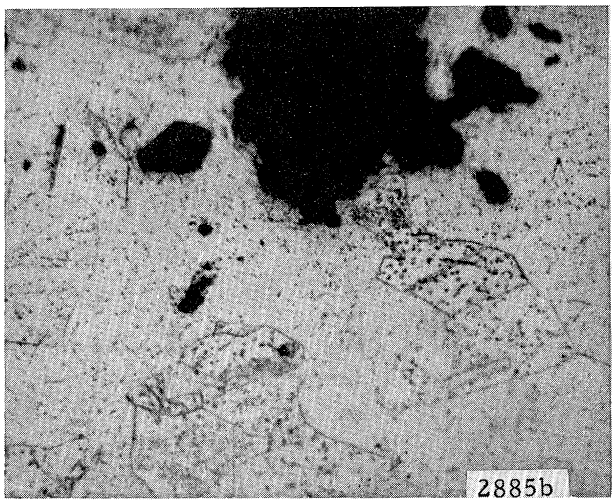

B
No Force - Longitudinal

C
Tension - Transverse

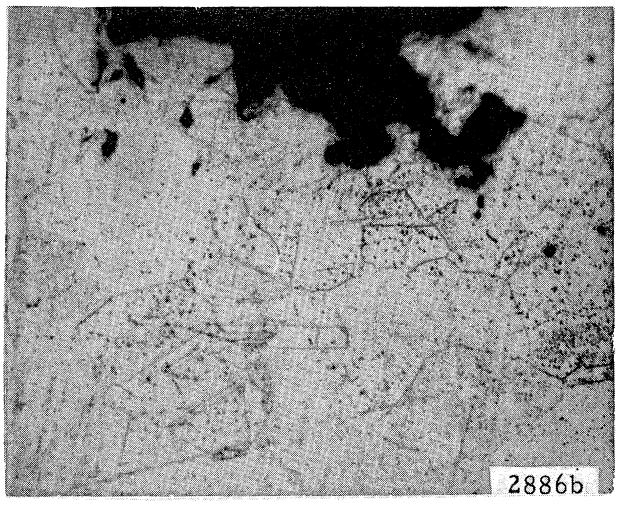

D
Tension - Longitudinal

Fig. 86. Photomicrographs of Cavitation Damage Area of No Load and Tension CFHC Copper Close Proximity Specimens (400x)

A. Transverse

B. Longitudinal

Fig. 87. Photomicrographs of Cavitation Damage Area of Compression OFHC Copper Close Proximity Specimen (400x)

they terminate. The longitudinal picture again shows direction of the cracks perpendicular to the surface.

Photomicrographs were also taken of the the brass. The results were typical of those found for copper. There were, in all cases, microcracks in the region of the damage pits. There were no slip lines, however.

It is evident that damage is accompanied by two possible effects: 1.) microcracks emanating from the base of the damage pits and 2.) cold work or strain hardening depending upon the material just below the damaged surface.

d. Photographic Investigation of Short Duration Damage Tests

It has been mentioned previously that a short duration damage test was run on cylindrical specimens in the mercury venturi. The results of this test (Fig. 20 of Chapter III A. 2b. 3) were very interesting and illuminating with respect to initial damage incurred under the different applied stress situations. Thus it was desirable to determine if the same effects applied to the close-proximity vibratory tests. Thus three brass specimens, of the same lot of material used in this test, were finely ground and then polished to a smooth surface. The specimens were then placed into the tensile compression unit and the same test preparation sequence was used as that for the general damage specimens. The only difference between the damage test with these samples and the general tests already described was the test duration. This was 10 seconds. Fig. 88, 89, and 90 show these specimens after the run. The pictures are 100x and the field is equivalent to 0.112 inches of damage surface.

The entire damage surfaces were examined (with the microscope) and it was found that there was no noticeable concentration of pits in any region. This agrees with the proficorder traces indicating approximately uniform damage across the damage area.

Comparing the three sequences of pictures, the pitting intensity is greatest for the specimen damaged under applied tensile load (Fig. 88). The pits appear to be distributed in size with a large number of small pits and a lesser number of larger pits. The zero load specimen (Fig. 89) shows a larger number of small pits, but the number of large relative to small pits has decreased. The size of the largest pits is still about the same for the tensile load specimens. The compressive specimen (Fig. 90), on the other hand, shows a definite decrease in the number of small and large pits visible on the surface. There are still some larger pits which have about the same diameter as the very large pits of the previous samples.

The major conclusion is that even though the shape and properties of the material as well as the cavitation regime and fluid differed drastically between these tests, the same effects of pre-stress upon pitting size distribution were found. Thus the effect of compression in the beginning of the damage sequence is to decrease the number of pits caused by lower energy impacts. The compressive force does not, of course, totally alleviate the damage as indicated by the long duration runs. Rather it appears to increase the threshold bubble energy for damage, thereby decreasing essentially the number of pits incurred from low energy bubbles, but leaving the surface still as vulnerable to high energy bubbles. Presumably the net effect would be to increase the "incubation period" by compressive pre-load.

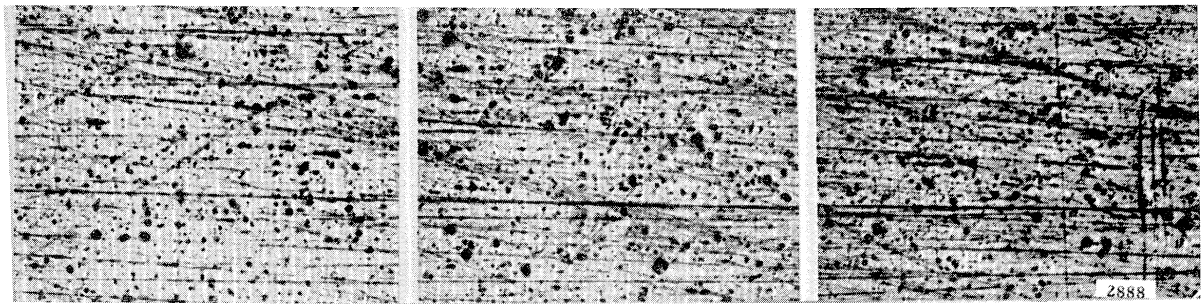

Fig. 88. Cavitation Damage in Tension Brass Close Proximity Specimens after 10 sec. Exposure (100x)

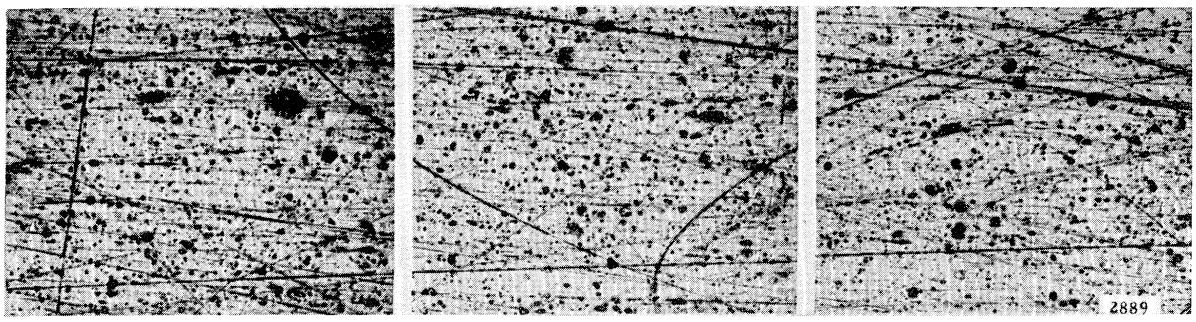

Fig. 89. Cavitation Damage in No Load Brass Close Proximity Specimens after 10 sec. Exposure (100x)

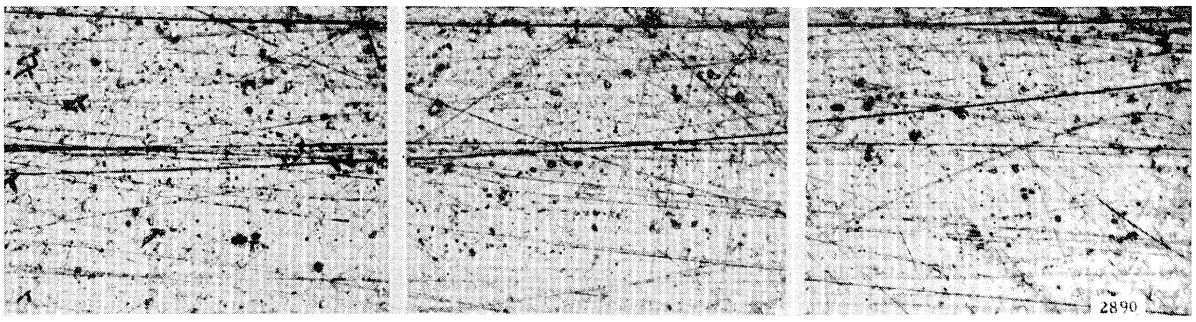

Fig. 90. Cavitation Damage in Compression Brass Close Proximity Specimens after 10 sec. Exposure (100x)

4. Discussion of Results

Table VIII summarizes the data taken for the Face Centered Cubic structure materials (which are listed in decreasing order of damage rate) showing the effect, in all applicable cases, of stress applied parallel to the rolling direction of the material. The rates are calculated from the slopes of the linear portions of the damage versus time curves.

The most heavily damaged material was the 3003-0 aluminum (2.37 mg/min under no load conditions). The copper had the second highest rate (1.708 mg/min). Following in order were brass, SAE660, and 304 stainless steel. The test durations were varied for the various materials to attain the maximum rate portion of the damage curves.

The effects of applied stresses are shown. Applied tensile load, in all cases but 304 stainless steel, increased damage rate by a proportion ranging upward from 3%. The effect of compressive stress was a decrease in rate for all but copper and stainless steel. For copper there was an increase in damage, but the change was not as great as that due to the tensile load. The average change due to compressive load was a decrease of 1.03%. The average change for tensile force was an increase of 5.55%. Thus the difference of averages was 6.58% tensile and compressive loading. Thus for the metals with F. C. C. structure a compressive stress may be beneficial in decreasing cavitation damage.

Table IX shows the compiled data for the specimens with rolling direction perpendicular to the applied stress direction and for aluminum and copper from Table IV to compare the effect of rolling direction. The effect of the applied tensile load is still an increase in damage rate, which is increased by 3.81% when the force direction was perpendicular to the rolling direction in the aluminum and decreased by 1.2% in the comparable copper group. The effect on damage rates for compression was a decrease 4.09% for copper and an increase of 12.53% for the aluminum.

TABLE VIII

Damage Rates for F. C. C. Structure

Material	Damage Rate for No Force	Compression	Tension	$\frac{CR-NFR}{NFR} \times 100$	$\frac{TR-NFR}{NFR} \times 100$
Aluminum	2.369	2.1845	2.518	-7.79	6.29
Copper	1.708	1.735	1.761	1.58	3.10
Brass	0.4099	0.4026	0.4795	-1.78	16.94
SAE 660	0.3754	0.3733	0.3898	-0.56	3.84
304SS	0.07408	0.07510	0.07229	1.38	-2.42

TABLE IX

Damage Rate, Comparison Rolling Direction

Material	Rolling Direction	Damage Rate for No Force	Damage Rate for Compression	Damage Rate for Tension	ΔC%	ΔT%
Aluminum	Perpendicular	2.369	2.458	2.614	4.19	10.34
Aluminum	Parallel	2.369	2.1845	2.518	-7.79	6.29
Copper	Perpendicular	1.708	1.664	1.740	-2.58	1.87
Copper	Parallel	1.708	1.735	1.761	1.58	3.10

The effect of applied stress is thus mixed and dependent on the material when applied perpendicular to the rolling direction. The effects individually are, however, in the same direction for each of the materials. From Table X, the face-centered cubic and the hexagonal-close packed structures show an increased damage rate when tested under tensile load but a decrease under compression. These effects are markedly larger in the HCP than in the FCC structure, differing by about 13%. For the body-centered cubic damage rate increased in both modes of stress.

V. CONCLUSIONS

In the present study three separate systems were used for investigating the effects of externally applied stress on cavitation damage. These were a mercury loop and a water loop, and a stationary vibratory facility using water as a test fluid. The materials studied included 3003-0 Aluminum, O.F.H.C. copper, SAE 660 bearing bronze, 65/35 brass, 304 stainless steel, 1020 carbon steel, and magnesium alloy tooling plate.

A wide variety of supporting investigations were undertaken as preliminary steps to the final objective of this work. The detailed results of all tests have been delineated in the appropriate sections of this report. A summary of the pertinent findings and conclusions follow:

A. Flow and Damage Investigation

The cavitation damage rate on a cylindrical pin type specimen positioned across the diffuser of a venturi was found to be highly dependent upon the mean stream velocity of the fluid and the cavitation condition. The rate maximized at a specific venturi pressure drop for a given throat velocity. The cavitation condition producing maximum damage rate requires that there be numerous bubbles and that these collapse near the surface of the specimen with

TABLE X

Damage Rate Comparison - Structure

Material	Structure	Damage Rate for No Force	Compression	Tension	ΔC%	ΔT%
Group	F. C. C.				-1.03*	5.55*
1020 Steel	B. C. C.	0.1772	0.1843	0.1831	4.46	3.33
Magnesium	H. C. P.	0.2186	0.1885	0.2469	-13.77	12.95

*Average Values

high intensity. The optimum attainment of these conditions is very sensitive to the setting of velocity and pressure levels.

The location of the most damaged area of the cylindrical specimens is at about 80^{o} from the upstream axial centerline. This position does not change with flow rate or pressure drop across the venturi. The location of this high damage region corresponds to an area just up stream of the lowest static pressure region.

There are five principle damage areas on the pin specimens. As an angular progression is made from the upstream axial centerline the following areas can be seen:

1.) $78\text{-}80^{o}$, start of the cavitation damage region
2.) $80\text{-}110^{o}$, high pit concentration area, with greatest concentration near 80^{o}
3.) $115\text{-}130^{o}$, relatively sparsely pitted region
4.) $130\text{-}145^{o}$, second highest pitting density region
5.) $165\text{-}180^{o}$, area of no damage

High speed photographs taken in the water loop indicated that these damage areas corresponded to areas where the cavitation cloud in its oscillations came in contact with the surface of the specimen. The photographs showed a definite lateral oscillation of the cavitation cloud. Vapor clouds were shed at an estimated frequency of 1.935×10^{3}/ second, at a Reynolds number of approximately 5×10^{5} corresponding to the estimated laminar to turbulent boundary layer transition for the cylinder. The Strouhal number for this shedding frequency is 0.632.

Using a cadmium-plated stainless steel cylindrical specimen, impact craters were obtained providing strong supporting evidence to the jet impingement theory of cavitation damage. Circular pits were formed as if by the "washing out" of the plating material.

Pressure measurements indicated that the minimum pressure on the pin occurs at $78\text{-}80^{o}$ from the upstream axial centerline. As the length of the cavitation cloud is increased, the pressure decreases from the 80^{o} point until it reaches a uniform low value over the entire back side of the pin. When the length of the cloud is greater than about 1/2 inch,

(for the 1/4 in. dia. pin) further increases in length, by decreasing the downstream pressure, has no effect on the pin-wall pressure in the 80-180° region.

B. Vibratory Facility Investigations

A system for stressed tests using a vibratory horn oscillating in close proximity to a metallic surface was developed. For a 2 mil double amplitude at 20 kHz the damage rate was shown to maximize for a horn-specimen clearance between 0.018 and 0.024 inches. The damage rates for this close proximity test are somewhat lower than those for a conventional vibratory horn test. This method, however, did make possible the damage testing of specimens in different pre-stress modes.

The damage areas of both the horn tip attachment and the specimens were scanned using a Bendix proficorder. The specimen damage was relatively uniform as a function of radius. The horn tip attachments showed increased damage near the outer edge.

High speed motion pictures of the fluid between the horn tip attachment and the specimen surface showed that the bubbles did not collapse totally in certain regions during an individual horn oscillation. The bubbles appeared to move outward with a radial velocity of about 54 feet per second. Using very short test durations, it was found, in both the flowing mercury system and the vibratory water system, that an applied tensile load along the specimen axis increased pitting while a compressive stress decreased it, as compared to a zero-stress specimen. In each case the compressive stress decreased the number of small pits in the initial stage. Approximately the same maximum pit sizes in about the same number regardless of the stress mode. For tensile stress there are more small pits formed in the initial portion of a test.

Metallographic examinations after the long duration tests revealed slip lines and micro cracks at the base of the damage pits. The slip lines indicate cold-work associated with the damage process.

The presence of the micro cracks for copper may also be indicated by the relatively large changes in the yield and tensile strengths of the specimens compared to the change in cross-sectional area after damage testing. Inverse results were obtained for aluminum, indicating that work hardenging due to cavitation overcame the effect of reduced area and micro cracks.

The damage results from the applied stress close proximity tests are summarized in Table XI. Large individual variations occurred in the data, though there were general trends for the overall experiment. The effect of the applied stress was found to be quite substantial, with initial effects on rate often much larger than long term effects. The same observation was made with respect to initial pitting observations.

In general, a compressive load on the specimen inhibits cavitation damage in the early stages and reduces the rate somewhat after it has started. An applied tensile load accelerates damage both in the initial period and later. Numerous findings of this study further support the hypothesized jet impingement theory of cavitation bubble collapse.

Various phases of the foregoing investigation are summarized in references 22, 23, and 24.

TABLE XI

Average and Extreme Damage Rates

A. Rates Measured in Linear Portion of Curve

	Percent Change Compression *	Percent Change Tension **
Maximum Positive	+4.5	+16.9
Maximum Negative	-13.8	-2.4
Algebraic Average	-1.5	+5.8

B. Initial Rate Effects

	Percent Change Compression *	Percent Change Tension * *
Maximum Positive	+56.4	+53.7
Maximum Negative	-51.8	-53.4
Algebraic Average	-4.2	+1.16

* $\frac{\text{Compressive Weight Loss - Zero Load Weight Loss}}{\text{Zero Load Weight Loss}} \times 100$

** Comparable to definition above for tensile weight loss.

REFERENCES

1. Hammitt, F.G., "Damage to Solids Caused by Cavitation", Phil. Trans. Roy. Soc., A, n1110, v.260, pp. 245-255, 1966.

2. Barinka, L.L., Hammitt, F.G., Robinson, M.J., Pehlke, R.D., and Siebert, C.A., "Cavitation Damage Tests of Stressed Specimens with Mercury in a Venturi", ORA Technical Report 03424-13-T, University of Michigan, March 1964.

3. Shal'nev, K.K., Stepanov, R.D., and Kozyrev, S.P., "Effect of the Stressed State of Metals on its Resistance to Cavitation", Soviet Physics-Doklady, 11, 9, 822-824.

4. Brager, D., Cheesewright, R., Hammitt, F.G., Kemppainen, D.J., "Cavitation Erosion of a Stationary Specimen in Close Proximity to an Oscillating Surface", ORA Technical Report No. 08153-4-T, Department of Nuclear Engineering, University of Michigan, May, 1967.

5. Barnard, B.J., and Cooper, G.A., "Deformation of Solids by Impact of Liquids", Philosophical Transactions of Royal Society A, v. 260, pp. 292-294.

6. Hammitt, F.G., "Cavitation Damage and Performance Research Facilities", ASME Fluids Engr. Conf., Philadelphia, Pa., May, 1964, Symposium on Cavitation Research Facilities and Techniques, 175-184.

7. Robinson, M.J., "On the Detailed Flow Structure and Corresponding Damage to Test Specimens in a Cavitating Venturi," Ph.D. Thesis and ORA Technical Report No. 03424-16-T, Department of Nuclear Engineering, The University of Michigan, August, 1965.

8. Garcia, R., "Comprehensive Cavitation Damage Data for Water and Various Liquid Metals Including Correlations with Material and Fluid Properties,", Ph.D. Thesis and ORA Technical Report No. 05031-6-T, Department of Nuclear Engineering, The University of Michigan, August, 1966.

9. Garcia, R., and Hammitt, F.G., "Cavitation Damage and Correlations with Material and Fluid Properties," ASME Paper Presented ASME Fluids Engr. Div. Conf., May, 1967.

10. Frederick, J.R., Ultrasonic Engineering, John Wiley and Sons, Inc., New York, 1965.

11. Liehhard, J.H., "Synopsis of Lift, Drag, and Vortex Frequency Data for Rigid Circular Cylinders," Washington State University College of Engineering Research Division, 1966.

12. Noell, G. L., "Cavitation Sensitive Coating Evaluation," Pratt Whitney Aircraft-CANAL, Tech. Info. Memo. No. 878.

13. Wood, G.M., Kulp, R.S., and Altieri, J.V., Jr., "Cavitation Damage Investigations in Mixed Flow Liquid Metal Pumps", Pratt-Whitney-CANAL, Symposium on Cavitation in Fluid Machinery Winter Annual Meeting ASME, Chicago, Nov. 1965.

14. Hammitt, F.G., Lafferty, J.F., Cheesewright, R., Pitek, M.T. Kemppainen, D.J., and Mitchell, T.M., "Laboratory Scale Devices for Rain Erosion Simulation," Second Meersburg Conference on Rain Erosion and Associated Phenomena, Meersburg, Federal Republic of Germany, and ORA Report No. 08153-3-T, Department of Nuclear Engineering, The University of Michigan, March, 1967.

15. Den Hartog, J.P., Strength of Materials, 1st Edition, McGraw Hill Book Co., Inc. 1949.

16. Garcia, R., Nystrom, R.E., and Hammitt, F.G., "Ultrasonic-Induced Cavitation Studies in Mercury and Water," ORA Technical Report No. 05031-3-T, Department of Nuclear Engineering, The University of Michigan, December 1965.

17. Nowotny, H., "Destruction of Materials by Cavitation," VDI-Verlag, Berlin, German, 1942, Reprinted by Edwards Brothers, Inc., Ann Arbor, Michigan, 1946, English Translation Available as ORA Technical Report No. 03424-15-I, Department of Nuclear Engineering, The University of Michigan, 1962.

18. Metals Handbook, Vol.I, Taylor Lyman, Editor-in-Chief, Eighth Edition, American Society of Metals, 1961.

19. Garcia, R., and Hammitt, F.G., "Ultrasonically Induced Cavitation Studies", ORA Technical Report 05031-1-T, Department of Nuclear Engineering, The University of Michigan, October,1964.

20. Devine, R.E., and Plesset, M.S., "Temperature Effects in Cavitation Damage", Report No. 85-27, Division of Engineering and Applied Science, California Institute of Technology, Pasadena, California, April, 1964.

21. Robinson, M.J., and Hammitt, F.G., "Detailed Damage Characteristics in a Cavitating Venturi", Trans. ASME, J. Basic Engr., 89, D, pp. 161-173, March, 1967.

22. Hammitt, F.G., and Kemppainen, D.J., "Cavitating Flow Past Transverse Cylinder in Venturi Diffuser with Water and Mercury", ORA Technical Report No. 01357-6-T, Department of Mechanical Engineering, The University of Michigan, March, 1969. (To be presented at the 3rd Conference on Hydraulics and Hydraulic Machinery, Budapest, Hungary, September, 1969.).

23. Kemppainen, D.J., and Hammitt, F.G., "Effects of External Load on Cavitation Damage", ORA Technical Report No. 01357-5-T, Department of Mechanical Engineering, The University of Michigan, March, 1969. (Submitted for IAHR Symposium, Kyoto, Japan, September, 1969.).

24. Kemppainen, D.J., and Hammitt, F.G., "Applied Stress and Cavitation Damage," ASME paper presented at ASME Fluids Engineering Conference, June, 1967.

APPENDIX I

Calibration of Hydraulic Cylinder and Pressure Transducer

To make possible the loading of the specimen to the desired stress level it was necessary to first obtain information relating the readout of the strain indicator to the load applied to the hydraulic ram. To accomplish this a cradle arrangement was manufactured to hold the hydraulic cylinder while under tensile load. Fig. 91 shows an exploded view of the tensile cradle. This particular arrangement was designed such that the primary load was held by the five threaded rods rather than the four holding rods of the cylinder itself. This relieved the cylinder of undue stress in these calibration tests.

Prior to test, the hydraulic cylinder was cradled in the fixture and fastened securely to prevent misalignment when tensile forces were applied. This composite assembly is shown in Fig. 92

The entire assembly was then placed between the upper and lower platens of a Baldwin tensile test machine in the same manner as an ordinary tensile test specimen (Fig. 93). The hydraulic system to be used in the ultrasonic test assembly was connected to the hydraulic cylinder. Using the cylinder's own pump system, the pressure at the pressure transducer pickup was plotted against the force produced on the Baldwin gauge.

A Budd Strain Indicator model P-350 was used as a digital readout. The adjustable balance and gage factor controls were set so that the entire operating range could be covered by the strain indicator. The optimum setting for this test was found to be at a gage factor of 0.37 and a balance of 5.34. By resetting the controls at these figures the load versus readout would remain the same for each test.

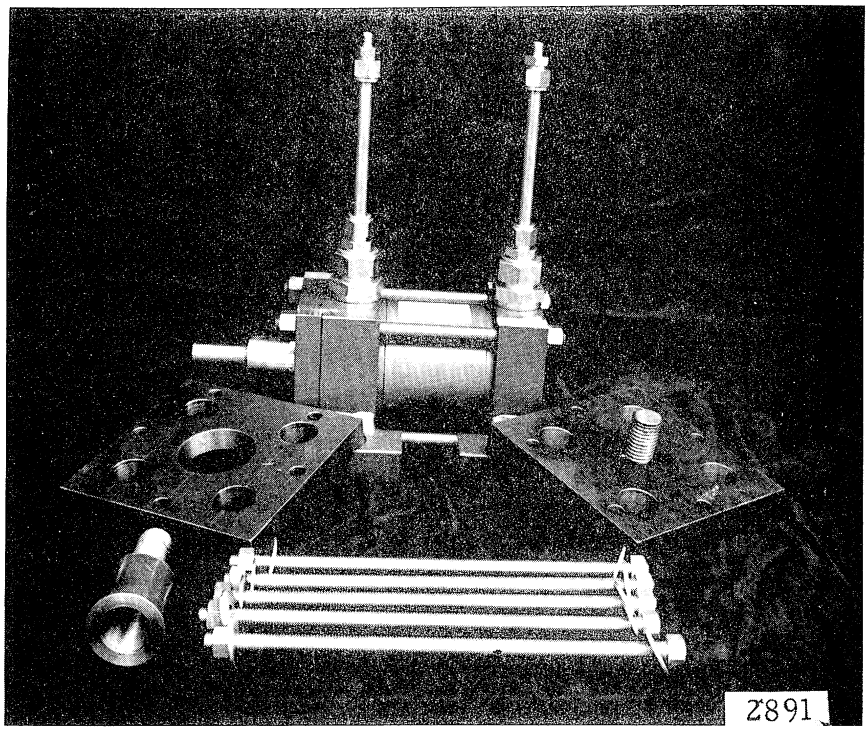

Fig. 91. Tensile Cradle Prior to Assembly

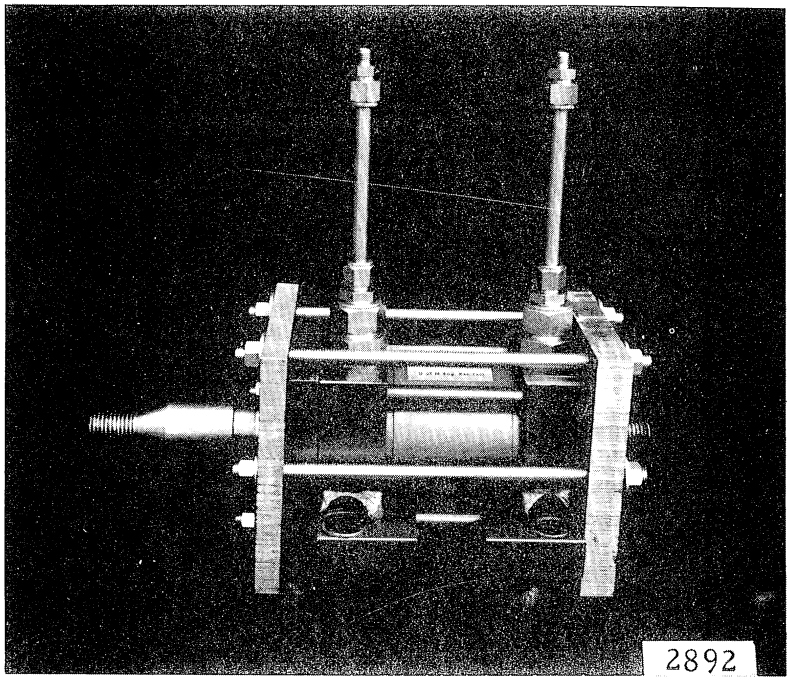

Fig. 92. Assembly for Tensile Calibration of Hydraulic Cylinder

The hydraulic cylinder was next calibrated in the compressive mode. The cradle was removed and the cylinder set flat on the lower carriage of the tensile machine (Fig. 94). The upper ram adapter was screwed into a holder which fit snugly against the pressure head of the machine. The pressure pump of the hydraulic system was again used to provide internal pressure to the hydraulic cylinder. The upper pressure head read force applied by the cylinder ram on the Baldwin gage. The entire set up is shown in Fig. 95.

The digital readout of the Budd strain indicator was again used; however, the gage factor settings and balance were left as originally set. This provided for switch-over from tension to compression during any test period without resetting.

Two calibration curves were generated by least squares fit: one for compression and one for tension. The two curves (Fig. 96) were then used as a basis for calculation of applied stress on the specimens.

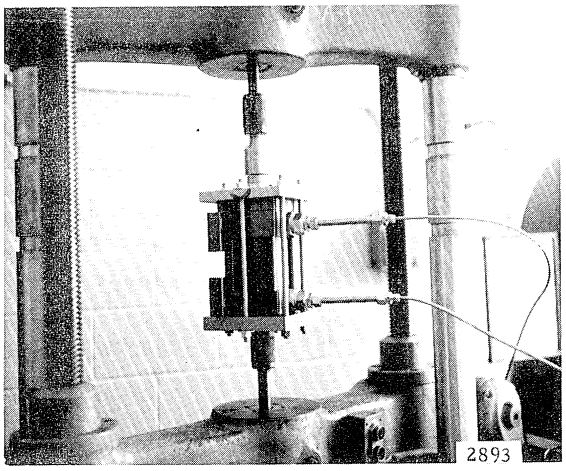

Fig. 93. Setup for Tensile Calibrati on of Hydraulic Cylinder

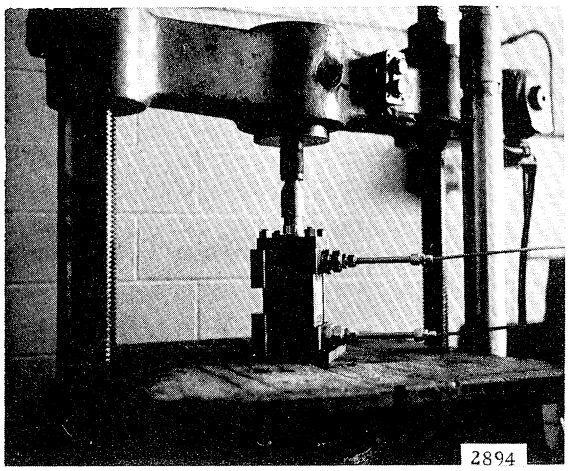

Fig. 94. Setup for Compressive Calibration of Hydraulic Cylinder

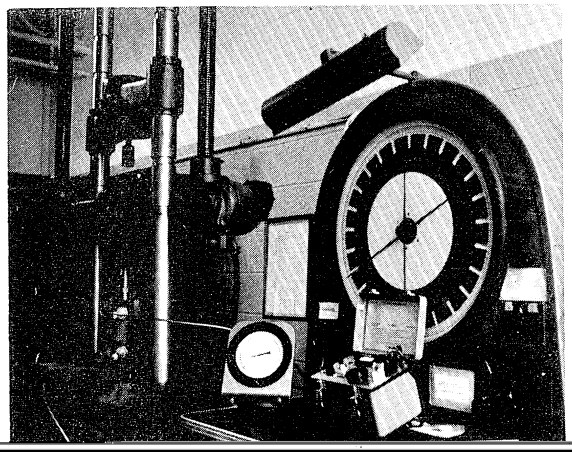

Fig. 95. Photograph of Total Calibration Setup

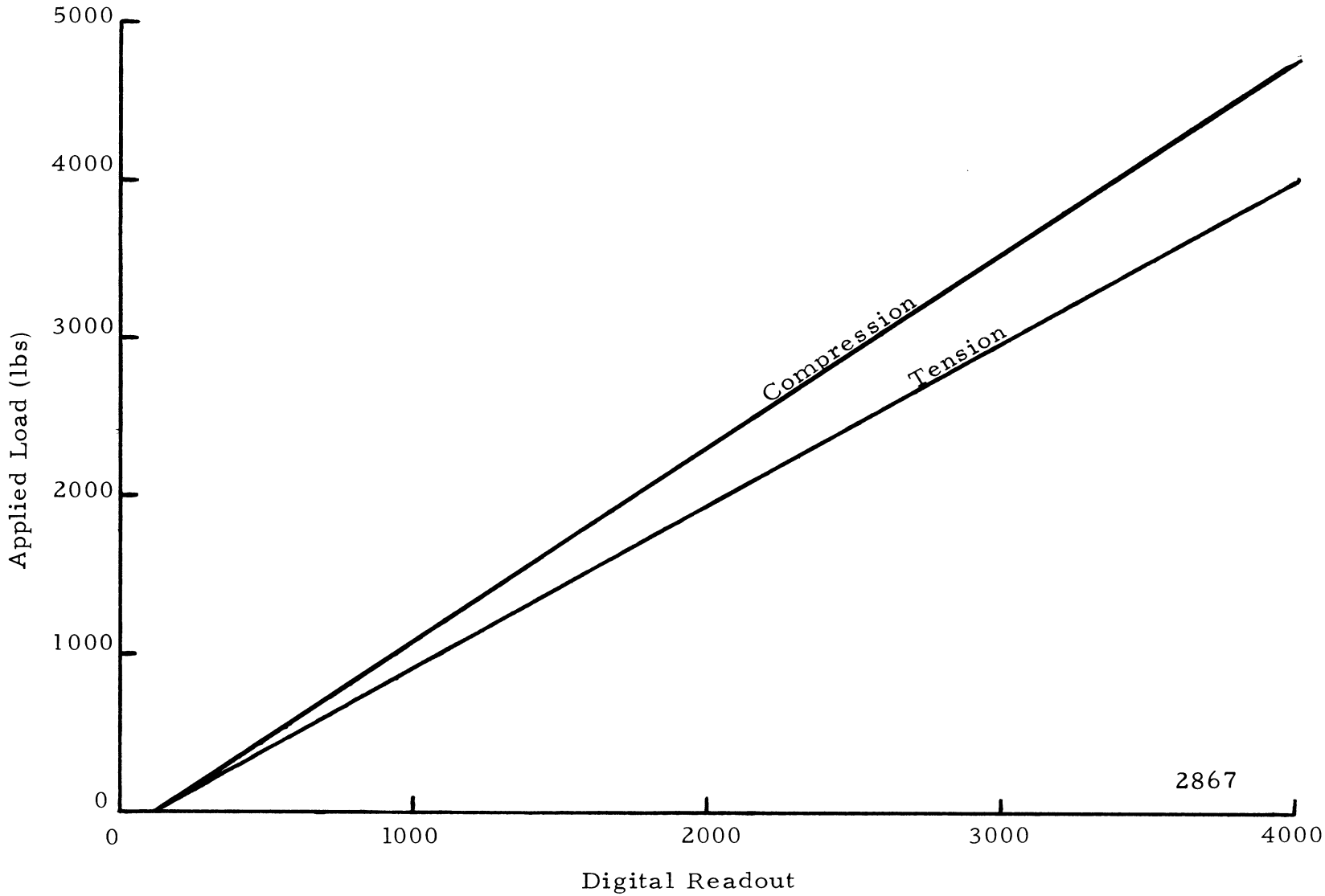

Fig. 96. Hydraulic Cylinder Calibration Curves

APPENDIX II

Measurement of Test Amplitude

The ultrasonic horn was calibrated using an MTI Fotonic Sensor*. The sensor has a linear range of 2-8 mils and an accuracy of 40 μ inches.

A probe support suitable for use with the stabilizer plate on the ultrasonic horn was built. This unit consists of a 1/2 inch SS holder with an attached pointer. The plate sets on three posts accurately machined to position the sensor squarely against the face of the test button.

The sensor is inserted through a 1/8 inch diameter hole in a calibrated head assembly. The head assembly is threaded with 1 1/4 inch x 40 micrometer thread and calibrated in 1 mil steps up to 10 mils. The sensor tube is held in place by a teflon spacer placed at the end of a #8 socket head cap screw set at 90^{o} to the sensor tube.

In order to calibrate the movement of the test button the Fotonic Sensor is first to be calibrated. The surface of the test button was highly polished to increase its reflectivity. The sensor tube was placed in the micrometer head and moved downward slowly until it contacted the surface of the button.

If a zero reading were not obtained the specimen surface was not perpendicular to the sensor tube. Suitable changes had to be made in the specimen so that a zero reading would be possible when the sensor probe and the specimen were in contact. When a zero reading was obtained, the micrometer head was also set to a zero reading with the indicator. The sensor probe was then withdrawn until a 0.200 inch shim could be placed between the probe and horn tips. The probe was pressed against the feeler gage with a slight pressure and the cap screw

*Fotonic Sensor Model KD-38, Instruments Div., Mechanical Technology, Inc.

was tightened against the probe. The micrometer head was then backed off to 0.005 in. and the 0.020 in. feeler gage is removed. The micrometer was again brought to the zero indicator reading and the meter of the Fotonic Sensor adjusted to read 100 per cent of scale. The capscrew was then released and the probe again placed against the surface of the horn tip. The micrometer head was set to zero and the cap screw tightened enough to hold the probe securely. The output of the Fotonic Sensor was then connected to an oscilloscope. The scope was set at 0.1 volt per cm. and a time base of 2 microsec per cm.. The beam was set to a vertical zero with the probe against the horn tip. Pictures of the trace position were taken consecutively at 0.001, 0.002, 0.003, 0.004, 0.005, and 0.006 inches. The sensor probe was then loosened and moved upward for calibration. The 0.020 inch shim was again placed between the probe tip and the button, and the 100% calibration point again checked. If this check was found not to be the same the process was repeated. Five sets of data were subsequently recorded for every calibration run made for the Fotonic Sensor.

The calibration of the horn amplitude was done in much the same manner. The sensor probe was again set at 0.020 for 100% meter reading. The probe was placed against the surface of the test button and then withdrawn to a distance corresponding to approximately 0.35 volts output. The ultrasonic horn was activated and the resulting wave photographed on the oscilloscope. Due to the time base setting of the scope, the photograph resembled a wide band of superimposed wave forms. The ultrasonic assembly was run at 3-4 different settings and pictures taken of the resulting waveform band. After each set of pictures the sensor was again checked for calibration at 100%. The resulting wave band was then measured

and an average band width for each power setting calculated. These results were then plotted as amplitude vs. percent power input to the horn assembly. The operating conditions were chosen from this set of points. Operation was always at an amplitude of two mils.

UNIVERSITY OF MICHIGAN
3 9015 03023 0067